

**Crystal Structure and Oxide Ion Diffusion  
in Pyrochlore Related Oxides**

**Ushio Matsumoto**

**Crystal Structure and Oxide Ion Diffusion  
in Pyrochlore Related Oxides**

**Ushio Matsumoto**

**2022**



## Acknowledgements

I would like to express my gratitude to my supervisor, Professor Isao Tanaka at Kyoto University, who patiently taught me invaluable lessons about integrity, honesty, and objectivity throughout my doctoral course. Thanks to his unstinting efforts, my research and other aspects of my life have improved greatly over the three years. I would also like to express my gratitude to Professor Kuniaki Murase and Professor Tetsuya Uda for their critical reading of this manuscript.

I also wish to thank Associate Professor Atsuto Seko at Kyoto University for many helpful discussions and comments when I was preparing to publish my first paper. I am also grateful to Assistant Professor Hiroyuki Hayashi at Kyoto University for many inspiring discussions and comments during our group meetings.

I am grateful to Dr. Hiroki Moriwake at Japan Fine Ceramics Center for his kind advice and generous support. I was able to complete my thesis on time in large part because of the supportive research environment at Japan Fine Ceramics Center. I am also grateful to Drs. Akihide Kuwabara and Satoshi Kitaoka, who provided many opportunities to undertake stimulating research projects. Their guidance and suggestions made it possible to obtain many of the research results contained in this thesis. Collaborating with both experimentalists and theoreticians has been a valuable experience for me.

I wish to thank Dr. Takafumi Ogawa for patiently teaching me how to perform first-principles calculations, and for giving me valuable guidance when studying pyrochlores. I also wish to thank Dr. Craig A. J. Fisher for many valuable discussions on molecular dynamics simulations, and for being a good English teacher.

I must also thank all of the collaborators who have worked with me during three years. I would like to thank, in no particular order, the following people: Dr Makoto Tanaka, Mr. Naoki Kawashima, and Mr. Kenta Asai during the experimental and theoretical work on  $\text{Y}_2\text{Ti}_2\text{O}_7$  pyrochlore-related oxides; Mrs. Rie Yokoi for help with many of the NMR calculations, NMR analysis, and free energy calculations for a variety oxides; Mr. Masashi Taki at Nagoya Institute of Technology for his patient implementation of the NMR experiments; Assistant Professor Hidenobu Murata at Osaka Prefecture University for many in-depth discussions on the pyrochlore-related oxides; Assistant Professor Shusuke Kasamatsu at Yamagata University for help with the machine learning potentials; Mr. Keiyu Mizokami and Mr. Takayuki Nishiyama for their kindness; Ms Makiko Orita for her kindness and support throughout my doctoral course.

To my lunch buddies, I would like to thank: Dr. Satoshi Suehiro, Dr. Hsin-Hui Huang, and Mrs. Ayako Taguchi for exploring new restaurants and cafes with me; Mr. Tomohiro Kuroyama, Dr. Sota Terasaka, and Mr. Sou Oyama for teaching me about the Nagoya cuisine.

I would also thank to my supervisors at Furukawa Electric Co., Ltd., Former Director Takahiro Ueno, Director Takehiko Nomura, and Dr. Koji Fujimura, who provided me with valuable opportunities to work outside the company, encouraging me to pursue my own research, and occasionally treating me to delicious meals at *izakaya*.

Finally, to my mother (Yoriko Matsumoto) and father (Kyoichi Matsumoto), and my sister (Tsukiko Matsumoto), I wish to thank you for your unwavering emotional and financial support during all my years at Kyoto University. After many twists and turns, here I am.

Nagoya 2022

Ushio Matsumoto

# Contents

<b>Chapter 1</b> .....	1
<b>1.1 Background</b> .....	1
<b>1.2 Pyrochlore-Related Structures</b> .....	4
<b>1.3 Research Objectives</b> .....	6
<b>1.4 Thesis Overview</b> .....	6
<b>Bibliography</b> .....	10
<b>Chapter 2 Chemical Environment of Al in Al-doped Y<sub>2</sub>Ti<sub>2</sub>O<sub>7</sub>: <sup>27</sup>Al NMR Spectroscopy and DFT-GIPAW Calculations</b> .....	15
<b>2.1 Introduction</b> .....	15
<b>2.2 Experimental and Calculation methods</b> .....	17
<b>2.2.1 Materials Synthesis</b> .....	17
<b>2.2.2 Solid-State NMR Spectroscopy</b> .....	17
<b>2.2.3 First-principles Calculations</b> .....	18
<b>2.3 Results</b> .....	21
<b>2.3.1 <sup>27</sup>Al NMR Spectroscopy</b> .....	22
<b>2.3.2 First-principles Calculations of NMR Parameters</b> .....	26
<b>2.3.3 Defect Stability</b> .....	29
<b>2.4 Discussion</b> .....	33
<b>2.5 Conclusions</b> .....	35
<b>Appendix 2.A Convergence Test</b> .....	36
<b>Appendix 2.B Defect Cluster Model</b> .....	37
<b>Bibliography</b> .....	38
<b>Chapter 3 Cooperative Oxide-Ion Transport in Pyrochlore Y<sub>2</sub>Ti<sub>2</sub>O<sub>7</sub>: A First-principles Molecular Dynamics Study</b> .....	43
<b>3.1 Introduction</b> .....	43
<b>3.2 Computational Methods</b> .....	46
<b>3.3 Results and Discussion</b> .....	48
<b>3.4 Conclusions</b> .....	57

3.5 Acknowledgement.....	58
Appendix 3.A Band Gap of the Structure $\text{Y}_2\text{Ti}_2\text{O}_7$ .....	59
Appendix 3.B Defect State Diagrams.....	60
Appendix 3.C Pseudo-code of the Mapping Approach .....	61
Bibliography .....	63
<b>Chapter 4 First-Principles Study on the Stability of Weberite-type, Pyrochlore, and Defect-Fluorite Structures of <math>A_2B_2O_7</math> (<math>A = \text{Lu}^{3+}</math>–<math>\text{La}^{3+}</math>, <math>B = \text{Zr}^{4+}</math>, <math>\text{Hf}^{4+}</math>, <math>\text{Sn}^{4+}</math> and <math>\text{Ti}^{4+}</math>) .....</b>	<b>68</b>
4.1 Introduction .....	68
4.2 Calculation Methods .....	71
4.3 Results and Discussion .....	72
4.4 Conclusions .....	83
4.5 Acknowledgement.....	84
Appendix 4.A Lattice Parameters of $\text{Yb}_2\text{Ti}_2\text{O}_7$ .....	85
Appendix 4.B Positional Parameters of $\text{Yb}_2\text{Ti}_2\text{O}_7$ .....	86
Appendix 4.C Atomic Configurations of Pyrochlore and Weberite-type Structures .....	87
Appendix 4.D Configurations of Cations in $\text{Yb}_3\text{TaO}_7$ and $\text{Yb}_2\text{Ti}_2\text{O}_7$ Weberite-type Structures .....	88
Bibliography .....	89
<b>Chapter 5 Oxide-Ion Diffusion in Weberite-type and Pyrochlore Structures <math>\text{Yb}_2\text{Ti}_2\text{O}_7</math>: A First-principles Molecular Dynamics Simulations .....</b>	<b>94</b>
5.1 Introduction .....	94
5.2 Computational Methods .....	95
5.3 Results and Discussion .....	97
5.4 Conclusions .....	101
Bibliography .....	103
<b>Chapter 6 General Conclusion.....</b>	<b>105</b>

# Chapter 1

## General Introduction

### 1.1 Background

To mitigate global warming and climate change, the Paris Agreement, an international treaty on climate change, was formulated in 2015.<sup>1</sup> The main goal of the Paris Agreement is to limit global warming to below 2 degrees Celsius above pre-industrial levels.<sup>1,2</sup> To achieve this, signatories to the agreement are obligated to reach a state of net-zero carbon dioxide emissions, or carbon neutrality, by the year 2050.<sup>2,3</sup> Anthropogenic greenhouse gasses are predominantly produced during combustion of fossil fuels to generate electricity and heat, and thus there is an urgent need to transition toward a society based on alternative renewable energy resources such as solar, wind, geothermal, ocean, biogas, and hydroelectric.<sup>3-6</sup> At the same time, hydrogen and ammonia have been attracting attention as clean and carriageable non-carbon fuels to replace fossil fuels.<sup>5,7-12</sup>

Fuel cells (FCs) are a class of electrochemical energy conversion devices, and include, proton-exchange membrane fuel cells, phosphoric acid fuel cells, solid acid fuel cell, alkaline fuel cell, direct methanol fuel cells, redox fuel cell, and solid oxide fuel cells (SOFCs).<sup>4,5,7,13-19</sup> SOFCs consist of a cathode, an anode, and an electrolyte, all of which are generally made of solid oxides. SOFCs are one of the most promising FCs, because they offer several advantages such as high efficiency, long-term stability, and relatively low cost.<sup>7,13,18-21</sup> On the other hand, the high operating temperature of SOFCs is one disadvantage.<sup>7,17-19,22</sup> During thermal cycling difference in mechanical properties and thermal expansion behavior between the constituent materials and layers of the cell results in thermal stresses. The cyclic thermal stresses can cause peeling and cracking of SOFC components, leading to the mechanical failure of the device.

Mixed ion-electron conductors are solid oxides that exhibit both high oxide-ion and electron conductivities. The perovskite-type solid solutions such as Ba-doped  $\text{LaNiO}_3$  and Sr-doped  $\text{LaMnO}_3$  has been commercially used as cathode materials which exhibits high electron conductivity and oxygen reduction activity.<sup>7,17</sup> However, the difference in thermal expansion between electrolyte materials and those cathode materials causes thermal stresses.

Oxide-ion conductors are solid oxides that exhibit high oxide-ion conductivity; in general, this occurs by oxide ions hopping between vacancies. Yttrium stabilized zirconia (YSZ), which has a pyrochlore-related crystal structure, has been commercially used as an electrolyte in SOFCs over the past few decades.<sup>7,17</sup> Use of YSZ, however, requires a high operating temperature to obtain a sufficiently high oxide-ion conductivity.<sup>7</sup> Thus, alternative SOFC electrolyte and cathode materials which exhibits high ionic conductivity at low temperatures are needed, providing a motivation to develop new oxide-ion conductors.<sup>22</sup>

The pyrochlore-related oxides  $A_2B_2O_7$  ( $A$  = rare-earth element,  $B$  = transition metal) are a promising family of oxides in the search for new solid electrolyte and electrode materials owing to their wide chemical space represented by elements  $A$  and  $B$  means that tuned by controlling their composition, incorporation on dopant elements (Figure 1.1). Consequently, a huge amount of research has been carried out as reported in the literature.<sup>23,24,33,34,25-32</sup> Furthermore, since the ordered pyrochlore (P) structure can transform into the disordered defect-fluorite (DF) structure by thermal, compositional, and pressure control with changes in physical and chemical properties, considerable efforts have been expended to elucidate the key factor to govern structural stability.<sup>26-29,31,35-41</sup>

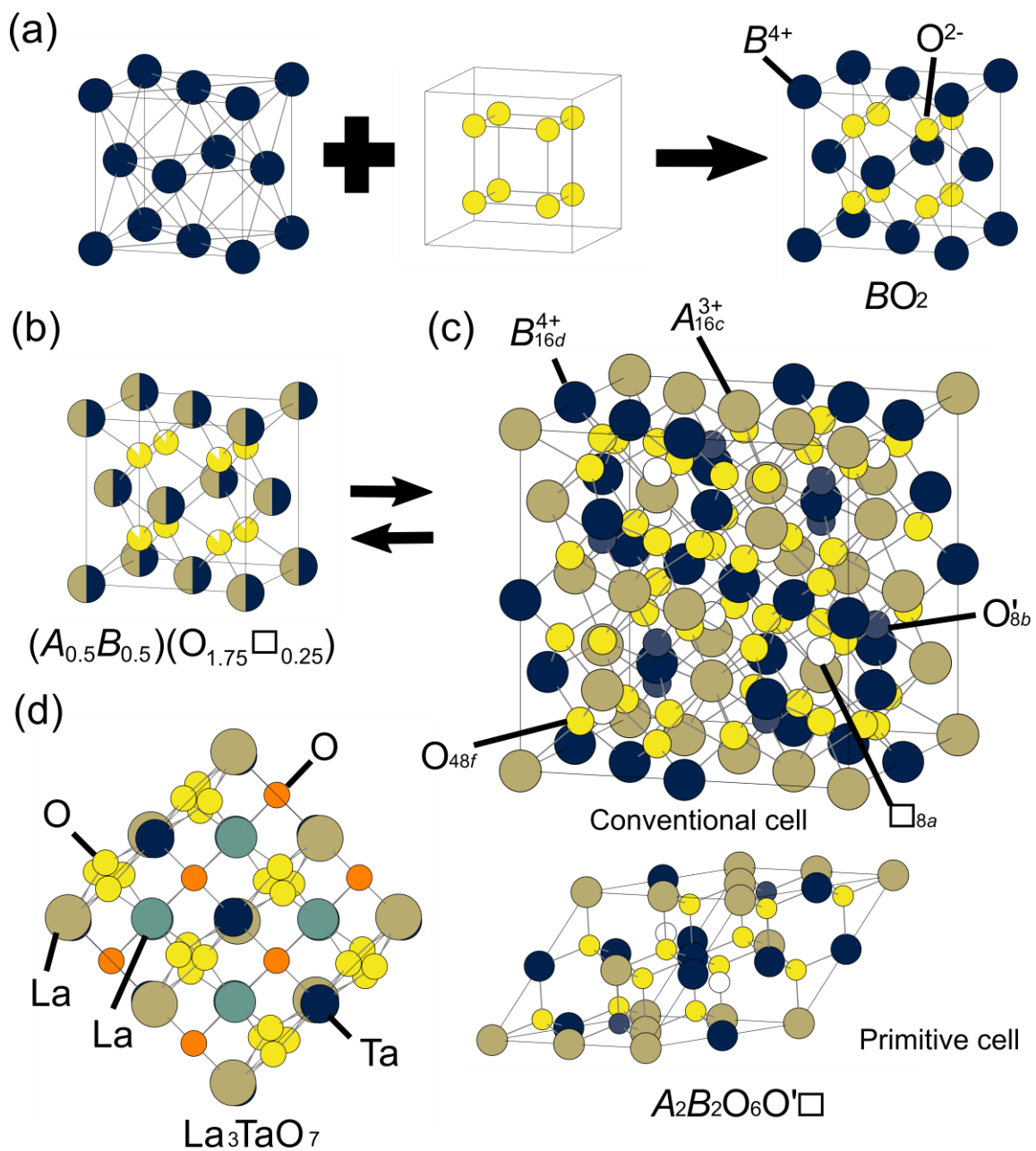


**Figure 1.1.** Crystal structures: (a) fluorite, (b) defect-fluorite, (c) pyrochlore, and (d)  $\text{La}_3\text{TaO}_7$  weberite.

## 1.2 Pyrochlore-Related Structures

The crystal structures of the pyrochlore-related oxides have been studied many times by X-ray diffraction (XRD), X-ray absorption near edge, extended X-ray absorption fine structure, Neutron diffraction, Infrared, Raman, and nuclear magnetic resonance (NMR) spectroscopy.<sup>26–29,31,35–41</sup> In 1983, Subramanian et al. suggested that the stability of the P structure strongly depends on the ionic radius ratio with compounds with large ionic radius ratios ( $r_A/r_B > 1.46$ ) preferentially forming the P structure and compounds with small ionic radius ratios ( $r_A/r_B < 1.46$ ) forming the DF structure.<sup>42</sup> For the stability field of the P structures, two phase transformations are experimentally observed based on XRD analyses.<sup>26–28,31,36,43</sup> At high temperature, the P structures are transformed into the DF structures by heating. This transformation is explained by the stabilization of increase of configurational entropy at high temperature region, which is supported in part by the theoretical predictions based on free energy calculations.<sup>44</sup> In contrast, at low temperature the phase transformation from the DF to the P structures can be induced by the balance between the redistribution energy of cations and free energy of the system, but the corroborative evidence has not been reported yet.

The DF structure with cubic space group  $Fm\bar{3}m$  is an oxygen-deficient fluorite structure, which is composed of face-centered-cubic (fcc) array cations and simple-cubic (sc) array anions (Figure 1.1a,b). In DF oxides, two types of cations and anions are randomly distributed on cation and anion sublattices, respectively, which means that DF oxides is a disordered phase. The compositional formula of  $A_2B_2O_7$  DF oxides is also expressed as  $(A_{0.5}B_{0.5})(O_{1.75}\square_{0.25})$ , where the intrinsic vacancy is labeled  $\square$ . There are one cation and one anion site; both  $A$  and  $B$  at  $4a$  (0,0,0), and O at  $8c$  (1/4,1/4,1/4) site in Wyckoff notation.

The P structure with the general formula  $A_2B_2O_7$  with cubic space group  $Fd\bar{3}m$ , which is also expressed as  $A_2B_2O_6O'\square$ , is an ordered structure of the DF structure (Figure 1.1c). In the ideal

pyrochlore, there are two cation and three anion sites; *A* at 16*c*, *B* at 16*d*, O at 48*f*, O' at 8*b* crystallographically nonequivalent sites, respectively. 8*a* (1/8, 1/8, 5/8) site is unoccupied. 16*c* and 16*d* sites have different chemical environments, viz., 16*c* and 16*d* sites are surrounded by six 48*f* and two 8*b*, six 48*f* and two 8*a* sites, respectively.

It is worth noting that both DF and P oxides contain the intrinsic vacancies, since the migration of oxide ions is mediated by their vacancies. Oxide-ion migration pathways has been highlighted by van dijk et al.,<sup>24</sup> who proposed that, in the P structure, the oxide ion jump from the 48*f* site to the 8*a* site is energetically preferred pathway and a continuous favorable pathway is formed with 48*f*–48*f* sites. Subsequent simulation studies, based on force field simulations, showed that the migration energy and formation energy of anion Frenkel strongly depend on the *A* and *B* cations.<sup>23,25</sup> First-principles calculations also confirmed the similar trend, supporting the formation of a continuous favorable path at the 48*f*–48*f* sites.<sup>45</sup> On the other hand, maximum entropy Patterson analyses with XRD and neutron diffraction spectroscopy studies have supported that a continuous oxide-ion density between 48*f*–8*a* and 48*f*–48*f* sites.<sup>46,47</sup> Therefore, there is a discrepancy between experimental and calculated results.

The weberite structure is one of ordered structures of pyrochlore-related structures, which have been observed in  $\text{Ca}_2^{2+}\text{Sb}_2^{5+}\text{O}_7$  and  $\text{La}_3^{3+}\text{Ta}^{5+}\text{O}_7$  oxides.<sup>48,49</sup> Experimental studies based on neutron pair distribution function (PDF) analysis by Shamblin et al. have revealed that the weberite-type structures are locally formed in the  $\text{Ho}_2\text{Zr}_2\text{O}_7$  oxide,<sup>50</sup> which is identified as a long-range disordered phase by XRD analysis.<sup>50</sup> Similarly, O'Quinn et al. reported that crystalline phase fraction of  $\text{Er}_2\text{Ti}_{2-x}\text{Zr}_x\text{O}_7$  synthesized by mechanical milling technique changes from weberite to pyrochlore structures with increasing temperature.<sup>51,52</sup> These experimental observations indicates that a weberite-type structure can be a stable structure in  $A_2B_2\text{O}_7$  oxides.

Despite experimental and theoretical researches on pyrochlore-related oxides, theoretical understanding of defects and oxide-ion diffusion has been a subject of research, because analyses of them have been not established yet. Also, the possibility of the existence of another thermodynamical stable phase such the weberite-type structure has not been systematically investigated. Therefore, further studies of pyrochlore-related oxides at the atomic level are needed.

### 1.3 Research Objectives

The first objective of this thesis was to elucidate the defect states of dopants and oxide-ion diffusion in the P structure. Although many studies have been reported so far, the chemical environments around dopants Al remains unknown. To examine the defects in the Al-doped P oxide,  $^{27}\text{Al}$  MAS-NMR experiments were carried out. Moreover, oxide-ion diffusion in pyrochlore oxides were examined using first-principles molecular dynamics (FPMD) simulations. To quantify the oxide-ion diffusion, the mapping approach for times-series analyzing was developed.

The second objective of this thesis was to discover new oxide-ion and/or mixed ion-electron conductors in pyrochlore-related oxides through theoretical calculations. To search unknown structures with  $A_2B_2O_7$  composition, configurational searching based on two-sublattice models were systematically carried out by first-principles calculations. Moreover, the oxide-ion diffusion in pyrochlore-related structures was examined using FPMD simulations.

### 1.4 Thesis Overview

This thesis is organized into six chapters as follows. Chapter 1 introduces the background. In Chapter 2, the chemical environments in an Al-doped  $\text{Y}_2\text{Ti}_2\text{O}_7$  P oxide (hereinafter referred to as  $\text{Y}_2\text{Ti}_2\text{O}_7:\text{Al}$ ), corundum  $\alpha\text{-Al}_2\text{O}_3$ , and garnet  $\text{Y}_3\text{Al}_5\text{O}_{12}$  are investigated using  $^{27}\text{Al}$  magic angle spinning (MAS)

NMR experiments and first-principles calculations. 1D MAS-NMR spectra of  $\text{Y}_2\text{Ti}_2\text{O}_7:\text{Al}$  are recorded at the different magnetic field strengths of 9.4 T and 14.1 T. Two signals of  $^{27}\text{Al}$  at round 17 and 22 ppm are seen in the spectra of  $\text{Y}_2\text{Ti}_2\text{O}_7:\text{Al}$  recorded at 14.1 T. The major signal with double peaks shows a characteristic of second-order electric quadrupole interaction. The NMR parameters of the major signal are in good agreement with those of  $\text{Al}'_{\text{Ti}}$  using NMR parameters from first-principles calculations, corroborating that dopant Al predominantly substitutes into Ti site. On the other hand, the weak signal is found to correspond with  $\alpha\text{-Al}_2\text{O}_3$ , which indicates that  $\text{Y}_2\text{Ti}_2\text{O}_7:\text{Al}$  synthesized using an ultraspray pyrolysis technique contains a small amount of unreacted  $\alpha\text{-Al}_2\text{O}_3$ . These findings demonstrate the utility of the combination scheme with NMR experiments and first-principles calculations to determine the chemical environments of defects in oxides. Furthermore, the thermodynamic stability of defects in pyrochlore  $\text{Y}_2\text{Ti}_2\text{O}_7:\text{Al}$  are examined using first-principles calculations to evaluate preference to the association with  $\text{Al}'_{\text{Ti}}$  and oxygen vacancy. The resulting free energy show that defect  $\text{Al}'_{\text{Ti}}$  is preferred to associate with oxygen vacancy at lower temperatures of 500 K, whereas at higher temperatures defect  $\text{Al}'_{\text{Ti}}$  and oxygen vacancy are favored to isolate.

In Chapter 3, oxide-ion diffusion in pyrochlore  $\text{Y}_2\text{Ti}_2\text{O}_7$  (space group:  $Fd\bar{3}m$ ) is investigated using first-principles molecular dynamics simulation. To quantify the defect states and oxide-ion migration mechanism observed during first-principles molecular dynamics simulations, a mapping approach for analyzing time-series data of local structural units based on Voronoi–Dirichlet partition is developed. Defect states are classified into three types: a Frenkel pair, a single vacancy, and a split vacancy. Although the energetically most favorable defect type is a split vacancy at low temperatures, split and single vacancies are found to be equally favorable at high temperatures. Oxide-ion migration occurs by a two-step cooperative mechanism via a split vacancy. Climbing-image nudged elastic band calculations show the energy barrier for the cooperative diffusion mechanism (0.65 eV) to be

substantially less than that of a simple stepwise mechanism (0.96 eV). This lower energy barrier is comparable to experimental activation energies of oxide-ion diffusion in  $\text{Y}_2\text{Ti}_2\text{O}_7$  reported in the literature, making this previously unrecognized cooperative mechanism the most likely candidate for enabling oxide-ion transport in the titanate pyrochlore.

In Chapter 4, crystal structures and energetics of a series of  $A_2B_2O_7$  ( $A = \text{Lu}^{3+}\text{--La}^{3+}$ ,  $B = \text{Zr}^{4+}$ ,  $\text{Hf}^{4+}$ ,  $\text{Sn}^{4+}$ , and  $\text{Ti}^{4+}$ ) compounds were systematically investigated using first-principles calculations. Experimentally they are known to form either pyrochlore or defect-fluorite structures. Recently formation of a weberite-type ordering was reported in  $\text{Ho}_2\text{Zr}_2\text{O}_7$ .<sup>50</sup>  $\text{Yb}_2\text{Ti}_2\text{O}_7$  is known to form a pyrochlore structure by ordinary solid phase reaction synthesis at high temperature, but it has been reported that the 100 reflection peak in the XRD pattern becomes weaker by heat treatment at low temperature,<sup>28</sup> suggesting the formation of another ordered state or a change to it. An exhaustive configurational search based on sub-lattice models shows that the lowest energy structure is a triclinic weberite-type structure characterized by alternating Yb and Ti layers. Free energies from first-principles phonon calculations suggest that the transition temperature between the weberite-type and pyrochlore structures of  $\text{Yb}_2\text{Ti}_2\text{O}_7$  is 550 K. The energies of the weberite-type and pyrochlore structures are also compared for a wide range of  $A_2B_2O_7$  compositions. It is found that the stability of the weberite-type structure increases relative to the pyrochlore structure as the  $A^{3+}$  cation radius decreases. Energies of disordered defect-fluorite structures estimated using special quasi-random structures are also reported. The formation of such defect-fluorite structures is found to be more energetically favorable at high temperatures in  $A_2\text{Zr}_2\text{O}_7$  and  $A_2\text{Hf}_2\text{O}_7$  when the  $A^{3+}$  cation radius is small. These results are consistent with previously reported experimental results.

In Chapter 5, oxide-ion diffusion in both weberite-type and pyrochlore structures with the composition  $\text{Yb}_2\text{Ti}_2\text{O}_7$  are investigated using FPMD simulations. Three-dimensional oxide-ion diffusion between  $48f$  and  $48f$  sites are found in the pyrochlore structure, whereas two-dimensional

diffusion on the Ti–O layers are found in the weberite-type structure. Furthermore, oxide-ion diffusion coefficient of the weberite-type is found to be large than that of pyrochlore by one order of magnitude. Finally, chapter 6 summarizes the conclusions for each chapter.

## Bibliography

- [1] UNFCCC. *Paris Agreement, Decision 1/CP.21*; **2015**.
- [2] Roelfsema, M.; van Soest, H. L.; Harmsen, M.; van Vuuren, D. P.; Bertram, C.; den Elzen, M.; Höhne, N.; Iacobuta, G.; Krey, V.; Kriegler, E.; Luderer, G.; Riahi, K.; Ueckerdt, F.; Després, J.; Drouet, L.; Emmerling, J.; Frank, S.; Fricko, O.; Gidden, M.; Humpenöder, F.; Huppmann, D.; Fujimori, S.; Fragkiadakis, K.; Gi, K.; Keramidas, K.; Köberle, A. C.; Aleluia Reis, L.; Rochedo, P.; Schaeffer, R.; Oshiro, K.; Vrontisi, Z.; Chen, W.; Iyer, G. C.; Edmonds, J.; Kannavou, M.; Jiang, K.; Mathur, R.; Safonov, G.; Vishwanathan, S. S. Taking Stock of National Climate Policies to Evaluate Implementation of the Paris Agreement. *Nat. Commun.* **2020**, *11* (1), 1–12.
- [3] Woolf, D.; Amonette, J. E.; Street-Perrott, F. A.; Lehmann, J.; Joseph, S. Sustainable Biochar to Mitigate Global Climate Change. *Nat. Commun.* **2010**, *11*, 2096.
- [4] Shiratori, Y.; Ijichi, T.; Oshima, T.; Sasaki, K. Internal Reforming SOFC Running on Biogas. *Int. J. Hydrogen Energy* **2010**, *35* (15), 7905–7912.
- [5] Panwar, N. L.; Kaushik, S. C.; Kothari, S. Role of Renewable Energy Sources in Environmental Protection: A Review. *Renew. Sustain. Energy Rev.* **2011**, *15* (3), 1513–1524.
- [6] Lund, H. Renewable Energy Strategies for Sustainable Development. *Energy* **2007**, *32* (6), 912–919.
- [7] Liu, L.; Kim, G. Y.; Chandra, A. Modeling of Thermal Stresses and Lifetime Prediction of Planar Solid Oxide Fuel Cell under Thermal Cycling Conditions. *J. Power Sources* **2010**, *195* (8), 2310–2318.
- [8] Brennan, L.; Owende, P. Biofuels from Microalgae-A Review of Technologies for Production, Processing, and Extractions of Biofuels and Co-Products. *Renew. Sustain. Energy Rev.* **2010**, *14* (2), 557–577.
- [9] Lu, Y.; Cai, Y.; Souamy, L.; Song, X.; Zhang, L.; Wang, J. Solid Oxide Fuel Cell Technology for Sustainable Development in China: An over-View. *Int. J. Hydrogen Energy* **2018**, *43* (28), 12870–12891.

- [10] Gil, A.; Medrano, M.; Martorell, I.; Lázaro, A.; Dolado, P.; Zalba, B.; Cabeza, L. F. State of the Art on High Temperature Thermal Energy Storage for Power Generation. Part 1-Concepts, Materials and Modellization. *Renew. Sustain. Energy Rev.* **2010**, *14* (1), 31–55.
- [11] Samaroo, N.; Koylass, N.; Guo, M.; Ward, K. Achieving Absolute Sustainability across Integrated Industrial Networks-a Case Study on the Ammonia Process. *Green Chem.* **2020**, *22* (19), 6547–6559.
- [12] Lovegrove, K.; Luzzi, A.; Soldiani, I.; Kreetz, H. Developing Ammonia Based Thermochemical Energy Storage for Dish Power Plants. *Sol. Energy* **2004**, *76* (1–3), 331–337.
- [13] Stambouli, A. B.; Traversa, E. Solid Oxide Fuel Cells (SOFCs): A Review of an Environmentally Clean and Efficient Source of Energy. *Renew. Sustain. Energy Rev.* **2002**, *6* (5), 433–455.
- [14] Stambouli, A. B.; Traversa, E. Fuel Cells, an Alternative to Standard Sources of Energy. *Renew. Sustain. Energy Rev.* **2002**, *6* (3), 295–304.
- [15] Wasmus, S.; Küver, A. Methanol Oxidation and Direct Methanol Fuel Cells: A Selective Review. *J. Electroanal. Chem.* **1999**, *461* (1–2), 14–31.
- [16] Muradov, N. Z.; Veziroğlu, T. N. From Hydrocarbon to Hydrogen-Carbon to Hydrogen Economy. *Int. J. Hydrogen Energy* **2005**, *30* (3), 225–237.
- [17] Brandon, N. P.; Skinner, S.; Steele, B. C. H. Recent Advances in Materials for Fuel Cells. *Annu. Rev. Mater. Res.* **2003**, *33* (5), 183–213.
- [18] Grew, K. N.; Chiu, W. K. S. A Review of Modeling and Simulation Techniques across the Length Scales for the Solid Oxide Fuel Cell. *J. Power Sources* **2012**, *199*, 1–13.
- [19] Kakaç, S.; Pramuanjaroenkij, A.; Zhou, X. Y. A Review of Numerical Modeling of Solid Oxide Fuel Cells. *Int. J. Hydrogen Energy* **2007**, *32* (7), 761–786.
- [20] Ding, D.; Li, X.; Lai, S. Y.; Gerdes, K.; Liu, M. Enhancing SOFC Cathode Performance by Surface Modification through Infiltration. *Energy Environ. Sci.* **2014**, *7* (2), 552–575.
- [21] Bkour, Q.; Zhao, K.; Scudiero, L.; Han, D. J.; Yoon, C. W.; Marin-Flores, O. G.; Norton, M. G.; Ha, S. Synthesis and Performance of Ceria-Zirconia Supported Ni-Mo Nanoparticles for Partial Oxidation of Isooctane. *Appl. Catal. B Environ.* **2017**, *212*, 97–105.

- [22] Goodenough, J. B. Oxide-Ion Conductors by Design. *Nature* **2000**, *404* (6780), 821–823.
- [23] Wilde, P. J.; Catlow, C. R. A. Defects and Diffusion in Pyrochlore Structured Oxides. *Solid State Ionics* **1998**, *112* (3–4), 173–183.
- [24] van Dijk, M. P.; de Vries, K. J.; Burggraaf, A. J. Oxygen Ion and Mixed Conductivity in Compounds with the Fluorite and Pyrochlore Structure. *Solid State Ionics* **1983**, *9–10*, 913–920.
- [25] Pirzada, M.; Grimes, R. W.; Minervini, L.; Maguire, J. F.; Sickafus, K. E. Oxygen Migration in  $A_2B_2O_7$  Pyrochlores. *Solid State Ionics* **2001**, *140* (3–4), 201–208.
- [26] Shlyakhtina, A. V. Morphotropy, Isomorphism, and Polymorphism of  $Ln_2M_2O_7$ -Based ( $Ln = La-Lu, Y, Sc; M = Ti, Zr, Hf, Sn$ ) Oxides. *Crystallogr. Reports* **2013**, *58* (4), 548–562.
- [27] Shlyakhtina, A. V.; Shcherbakova, L. G. Polymorphism and High-Temperature Conductivity of  $Ln_2M_2O_7$  ( $Ln = Sm-Lu; M = Ti, Zr, Hf$ ) Pyrochlores. *Solid State Ionics* **2011**, *192* (1), 200–204.
- [28] Shlyakhtina, A. V.; Shcherbakova, L. G.; Knotko, A. V.; Steblevskii, A. V. Study of the Fluorite-Pyrochlore-Fluorite Phase Transitions in  $Ln_2Ti_2O_7$  ( $Ln=Lu, Yb, Tm$ ). *J. Solid State Electrochem.* **2004**, *8* (9), 661–667.
- [29] Norberg, S. T.; Hull, S.; Eriksson, S. G.; Ahmed, I.; Kinyanjui, F.; Biendicho, J. J. Pyrochlore to Fluorite Transition: The  $Y_2(Ti_{1-x}Zr_x)_2O_7$  ( $0.0 \leq x \leq 1.0$ ) System. *Chem. Mater.* **2012**, *24* (22), 4294–4300.
- [30] Gill, J. K.; Pandey, O. P.; Singh, K. Ionic Conductivity, Structural and Thermal Properties of Pure and  $Sr^{2+}$  Doped  $Y_2Ti_2O_7$  Pyrochlores for SOFC. *Solid State Sci.* **2011**, *13* (11), 1960–1966.
- [31] Popov, V. V.; Menushenkov, A. P.; Yaroslavtsev, A. A.; Zubavichus, Y. V.; Gaynanov, B. R.; Yastrebtsev, A. A.; Leshchev, D. S.; Chernikov, R. V. Fluorite-Pyrochlore Phase Transition in Nanostructured  $Ln_2Hf_2O_7$  ( $Ln = La-Lu$ ). *J. Alloys Compd.* **2016**, *689*, 669–679.
- [32] Minervini, L.; Grimes, R. W.; Sickafus, K. E. Disorder in Pyrochlore Oxides. *J. Am. Ceram. Soc.* **2000**, *83* (8), 1873–1878.
- [33] Tuller, H. L. Ionic Conduction in Nanocrystalline Materials. *Solid State Ionics* **2000**, *131* (1), 143–157.

- [34] Li, Y.; Kowalski, P. M.; Beridze, G.; Birnie, A. R.; Finkeldei, S.; Bosbach, D. Defect Formation Energies in  $A_2B_2O_7$  Pyrochlores. *Scr. Mater.* **2015**, *107*, 18–21.
- [35] Heremans, C.; Wuensch, B. J.; Stalick, J. K.; Prince, E. Fast-Ion Conducting  $Y_2(Zr_yTi_{1-y})_2O_7$  Pyrochlores: Neutron Rietveld Analysis of Disorder Induced by Zr Substitution. *Journal of Solid State Chemistry*. 1995, 108–121.
- [36] Popov, V. V.; Menushenkov, A. P.; Ivanov, A. A.; Yastrebtsev, A. A.; Gaynanov, B. R.; d'Acapito, F.; Puri, A. A XAFS Investigation of Amorphous-to-Crystalline and Fluorite-to-Pyrochlore Phase Transitions in  $Ln_2M_2O_7$  ( $Ln = Gd, Tb, Dy$ ;  $M = Ti, Zr$ ). *Radiat. Phys. Chem.* **2020**, *175* (August 2019), 108469.
- [37] Blanchard, P. E. R.; Liu, S.; Kennedy, B. J.; Ling, C. D.; Avdeev, M.; Aitken, J. B.; Cowie, B. C. C.; Tadich, A. Investigating the Local Structure of Lanthanoid Hafnates  $Ln_2Hf_2O_7$  via Diffraction and Spectroscopy. *J. Phys. Chem. C* **2013**, *117* (5), 2266–2273.
- [38] Zhang, F. X.; Manoun, B.; Saxena, S. K.; Zha, C. S. Structure Change of Pyrochlore  $Sm_2Ti_2O_7$  at High Pressures. *Appl. Phys. Lett.* **2005**, *86* (18), 181906.
- [39] Klee, W. E.; Weitz, G. Infrared Spectra of Ordered and Disordered Pyrochlore-Type Compounds in the Series  $RE_2Ti_2O_7$ ,  $RE_2Zr_2O_7$  and  $RE_2Hf_2O_7$ . *J. Inorg. Nucl. Chem.* **1969**, *31* (8), 2367–2372.
- [40] François, B.; Osvald, K. Pyrochlores. 111. X-Ray, Neutron, Infrared, and Dielectric Studies of  $A_2Sn_2O_7$ , Stannates. *Can. J. Chem.* **1968**, *46* (6), 859–873.
- [41] Sayed, F. N.; Grover, V.; Bhattacharyya, K.; Jain, D.; Arya, A.; Pillai, C. G. S.; Tyagi, A. K.  $Sm_{2-x}Dy_xZr_2O_7$  Pyrochlores: Probing Order-Disorder Dynamics and Multifunctionality. *Inorg. Chem.* **2011**, *50* (6), 2354–2365.
- [42] Subramanian, M. A.; Aravamudan, G.; Subba Rao, G. V. Oxide Pyrochlores - A Review. *Prog. Solid State Chem.* **1983**, *15* (2), 55–143.
- [43] Zhou, L.; Huang, Z.; Qi, J.; Feng, Z.; Wu, D.; Zhang, W.; Yu, X.; Guan, Y.; Chen, X.; Xie, L.; Sun, K.; Lu, T. Thermal-Driven Fluorite–Pyrochlore–Fluorite Phase Transitions of  $Gd_2Zr_2O_7$  Ceramics Probed in Large Range of Sintering Temperature. *Metall. Mater. Trans. A Phys. Metall. Mater. Sci.* **2016**, *47* (1), 623–630.

- [44] Jiang, C.; Stanek, C. R.; Sickafus, K. E.; Uberuaga, B. P. First-Principles Prediction of Disorder Tendencies in Pyrochlore Oxides. *Phys. Rev. B* **2009**, *79* (10), 17–21.
- [45] Li, Y.; Kowalski, P. M. Energetics of Defects Formation and Oxygen Migration in Pyrochlore Compounds from First Principles Calculations. *J. Nucl. Mater.* **2018**, *505*, 255–261.
- [46] Uno, W.; Fujii, K.; Niwa, E.; Torii, S.; Miao, P.; Kamiyama, T.; Yashima, M. Experimental Visualization of Oxide-Ion Diffusion Paths in Pyrochlore-Type  $\text{Yb}_2\text{Ti}_2\text{O}_7$ . *J. Ceram. Soc. Japan* **2018**, *126* (5), 341–345.
- [47] Tanaka, M.; Matsudaira, T.; Kawai, E.; Kawashima, N.; Matsumoto, U.; Ogawa, T.; Takeuchi, M.; Kitaoka, S. Effect of Chemical Composition on Mass Transfer in  $\text{Y}_2\text{Ti}_2\text{O}_7$  under Oxygen Potential Gradient at High Temperatures. *J. Ceram. Soc. Japan* **2021**, *129* (1), 22–31.
- [48] Cai, L.; Nino, J. C. Complex Ceramic Structures. I. Weberites. *Acta Crystallogr. Sect. B Struct. Sci.* **2009**, *65* (3), 269–290.
- [49] King, G.; Thompson, C. M.; Greedan, J. E.; Llobet, A. Local Structure of the Vacancy Disordered Fluorite  $\text{Yb}_3\text{TaO}_7$  from Neutron Total Scattering. *J. Mater. Chem. A* **2013**, *1* (35), 10487–10494.
- [50] Shamblin, J.; Feyngenson, M.; Neuefeind, J.; Tracy, C. L.; Zhang, F.; Finkeldei, S.; Bosbach, D.; Zhou, H.; Ewing, R. C.; Lang, M. Probing Disorder in Isometric Pyrochlore and Related Complex Oxides. *Nat. Mater.* **2016**, *15* (5), 507–511.
- [51] O'Quinn, E. C.; Sickafus, K. E.; Ewing, R. C.; Baldinozzi, G.; Neuefeind, J. C.; Tucker, M. G.; Fuentes, A. F.; Drey, D.; Lang, M. K. Predicting Short-Range Order and Correlated Phenomena in Disordered Crystalline Materials. *Sci. Adv.* **2020**, *6* (35), eabc2758.
- [52] Drey, D. L.; O'Quinn, E. C.; Subramani, T.; Lilova, K.; Baldinozzi, G.; Gussev, I. M.; Fuentes, A. F.; Neuefeind, J. C.; Everett, M.; Sprouster, D.; Navrotsky, A.; Ewing, R. C.; Lang, M. Disorder in  $\text{Ho}_2\text{Ti}_{2-x}\text{Zr}_x\text{O}_7$ : Pyrochlore to Defect Fluorite Solid Solution Series. *RSC Adv.* **2020**, *10* (57), 34632–34650.

## Chapter 2

### Chemical Environment of Al in Al-doped $Y_2Ti_2O_7$ : $^{27}Al$ NMR

### Spectroscopy and DFT-GIPAW Calculations

#### 2.1 Introduction

Pyrochlore oxides of the general formula  $A_2B_2O_7$ ,<sup>1</sup> where  $A$  is a trivalent rare-earth ion and  $B$  a tetravalent transition-metal ion, have an ordered structure derived from the defective-fluorite structure and are a class of materials with fascinating physical and chemical properties such as ionic conductivity,<sup>2–6</sup> low thermal conductivity,<sup>7,8</sup> oxygen storage capacity,<sup>9</sup> and high-entropy.<sup>10,11</sup> Their multifunctional properties can be tuned by controlling the ionic radius ratio of the  $A$  and  $B$  cations or incorporating a variety of cations with variable oxidation states. Elucidating the origin of their compositional flexibilities at the atomic scale has thus generated considerable research interest in the fields of materials physics and chemistry.

Typical pyrochlore oxides such as  $A_2Ti_2O_7$  ( $A = Gd, Sm, \text{ and } Y$ ) have been known to be mixed ion–electron conductors since their discovery.<sup>12</sup> Although this property has led to their consideration as a potential material for an electrode in a solid oxide fuel cell owing to their property, their poor ionic conductivity is a significant practical constraint. For this reason, a variety of approaches have been used to enhance their conductivity in recent decades. For example, Moon and Tuller have found that doping with an isovalent cation lowers the activation energy of ion transport by one-fourth order of magnitude.<sup>13</sup> Kramer and Tuller have also reported that doping with an aliovalent cation (e.g. Al and Ca) also lowers the activation energy and enhances the ionic conductivity by an order of magnitude.<sup>4</sup> Similar results for pyrochlore oxides have been reported in the literature.<sup>14–17</sup> At the

atomic scale structures,  $^{17}\text{O}$  nuclear magnetic resonance (NMR) spectroscopy by Kim and Grey<sup>18</sup> has revealed that when Ca is doped in  $\text{Y}_2\text{Ti}_2\text{O}_7$  (hereinafter referred to as  $\text{Y}_2\text{Ti}_2\text{O}_7:\text{Ca}$ ), there is an increase of vacancies around yttrium, and the local structure becomes disordered. A series of findings in  $\text{Y}_2\text{Ti}_2\text{O}_7:\text{Ca}$  has demonstrated that the local structures are closely related to oxide-ion conductivity. In contrast, few reports have characterized the defects in pyrochlore oxides when Al is doped in the pyrochlore.<sup>19,20</sup> Further investigations are thus required to elucidate the local environments in  $\text{Y}_2\text{Ti}_2\text{O}_7:\text{Al}$ .

NMR spectroscopy is a powerful method that can provide direct evidence about the chemical environment of Al. To date, many NMR-based studies of aluminum species have been reported in the literature.<sup>21-24</sup> Characterization of the dopant Al using NMR spectroscopy is nevertheless challenging because to the complex relationship between NMR parameters and local structures. The primary reason for this complexity is that the strong quadrupole interaction of aluminum nuclei ( $I = 5/2$ ) broadens lineshapes become wider, and shifts a central position of lineshapes. The deduction in many studies of local structures based on observed chemical shifts and lineshapes has therefore resulted in erroneous or misleading interpretations. The recently developed gauge-including projector augmented-waves (GIPAW) approach<sup>25</sup> and electric-field gradient (EFG) calculations<sup>26</sup> have enabled to the accurate calculation of NMR parameters,<sup>21</sup> that can provide deep insights about the chemical environments of Al-centered defects.

Herein, we investigated the chemical environments of the dopant Al in pyrochlore  $\text{Y}_2\text{Ti}_2\text{O}_7:\text{Al}$  by adopting an eclectic strategy that included NMR spectroscopy and first-principles calculations. We used solid-state  $^{27}\text{Al}$  magic-angle-spinning (MAS) NMR and two-dimensional (2D) multiple-quantum (MQ) MAS-NMR techniques to characterize the local structures of the dopants in pyrochlore. MQMAS-NMR is a technique for obtaining high-resolution spectra by averaging quadrupole broadening. To examine NMR parameters, different defect models and compounds

containing Al and Y species were calculated using first-principles calculations with the GIPAW approach. After determining the defects in  $Y_2Ti_2O_7:Al$  from a combination of experimental and calculated results, the finite-temperature stabilities of defects were evaluated based on free energy calculations that took into consideration the contributions of phonon entropy and configurational entropy to help understand the propensity for oxygen defects.

## 2.2 Experimental and Calculation methods

### 2.2.1 Materials Synthesis

1 cation% Al-doped  $Y_2Ti_2O_7$  powder was synthesized using the ultrasonic spray pyrolysis (USP) technique, which offers precise control of chemical composition of the sample. The aqueous precursor solution was prepared by mixing  $Y(NO_3)_3$  and  $TiCl_4$  solution together with  $Al(NO_3)_3 \cdot 9H_2O$ . The USP technique was then used to convert the precursor solution to a powder. The resulting powder was heated in an electric resistance furnace at 1773 K for 20 h in a Pt crucible, and the crucible was then removed from the furnace and quenched in water at room temperature. The X-ray diffraction pattern of the quenched powder showed a single phase of pyrochlore  $Y_2Ti_2O_7$ . The molar ratio of (Y+Al)/Ti was determined to be 1.041 by analysis with inductively coupled plasma optical emission spectroscopy. The powder sample therefore had a chemical composition of slightly Y-rich, or  $(Y+Al)_2Ti_{1.92}O_{7-\delta}$ .

### 2.2.2 Solid-State NMR Spectroscopy

The solid-state  $^{27}Al$  NMR experiments of the powder samples  $Y_2Ti_2O_7:Al$ ,  $\alpha-Al_2O_3$  (TM-DAR, Taimei Chem. Corp.), and  $Y_3Al_5O_{12}$  (Shin-Etsu Chemical Co., Ltd.) were performed at room temperature on a Fourier transform nuclear magnetic resonance spectrometer system (JNM-ECX 400

and JNM-ECX 600II, JEOL Ltd.). The one-dimensional (1D) NMR spectra with 9.4 tesla (T) and 14.1 T were recorded with a HXMAS probe using 4.0-mm rotors at a MAS rate of 12 kHz and a HXMAS probe using 3.2-mm rotors at a MAS rate of 20 kHz, respectively. In the 4.0 mm probe, a short  $\pi/2$  pulse of 1.5  $\mu\text{s}$  was used for excitation with a 1-s relaxation delay between each of the 2048 transients recorded. A solution of 1 M  $\text{Al}(\text{NH}_4)(\text{SO}_4)_2$  was used for referencing and calibrating the radio frequency (RF) pulses. In the 3.2-mm HXMAS probe, a short  $\pi/6$  pulse of 0.87  $\mu\text{s}$  was used for excitation with a 45-s relaxation delay between each of the 128 transients recorded. A solution of 1 M  $\text{Al}(\text{NO}_3)_3$  was used for referencing and calibrating the RF pulses. To examine the chemical environments of dopant Al in greater detail, the 2D z-filtered five-quantum (5Q) MAS-NMR spectrum with 14.1 T was also recorded in the 3.2 mm HXMAS probe at a MAS rate of 6 kHz. Four hundred eighty transients (total of 30,720 transients) were averaged using the two-pulse sequence with an excitation pulse of 5  $\mu\text{s}$ , a conversion pulse of 1.6  $\mu\text{s}$ , and a relaxation delay of 5 s.

The line shape of the MAS-NMR spectrum was characterized by three measurable quantities, viz., the chemical shift,  $\delta_{\text{iso}}$ , the coupling constant,  $C_Q := eQV_{ZZ}/h$ , and the asymmetry parameter,  $\eta_Q := (V_{XX} - V_{YY})/V_{ZZ}$ , where  $e$ ,  $h$ , and  $Q$  denote the elementary charge, Planck's constant, and the spectroscopic quadrupole moment, respectively. The EFG tensor in the principal-axis system was diagonalized with three principal components ordered such that  $\|V_{XX}\| \leq \|V_{YY}\| \leq \|V_{ZZ}\|$ . The range of  $\eta_Q$  is restricted to  $0 \leq \eta_Q \leq 1$ . The ssNake program<sup>27</sup> was used to fit the experimental peaks.

### 2.2.3 First-principles Calculations

All first-principles calculations within the framework of density functional theory (DFT) were carried out using the projector augmented wave (PAW) method,<sup>28</sup> as incorporated in the Vienna Ab initio

Simulation Package (VASP).<sup>29,30</sup> The 2s and 2p orbitals for O atoms; 3d and 4s orbitals for Ti atoms; 4s, 4p, 4d, and 5s orbitals for Y atoms; and 3s and 3p orbitals for Al atoms were explicitly treated as valence states. Generalized gradient approximation (GGA) functional with Perdew–Burke–Ernzerhof parametrization adapted for solids<sup>31</sup> (PBEsol) was used to treat exchange–correlation effects. Because the GGA functional is known to misalign the metal’s 3d states, an on-site Coulomb correction,  $U_{\text{eff}}$ , was applied to the Ti 3d electrons, where the value of  $U_{\text{eff}}$  was set to 5.4 eV<sup>32</sup> within the rotationally invariant formalism.<sup>33</sup> Atomic positions were fully optimized until Hellman–Feynman forces were smaller than  $0.001 \text{ eV} \cdot \text{\AA}^{-1}$ .

The chemical shielding tensor,  $\vec{\sigma}$ , and the EFG tensor,  $\vec{V}$ , were calculated on optimized structures with the GIPAW and PAW approaches, respectively. The  $k$ -point sampling and cutoff energies were carefully examined before choosing (Figure 2.A1 in Appendix 2.A). Brillouin zones of all structures were integrated with  $k$ -point spacings of less than  $0.3 \text{ \AA}^{-1}$  and a Gaussian smearing approach with a smearing width of 0.01 eV. The cutoff energy for the planewave basis sets was set at 700 eV. Finite-size effects of supercells on NMR parameters were examined by calculating five supercells created by expanding the primitive unit cell of 22 atoms to 44-atom, 88-atom, 176-atom, 352-atom, and 702-atom cells. Figure 2.1 shows the 44-atom and 88-atom structures of these cells. The isotropic shielding,  $\sigma_{\text{iso}}$ , was determined from the trace of the shielding tensor,  $\vec{\sigma}$ . The chemical shift,  $\delta_{\text{iso}}$ , was defined by the formalism  $\delta_{\text{iso}} := \sigma_{\text{iso}} - (\sigma_{\text{iso}}^{\text{ref}} - \tilde{\delta}_{\text{iso}}^{\text{exp}})$ , where the reference chemical shielding,  $\sigma_{\text{iso}}^{\text{ref}}$ , and the correction term,  $\tilde{\delta}_{\text{iso}}^{\text{exp}}$ , were set to the calculated and experimental value of the six-coordinated Al in yttrium aluminum garnet (YAG)  $\text{Y}_3\text{Al}_5\text{O}_{12}$ , respectively. The electric quadrupole moment,  $eQ$ , was set to  $146.6 \text{ mb}^{34}$  for  $^{27}\text{Al}$  nuclei. The calculated EFG tensor was used to evaluate the quadrupolar coupling constant and the asymmetry parameter.

To examining the dopants on finite-temperature stability, defect calculations including phonon contributions were performed. Initially, the finite-size and exchange–correlation effects on defect

formation energies were evaluated by calculating five supercells with three functionals: GGA-PBEsol, GGA-PBEsol+U, and hybrid Heyd–Scuseria–Ernzerhof<sup>35</sup> (HSE06). Phonon calculations were performed in the harmonic approximation using a 176-atom supercell with finite displacements of 0.01 Å. the GGA-PBEsol+U functional was adopted to reduce the computational demand. The interatomic force constants were calculated by the Parlinski–Li–Kawazoe method,<sup>36</sup> as implemented in the phonopy code.<sup>37,38</sup>

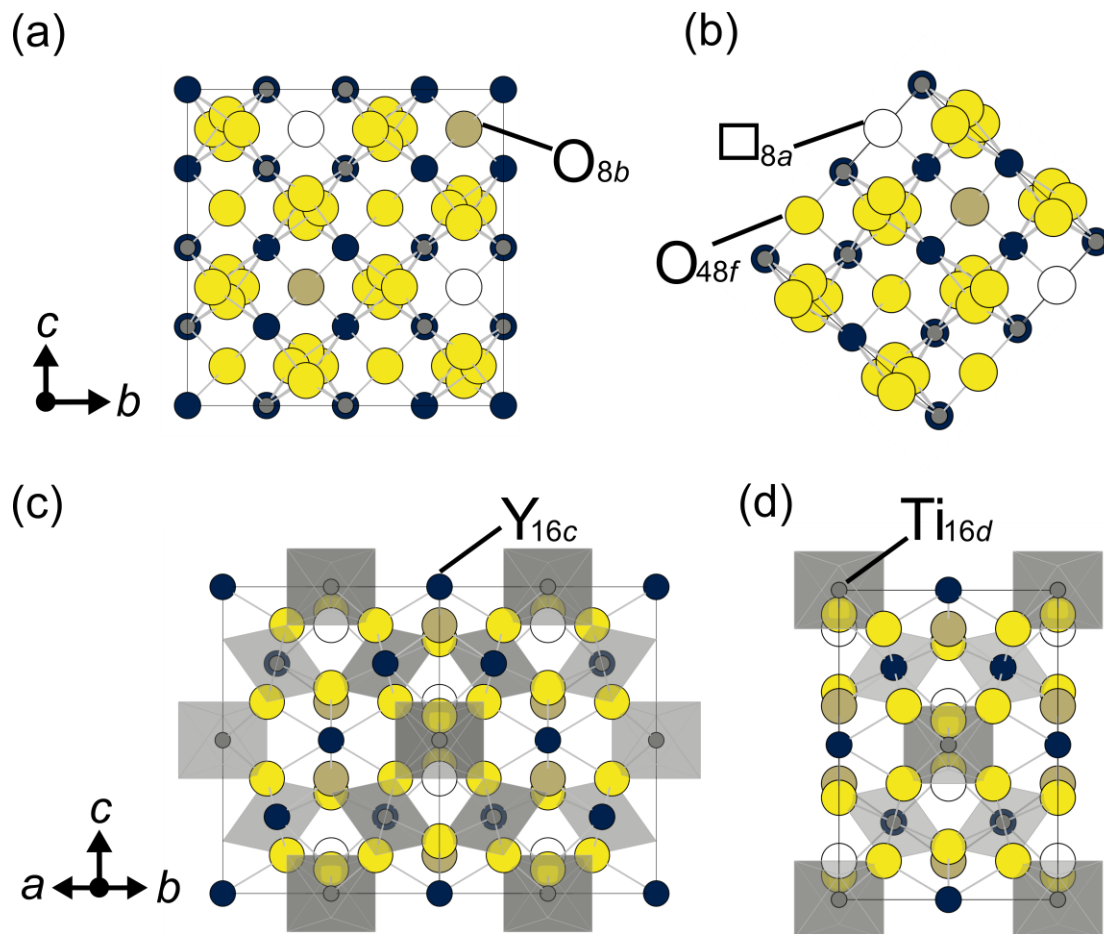


**Figure 2.1.** Crystal structures with (a, c) an 88-atom cubic cell and (b, d) a 44-atom cell in the (a, b) [100] and (c, d) [110] directions. Navy, gray, yellow and dark yellow spheres denote Y<sub>16c</sub>, Ti<sub>16d</sub>, O<sub>48f</sub> and O<sub>8b</sub> atoms, respectively, and white spheres denote vacant 8a sites labeled □<sub>8a</sub>.

## 2.3 Results

The  $Y_2Ti_2O_7$  and  $Al_2O_3$  compositions formed into a solid solution,  $Y_2Ti_2O_7:Al$ , at high temperatures, where the end-member compositions were  $Y_2Ti_2O_7$ ,  $\alpha-Al_2O_3$ , and  $Y_3Al_5O_{12}$ .<sup>39</sup> Because these structures may be formed as secondary phases, two oxides,  $\alpha-Al_2O_3$  and  $Y_3Al_5O_{12}$ , together with  $Y_2Ti_2O_7:Al$  were prepared for the MAS-NMR experiments. We also performed first-principles calculations for structural optimization, and Table 2.1 lists the resulting unit-cell parameters. The coordination numbers (CNs) of the Al cation were six in corundum  $\alpha-Al_2O_3$  and four and six in  $Y_3Al_5O_{12}$ .

**Table 2.1.** Calculated unit-cell parameters of  $\alpha-Al_2O_3$ ,  $Y_3Al_5O_{12}$ , and  $Y_2Ti_2O_7$ .

crystal	$\alpha-Al_2O_3$	$Y_3Al_5O_{12}$	$Y_2Ti_2O_7$
space group	$R\bar{3}c$	$Ia\bar{3}d$	$Fd\bar{3}m$
lattice const. (Å)	$a = 4.8051$ $c = 13.1122$	$a = 12.1000$	$a = 10.2256$
formula units, Z	6	8	8
volume / Z (Å <sup>3</sup> )	43.697	221.4323	133.651
site coordinates	Al (0, 0, z) O (x, 0, 1/4) $x = 0.3062$ $z = 0.3522$	Y (1/8, 0, 1/8) Al (0, 0, 0) Al' (3/8, 0, 1/4) O (x, y, z) $x = 0.2802$ $y = 0.1009$ $z = 0.1995$	Y (0, 0, 0) Ti (1/2, 1/2, 1/2) O (x, 1/8, 1/8) O' (1/8, 1/8, 1/8) $\square$ (1/8, 1/8, 5/8) $x = 0.9182$

$Y_2Ti_2O_7$  has a pyrochlore structure with cubic space group  $Fd\bar{3}m$ . The structure, which is also expressed as  $Y_2Ti_2O_6O'\square$ , is illustrated in Figure 2.1. In the ideal pyrochlore, there are two cation and three anion sites. Four of the sites are occupied: Y at  $16c$ , Ti at  $16d$ , O at  $48f$ , and O' at  $8b$ . These sites

are crystallographically nonequivalent in Wyckoff notation. The  $8a$  ( $1/8, 1/8, 5/8$ ) site is unoccupied, viz., the intrinsic vacancy, which is labeled  $\square$ . The  $16c$  and  $16d$  sites have different chemical environments, viz., the  $16c$  and  $16d$  sites are surrounded by six  $48f$  and two  $8b$  sites and by six  $48f$  and two  $8a$  sites, respectively. The CNs of the Y and Ti cations in  $Y_2Ti_2O_7$  are therefore eight and six, respectively.

### 2.3.1 $^{27}\text{Al}$ NMR Spectroscopy

The NMR spectra commonly exhibit a complex line shape due to the dipole magnetic interaction and quadrupole interaction in the case of the spin ( $I = 5/2$ ) of the aluminum nuclei. Of these interactions, the dipole magnetic interaction and the first-order effect of the quadrupole interaction can be averaged using the MAS measurement method. The result is that the second-order effect remains. The line shape due to the second-order effect of the quadrupole interaction has been formulated as follows:<sup>40</sup>

$$\begin{aligned} v_{m,m+1} - v_L &= v_{\text{iso}} + v(\alpha, \beta, \eta) \\ &= -\frac{v_Q^2}{6v_L} \left\{ \begin{aligned} &\frac{1}{5}[I(I+1) - 9m(m+1) - 3] \left(1 + \frac{\eta_Q^2}{3}\right) \\ &+ \left[(I+1) - \frac{17}{3}m(m+1) - \frac{13}{6}\right] g_{\text{MAS}}(\alpha, \beta, \eta_Q) \end{aligned} \right\} \end{aligned} \quad (1)$$

where,  $v_{m,m+1}$ ,  $v_{\text{iso}}$ ,  $v_L$ , and  $v_Q := 3C_Q/2I(2I-1)$  denote the resonance frequency between  $m$  and  $m+1$  Zeeman levels, the isotropic second-order quadrupole shift, the Lamour frequency, and the quadrupole frequency, respectively. The parameter  $m$  denotes the magnetic quantum number associated with the specific Zeeman level, where the central transition corresponds to  $m = -1/2$ . The parameters  $\alpha$  and  $\beta$  denote spherical polar angles. Equation 1 makes it possible to obtain NMR parameters from experimental spectra by spectral fitting and to plot a spectrum from the NMR parameters. Equation 1 also indicates that the quadrupolar coupling constant and the Lamour frequency of quadrupole interaction are directly proportional to and inversely proportional to the

magnetic field strength. These dependencies on magnetic field strength are a characteristic of electric quadrupole interactions.

The  $^{27}\text{Al}$  MAS-NMR spectra of  $\alpha\text{-Al}_2\text{O}_3$ ,  $\text{Y}_3\text{Al}_5\text{O}_{12}$ , and  $\text{Y}_2\text{Ti}_2\text{O}_7\text{:Al}$  were recorded to study the local environment of aluminum. Figure 2.2a and 2.2b shows the  $^{27}\text{Al}$  MAS-NMR spectra of  $\text{Y}_2\text{Ti}_2\text{O}_7\text{:Al}$  at different magnetic field strengths of 9.4 T and 14.1 T, respectively. Two signals of  $^{27}\text{Al}$  at round 17 and 22 ppm are apparent in the spectra of  $\text{Y}_2\text{Ti}_2\text{O}_7\text{:Al}$ . The fact that the chemical shifts of both signals are in the range 0–40 ppm suggests that  $\text{Y}_2\text{Ti}_2\text{O}_7\text{:Al}$  contains five- or six-coordinated aluminum. The line shape of the major signal with double peaks at 15 and 20 ppm is a characteristic of a second-order electric quadrupole interaction. The effect of the quadrupole interaction could also be confirmed from the fact that the line shape was independent of the magnetic field strength. When the strength of the applied magnetic field was increased, the peak position shifted downfield, and the linewidth of the signals became narrower. In contrast, the position of the weak signal at 20 ppm was almost unchanged by an increase of the applied magnetic field. As a result, its quadrupole interaction coupling constant was much smaller. The fact that the central position and the line shape of this weak signal matched those of  $\alpha\text{-Al}_2\text{O}_3$  (Figure 2.2b and 2.2c) indicated that the sintered sample contained a small amount of an unreacted  $\alpha\text{-Al}_2\text{O}_3$ .

Examination of the spectra of  $\text{Y}_2\text{Ti}_2\text{O}_7\text{:Al}$  revealed that the major signal had a weak shoulder at lower chemical shifts. This shoulder could not be explained by the signal peak of a defect. The implication is that there was another defect or crystal in the sample. We therefore performed line shape fitting of the NMR spectra of  $\text{Y}_2\text{Ti}_2\text{O}_7\text{:Al}$  observed at 9.4 and 14.1 T on the assumption that there were three types of aluminum. Table 2.2 lists the NMR parameters that we obtained, and Figure 2.2b shows the deconvoluted line shapes. We also performed line shape fitting of the NMR spectra of  $\text{Al}_2\text{O}_3$  and  $\text{Y}_3\text{Al}_5\text{O}_{12}$ . Table 2.2 lists the parameters that we obtained.

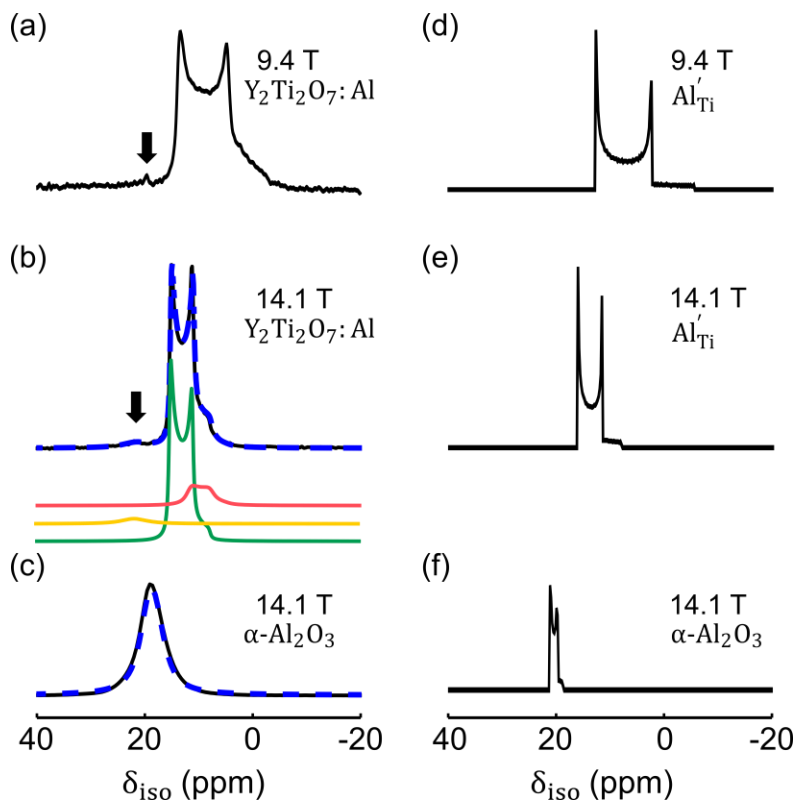


**Figure 2.2.**  $^{27}\text{Al}$  MAS-NMR (a–c) experimental and (d–f) simulated spectra. The experimental spectra of  $\text{Y}_2\text{Ti}_2\text{O}_7:\text{Al}$  were recorded at 9.4 T (a) and 14.1 T (b), and the spectra of  $\alpha\text{-Al}_2\text{O}_3$  was recorded at 14.1 T (c). The simulated NMR spectra of  $\text{Al}'_{\text{Ti}}$  in  $\text{Y}_2\text{Ti}_2\text{O}_7:\text{Al}$  at 9.4 T (a) and 14.1 T (b) and  $\text{Al}_2\text{O}_3$  at 14.1 T (c), calculated using NMR parameters from first-principles calculations. In (a, b), the black arrows indicate the weak signal corresponding to  $\alpha\text{-Al}_2\text{O}_3$ . In (b, c), The NMR spectra recorded at 14.1 T were deconvoluted by Lorentzian line shape: experimental spectra (black), simulated spectra (blue dashed), and deconvoluted signals (green, yellow, and red).

To identify the NMR signals of  $\text{Y}_2\text{Ti}_2\text{O}_7:\text{Al}$  in greater detail, we performed 5QMAS-NMR experiments. Figure 2.3 shows the 2D 5QMAS-NMR spectrum of  $\text{Y}_2\text{Ti}_2\text{O}_7:\text{Al}$  recorded at 14.1 T after Fourier transformation and a shearing transformation. The alignment of all peaks with the MAS axis indicated that the dopant Al was in a highly crystalline sample. The double peaks observed in the 1D MAS-NMR spectra were also apparent at 11.1 and 14.7 ppm in this spectrum. In addition, the appearance of extra double peaks at 8.5 and 12.5 ppm confirmed the existence of another aluminum

in  $Y_2Ti_2O_7:Al$ . This observation demonstrated that the resolution of MQMAS-NMR exceeded that of MAS-NMR. However, the fact that the weak peak of  $\alpha-Al_2O_3$  at  $\sim 22$  ppm could not be seen in this spectrum was probably due to the poor sensitivity of the MQMAS-NMR.

**Table 2.2.** Experimental and calculated chemical shifts,  $\delta_{iso}$ , quadrupolar coupling constants,  $C_Q$ , and asymmetry parameters,  $\eta_Q$ , of  $\alpha-Al_2O_3$ ,  $Y_3Al_5O_{12}$ , and  $Y_2Ti_2O_7:Al$ .

sample structures	or method	CN <sup>a</sup> : defect type	$\delta_{iso}$ (ppm)	$C_Q$ (MHz)	$\eta_Q$	reference
$\alpha-Al_2O_3$	expt.	VI	21.07 <sup>c</sup>	2.39	0	23
	expt. (14.1 T) <sup>b</sup>	VI	20.76	2.878	0.301	this work
	DFT	VI	22.96	2.135	0.00	this work
$Y_3Al_5O_{12}$	expt.	IV	84.7 <sup>c</sup>	6.02	0.00	23
		VI	6.77 <sup>c</sup>	0.63	0.00	23
	expt. (14.1 T) <sup>b</sup>	IV	81.45	6.076	0.00	this work
		VI	6.77	2.252	0.60	this work
		DFT	IV	78.59	-6.376	0.00
	DFT	VI	6.77	-0.969	0.00	this work
$Y_2Ti_2O_7:Al$	expt. (14.1 T) <sup>b</sup>	VI	22.76	2.200	0.33	this work
		VI	16.39	3.752	0.00	this work
		VI	12.80	3.636	0.11	this work
	DFT	VI: $Al'_{Ti}$	18.55	3.98	0.02	this work
		V: $\{Al'_{Ti} \cdot v_{O,48f}''\}$	48.93	7.34	0.11	this work
		VI: $Al'_{Ti}$ $+ \{v_{O}'' \cdot O''_{i,2NN}$ $\cdot v_{O}''\}$	18.79	6.93	0.41	this work
		VIII: $Al^{\times}_{\tilde{Y}}$	-3.94	31.79	0.02	this work

<sup>a</sup> CN denotes the coordination number of Al species.

<sup>b</sup> Measurement magnetic field strength.

<sup>c</sup> Chemical shifts in the previous work are given relative to the six-coordinated Al in  $Y_3Al_5O_{12}$ , which is set to 6.77 ppm.

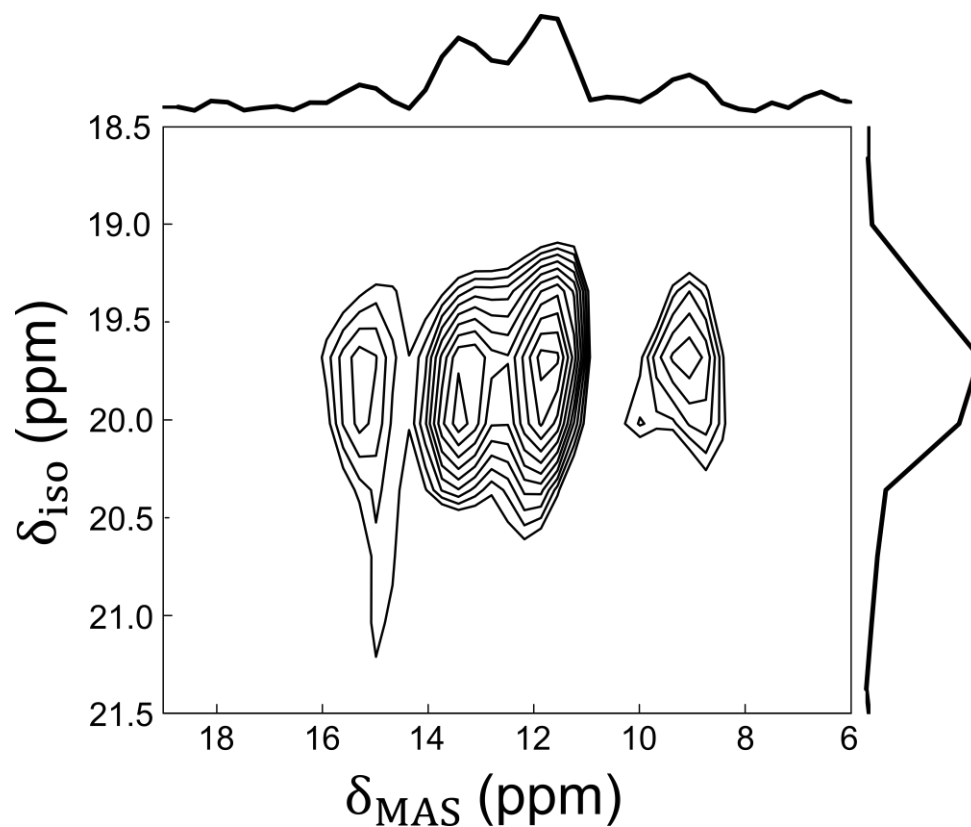


**Figure 2.3.** 5QMAS NMR spectrum of  $^{27}\text{Al}$  in  $\text{Y}_2\text{Ti}_2\text{O}_7:\text{Al}$  recorded at 14.1 T.

### 2.3.2 First-principles Calculations of NMR Parameters

Complex oxygen vacancies, apart from cation substitution, are formed in the pyrochlore: (1) an oxygen vacancy ( $v_{48f}^{\ddot{\cdot}}$ ) using Kröger–Vink notation, and (2) an association of an anion Frenkel pair and the oxygen vacancy ( $\{v_{\text{O},48f}^{\ddot{\cdot}} \cdot \text{O}_{i,8a}^{\prime\prime} \cdot v_{\text{O},48f}^{\ddot{\cdot}}\}^{\ddot{\cdot}}$ ). The curly brackets here represent the association of defects. The former association is formed by a removing an O on the 48*f* site which is called a “single vacancy”. The latter is formed by removing an O and movement of a neighbor O onto the interstitial 8*a* site. This association is called a “split vacancy”. The other oxygen vacancy ( $v_{\text{O},8b}^{\ddot{\cdot}}$ ) is not taken into account because it is energetically much less stable than the  $v_{\text{O},48f}^{\ddot{\cdot}}$  by about 3 eV.

This trend is consistent with our previous results of first-principles molecular dynamics simulations<sup>32</sup> (FPMD) and Rietveld analysis;<sup>41</sup> it is also similar to the results of other pyrochlore cases, e.g.,  $\text{Y}_2\text{Sn}_2\text{O}_7$ <sup>42,43</sup> and  $\text{Yb}_2\text{Ti}_2\text{O}_7$ .<sup>44,45</sup>

To calculate the NMR parameters of dopant Al in  $\text{Y}_2\text{Ti}_2\text{O}_7:\text{Al}$ , we modeled four defects, including the defect associated (Figure 2.4 and Figure 2.A2 in Appendix 2.B): (1) a defect in the substitution of Al into Ti ( $\text{Al}'_{\text{Ti}}$ ); (2) a defect cluster with  $\text{Al}'_{\text{Ti}}$  and an oxygen vacancy located at the first nearest neighbor (1NN) of the 48*f* site ( $\{\text{Al}'_{\text{Ti}} \cdot v_{\text{O},48f}\}'$ ); (3) a defect cluster with  $\text{Al}'_{\text{Ti}}$  and the split vacancy at the second nearest neighbor (2NN) of the 8*a* site ( $\text{Al}'_{\text{Ti}} + \{v_{\text{O},48f} \cdot \text{O}''_{i,8a,2\text{NN}} \cdot v_{\text{O},48f}\}''$ ); and (4) a defect in the substitution of Al into Y ( $\text{Al}^\times_{\text{Y}}$ ). The defects in cases 1 and 4 are the simple substitution models of cations, which are the same as those previously reported in the literature. For the  $\text{Al}'_{\text{Ti}}$  defect, models 2 and 3 were considered in greater detail to examine the influence of an oxygen vacancy. The distance between the  $\text{Al}'_{\text{Ti}}$  defect and the oxygen vacancy was longer in case 3 than in case 1, and shorter in case 3 than in case 2. In case 2, the CN of Al was reduced from six to five, whereas in cases 1 and 3 the CN remained six.

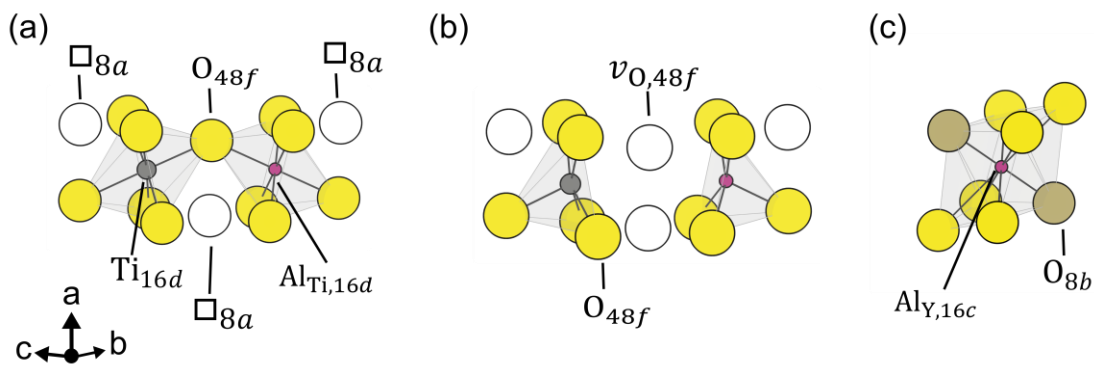


**Figure 2.4.** Local environments of defects (a)  $\text{Al}'_{\text{Ti}}$ , (b)  $\{\text{Al}'_{\text{Ti}} \cdot v_{\text{O},48f}\}'$ , and (c)  $\text{Al}^\times_{\text{Y}}$ . Gray, pink, yellow and dark yellow spheres denote Ti, Al,  $\text{O}_{48f}$  and  $\text{O}_{8b}$  atoms, respectively and white spheres denote oxygen vacant sites.

To examine the correlation between cell sizes and NMR parameters, we performed NMR calculations for the four defects in  $Y_2Ti_2O_7:Al$  as described section 2.3.1. The resulting NMR parameters are plotted in Figure 2.5. The chemical shifts and coupling constants decreased linearly as the concentration of Al decreased in each case. In contrast, the asymmetry parameters remained almost constant. In these calculations, the NMR parameters at 1 cation% were extrapolated by fitting a function of the form  $aL^{-1} + b$ , where  $L^{-1}$  is the lattice constant before a defect is introduced a defect. We also performed NMR calculations for  $\alpha-Al_2O_3$  and  $Y_3Al_5O_{12}$ , and the resulting NMR parameters are summarized in Table 1 together with those for  $Y_2Ti_2O_7:Al$ . Here,  $\tilde{\delta}_{iso}^{exp}$  was set at 6.77 ppm, which is the experimental value of six-coordinated Al in YAG. The NMR parameters of  $\alpha-Al_2O_3$  and  $Y_3Al_5O_{12}$ , obtained from first-principles calculations, were in good agreement with our experimental and the previously reported values.<sup>23,46</sup>

These results showed that the chemical shifts correlate roughly with the inverse order of the CNs. In other words, the chemical shifts of five-coordinated and eight-coordinated Al shifted downfield (around 40 ppm) and upfield (around  $-10$  ppm), respectively, whereas the shift of six-coordinated Al remained at  $\sim 20$  ppm. Out of all the different defect types we considered, the NMR parameters of the  $Al'_{Ti}$  system were in best agreement with the experimental values for  $Y_2Ti_2O_7:Al$ . This agreement indicates that the dopant Al was predominantly substituted onto the Ti site, a conclusion consistent with the results of previous studies.<sup>19</sup> The fact that the quadrupolar coupling constants of defects  $\{Al'_{Ti} \cdot v_{O,48f}''\}$  and  $Al_Y^{\times}$  were larger than that of  $Al'_{Ti}$  suggests that the quadrupolar interaction of those defects strengthened when the local symmetry decreased. A comparison of the results for  $Al'_{Ti}$  with those of its defect cluster  $\{Al'_{Ti} \cdot v_{O,48f}''\}$  revealed that the association of  $Al'_{Ti}$  with a  $v_{O,48f}''$  oxygen vacancy decreases its chemical shift and increases its coupling constant. The asymmetry parameter also increases slightly.

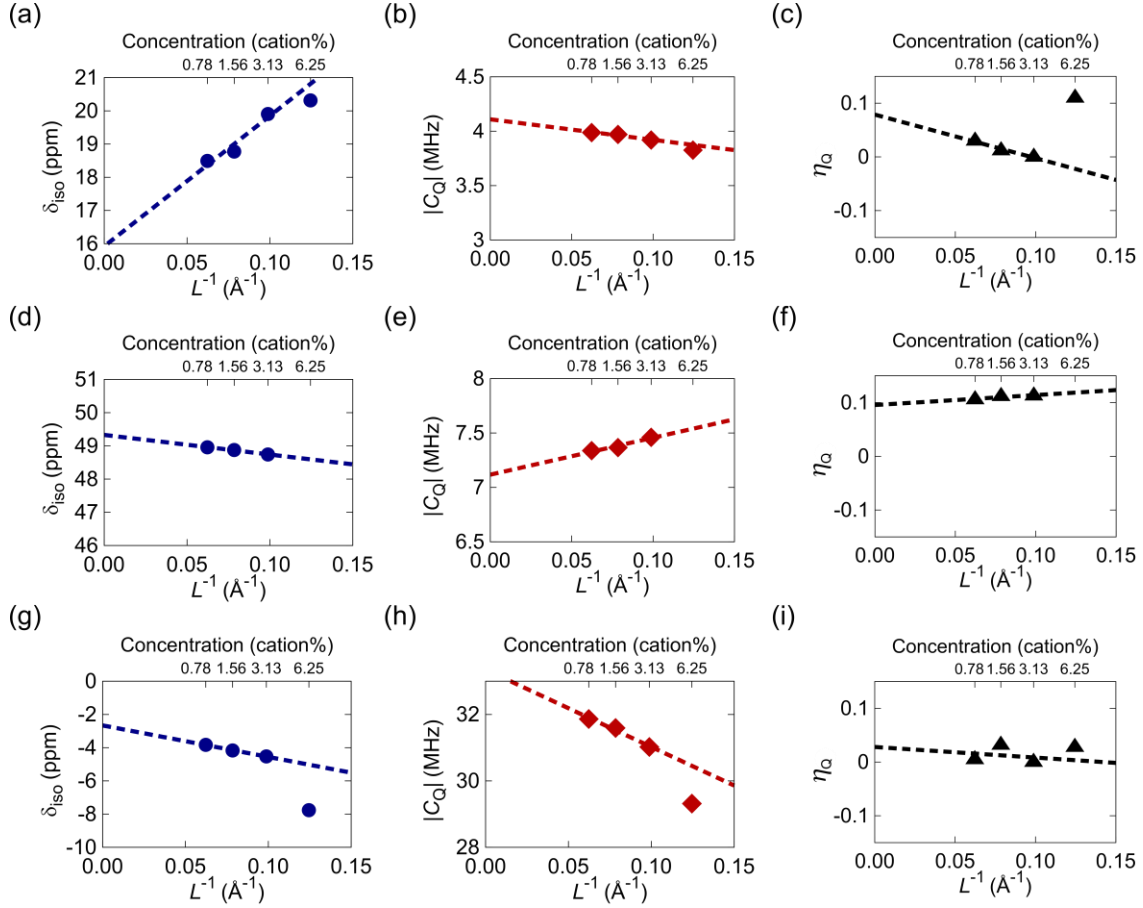


**Figure 2.5.** NMR parameters of (a–c)  $\text{Al}'_{\text{Ti}}$ , (d–f)  $\{\text{Al}'_{\text{Ti}} \cdot v_{\text{O},48f}^{\ddot{}}\}$ , and (g–i)  $\text{Al}^{\times}_{\text{Ti}}$  as a function of the reciprocal lattice constant,  $L^{-1}$ , from first-principles calculations: (a, d, g) chemical shifts,  $\delta_{\text{iso}}$ ; (b, e, h) coupling constants,  $C_Q$ ; and (c, f, i) asymmetry parameters,  $\eta_Q$ . The dashed line is a line of best fit that represents three points in the range corresponding to  $L^{-1}$  less than  $0.10 \text{ \AA}^{-1}$ .

### 2.3.3 Defect Stability

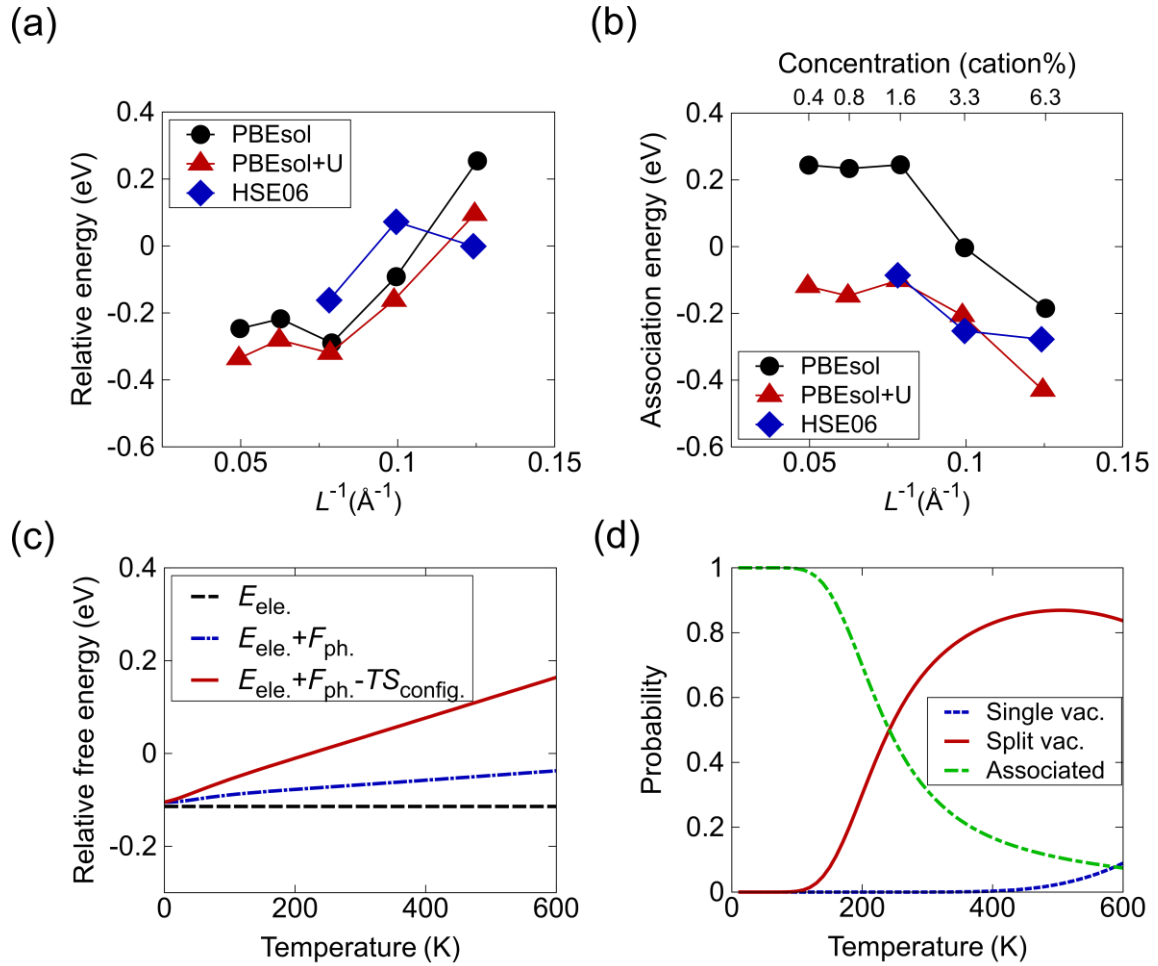
To evaluate the energetic stability of defects in  $\text{Y}_2\text{Ti}_2\text{O}_7:\text{Al}$ , we calculated their relative energies. In general, there were two concerns to associate with calculating the defect energies: the small cell size and the accuracy of the GGA functional. We therefore examined the effects of cell size and exchange–correlation functionals on the calculated energies.

Figure 2.6a shows the relative energy of the split vacancy ( $\{v_{\text{O},48f} \cdot \text{O}_{i,8a}'' \cdot v_{\text{O},48f}\}$ ) with respect to the single vacancy ( $v_{\text{O},48f}$ ). The relative energies have an  $L^{-1}$  dependence, and the proportionality was negative when  $L^{-1}$  exceeded  $0.078 \text{ \AA}^{-1}$ , where  $L$  is an ideal lattice constant of a supercell. When  $L^{-1}$  was less than  $0.078 \text{ \AA}^{-1}$ , the relative energies converged to a certain value for each exchange–correlation functional. The fact that the relative energies were negative, suggested that a split vacancy was preferred to a single vacancy at 0 K. This result was consistent with our previous work using FPMD simulations, which showed that the split vacancy was predominantly formed at low temperatures in the pyrochlore.<sup>32</sup>

Figure 2.6b shows the association energies between a defect  $\text{Al}'_{\text{Tl}}$  and an oxygen vacancy. The association energies converged to a certain value for each exchange–correlation functional when  $L^{-1}$  was less than  $0.078 \text{ \AA}^{-1}$ . The association energies at  $L^{-1} = 0.078 \text{ \AA}^{-1}$  obtained using the PBEsol, PBEsol+U, and HSE06 functionals were 0.25 eV,  $-0.10 \text{ eV}$ , and  $-0.09 \text{ eV}$ , respectively. The fact that the association energies of the PBEsol+U were close to that obtained using the HSE06, differed from the results for PBEsol. We attributed this difference in energies using the PBEsol and the HSE06 to the poor description of the exchange interaction obtained with the GGA functional. This deficiency of the GGA functional is well known. The PBEsol+U was therefore more suitable than the PBEsol

for the electronic calculation of defects because of the improvement of the former by the +U correction.

The negative association energy indicated that oxygen vacancies generated by doping Al were preferentially associated with  $Al'_{Ti}$  at 0 K. However, this defect cluster was incompatible with the result obtained from the combined NMR observations and calculations. This incompatibility



**Figure 2.6.** Relative energies of (a) the split vacancy and (b) the associated defect  $\{Al'_{Ti} \cdot v_{\ddot{O}}\}$  with respect to  $Al'_{Ti} + \{v_{\ddot{O}} \cdot O''_{i,2NN} \cdot v_{\ddot{O}}\}$ . (c) Relative free energies of  $\{Al'_{Ti} \cdot v_{\ddot{O},48f}\}$  with respect to  $Al'_{Ti} + v_{\ddot{O},48f}$  with and without phonon and configurational contributions. (d) Probabilities of the single vacancy (blue dashed line), split vacancy (red line) and the associated defect (green dashed line).

indicated that  $\text{Al}'_{\text{Ti}}$  rather than  $\{\text{Al}'_{\text{Ti}} \cdot v_{\text{O},48f}\}$  was more stable. There was thus a possibility that the order of the stability of defects at finite temperature differed from that at temperatures approaching 0 K.

To assess the energetical stability of defects at finite temperature, we calculated configurational and harmonic phonon entropies. If a supercell contains one  $\text{Al}'_{\text{Ti}}$  and one oxygen vacancy, the Helmholtz free energy of  $\{\text{Al}'_{\text{Ti}} \cdot v_{\text{O}}\}$  relative to  $\text{Al}'_{\text{Ti}} + \{v_{\text{O}} \cdot \text{O}''_i \cdot v_{\text{O}}\}$  is given by Equation 2:

$$\Delta F(T) = F[\{\text{Al}'_{\text{Ti}} \cdot v_{\text{O}}\}] + F[\cdot] - F[\text{Al}'_{\text{Ti}}] - F[\{v_{\text{O}} \cdot \text{O}''_i \cdot v_{\text{O}}\}] \quad (2)$$

where,  $F[X^q]$  is the free energy of defect  $X$  with charge  $q$ . The chemical potentials of electrons and some atoms cancel out in Equation 2. The configurational entropy,  $S_{\text{conf}}$ , in this system is defined as  $k_{\text{B}} \ln g$ , where  $g$  called the geometrical factor or on-site configurational degeneracy and is equal to the number of possible configurations.<sup>47-49</sup> The  $g$  values of  $\{\text{Al}'_{\text{Ti}} \cdot v_{\text{O},48f,1\text{NN}}\}$ ,  $\text{Al}'_{\text{Ti}} + \{v_{\text{O}} \cdot \text{O}''_i \cdot v_{\text{O}}\}$ , and  $\text{Al}'_{\text{Ti}} + v_{\text{O}}$  are 6,  $12n-6$ , and  $6n-6$ , respectively, where  $n$  is the number of formula units. Thus, the system 1 cation% Al corresponds to  $n = 25$ . Here, the plus sign indicates that the defects are separated from each other.

Figure 2.6c compares the relative free energies of the defect clusters calculated with and without phonon and configurational entropy contributions. The plots show that relative free energy is higher when phonon and configurational entropies are included, with the configurational entropy contribution larger than the phonon contribution. The relative free energy positively correlated with temperature, and it changes from negative to positive at  $\sim 300$  K. This sign inversion indicates that at temperatures higher than room temperature, the isolated oxygen defect is energetically preferred.

The abundance ratio of defects can be further investigated by calculating the thermodynamic probabilities,  $P$ , of the three types of defects from the above free energies on the assumption that the three-level system with those free energies is in the canonical ensemble at temperature  $T$ . Because

the split vacancy involves two  $48f$  sites but the single vacancy only one, the weight of the split vacancy is twice that of the single vacancy.

Figure 2.6d shows the probabilities of the three types of defects:  $\{Al'_{Ti} \cdot v_{O}\}'$ ,  $Al'_{Ti} + \{v_{O} \cdot O''_i \cdot v_{O}\}''$ , and  $Al'_{Ti} + v_{O,48f}$ . At low temperatures the probability of the defect cluster is equal to unity, i.e., the defect cluster is formed almost exclusively. At elevated temperatures, the probability of the defect cluster decreases from 1.0 to 0.1 with an increase in temperature from 100 K to 300K, whereas the probability of the isolated split vacancy increases from 0.0 to 0.9. This behavior indicates that the split vacancy is preferentially isolated rather than the defect cluster at room temperature. At temperatures higher than 500 K, the gradual increase of the probability of a single vacancy, results in  $Al'_{Ti}$  becoming isolated.

## 2.4 Discussion

Our NMR experiments and first-principles calculations indicate that the dopant Al predominantly substituted onto Ti sites. This conclusion is physically reasonable because the Shannon's ionic radius of the  $Al^{3+}$  cation (0.535 Å) is much closer to that of the  $Ti^{4+}$  cation (0.605 Å) than that of the  $Y^{3+}$  cation (1.019 Å).<sup>50</sup> This result implies that oxygen vacancies are generated in the pyrochlore structure by Al doping to maintain charge balance, and provides an explanation for the increase of the prefactor of the oxide-ion conductivity by Al doping.<sup>6</sup> Our results demonstrate that NMR parameters can serve as a fingerprint of the chemical environment of the Al dopant. In contrast, Ohtsuka et al.<sup>19</sup> have reported that Al occupies  $Y^{3+}$  and  $Ti^{4+}$  sites in an approximate ratio of 3:7 in  $Y_2Ti_2O_7:Al$ . They used statistical atom-location by channeling-enhanced microanalysis (ALCHEMI) method,<sup>51</sup> which is a method used to determine sites of impurity atoms. In our MAS-NMR spectra, a signal corresponding to  $Al'_Y$  could not be seen at a shift of  $-100$  ppm. Because spinning sidebands appeared in the same

region, these signals may have overlapped. This possibility illustrates the limitation of MAS-NMR experiments to elucidate the local structure of defects exhibiting downfield signals. In addition, the fact that the extra signals observed by 1D- and 2D-MASNMR spectroscopies (Figures 2.2 and 2.3) cannot be identified, suggests that the more complex defect states may also exist in this oxide.

NMR experiments also indicated that the oxygen vacancy generated by the aliovalent cation  $\text{Al}^{3+}$  doping was not associated with oxygen vacancies in the sample sintered at high temperatures because no peaks derived from five-coordinated aluminum in the MAS-NMR spectra appeared. This experimental result is consistent with our statistical analysis using first-principles calculations, wherein all point defects separate was at temperatures higher than 500 K. However, the fact that the defect clusters were stable at room temperature is a concern for practical use as a mixed ion–electron conductor because the activation energy of oxide-ion diffusion may increase during long-term use as a result of trapping of oxygen vacancies. This kind of deterioration in oxide-ion conductivity has been experimentally confirmed in the case  $\delta\text{-Bi}_2\text{O}_3$ .<sup>52</sup>

It seems appropriate to note a few limitations of the calculations in our study. First, other defects, such as  $\text{Y}'_{\text{Ti}}$ ,  $\text{Ti}'_{\text{Ti}}$ , and  $\text{Ti}'_{\text{Y}}$ , were not considered. If an oxygen vacancy is preferentially associated with one of these defects, the energetics may change. However, these cation exchange defects likely have high formation energies and thus are unlikely to be present in significant concentrations. It may be possible to investigate a wider range of defect states quantitatively by calculating the thermal equilibrium in the ground canonical ensemble as has been done for systems such as  $\text{Y}_2\text{O}_3\text{-TiO}_2$ ,<sup>41</sup>  $\text{ZnO}$ ,<sup>53</sup> and metallic Al.<sup>47</sup> Second, the vibrational entropy was calculated based on the harmonic approximation. Anharmonic vibrations are known to make significant contributions to the free energy at high temperatures, and thus a more accurate treatment will require the anharmonic vibrational contributions to be taken into account e.g. UP-TILD approach<sup>54</sup> or the recently developed TU-TILD approach.<sup>48</sup> We intend to attempt such calculations in the near future.

## 2.5 Conclusions

To investigate the chemical environments in pyrochlore  $Y_2Ti_2O_7:Al$ , we performed  $^{27}Al$  MAS-NMR experiments and first-principles calculations of  $\alpha-Al_2O_3$ ,  $Y_3Al_5O_{12}$ , and  $Y_2Ti_2O_7:Al$ . The MAS-NMR spectra of the  $Y_2Ti_2O_7:Al$  sample showed three signals in pyrochlore  $Y_2Ti_2O_7:Al$ . The good agreement between the NMR parameters of the major signal and those of  $Al'_{Ti}$  based on NMR parameters derived from first-principles calculations corroborated that fact that the dopant Al predominantly substituted onto Ti sites. In contrast, the weak signal found to correspond with  $\alpha-Al_2O_3$  indicated that the  $Y_2Ti_2O_7:Al$  sample was synthesized using a USP technique and contained a small amount of unreacted  $\alpha-Al_2O_3$ . These findings demonstrated the utility of combining NMR experiments and first-principles calculations to determine the chemical environments of defects in oxides. We also examined the thermodynamic stability of defects in pyrochlore  $Y_2Ti_2O_7:Al$  using first-principles calculations. Those calculations showed that the  $Al'_{Ti}$  defect preferentially associated with the oxygen vacancy at temperatures lower than 500 K, whereas at higher temperatures the  $Al'_{Ti}$  defect and oxygen vacancy were preferentially isolated. These results suggested the importance of defect states in the design of nonstoichiometric pyrochlore oxides for mixed ion–electron conductors at room temperature.

## Appendix 2.A Convergence Test

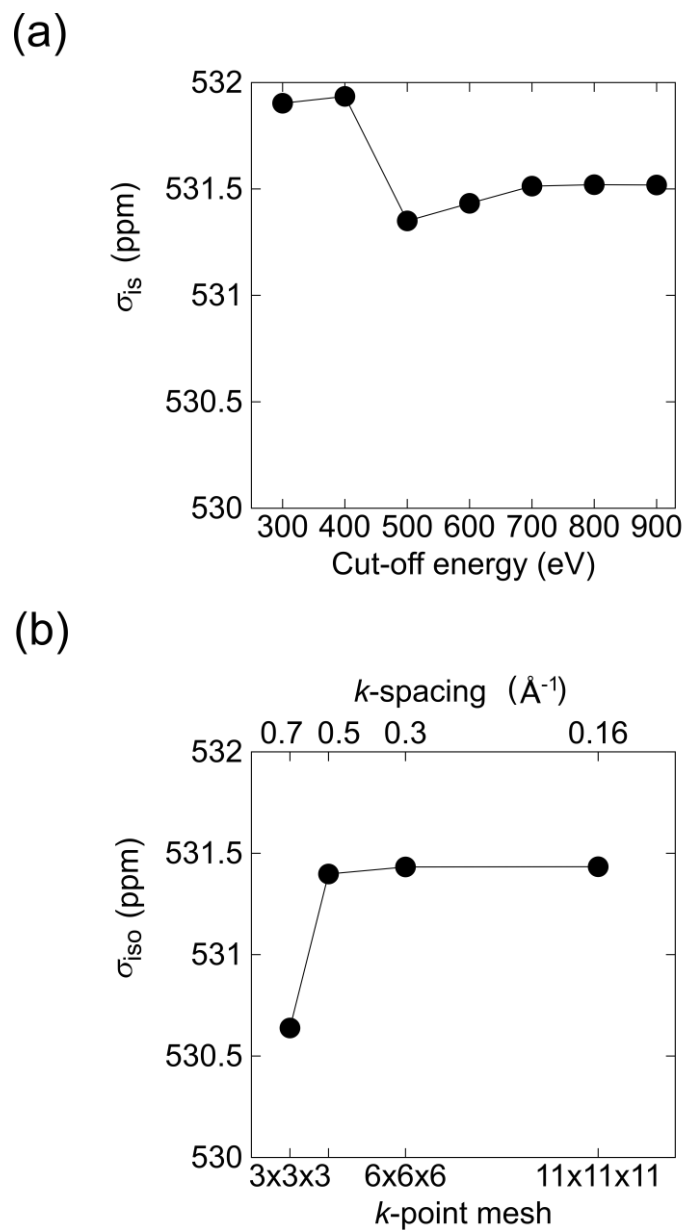


**Figure 2.A1.** Calculated chemical shift of Al for  $\alpha$ -Al<sub>2</sub>O<sub>3</sub> as a function of (a) cut-off energy and (b)  $k$ -point mesh.

## Appendix 2.B Defect Cluster Model

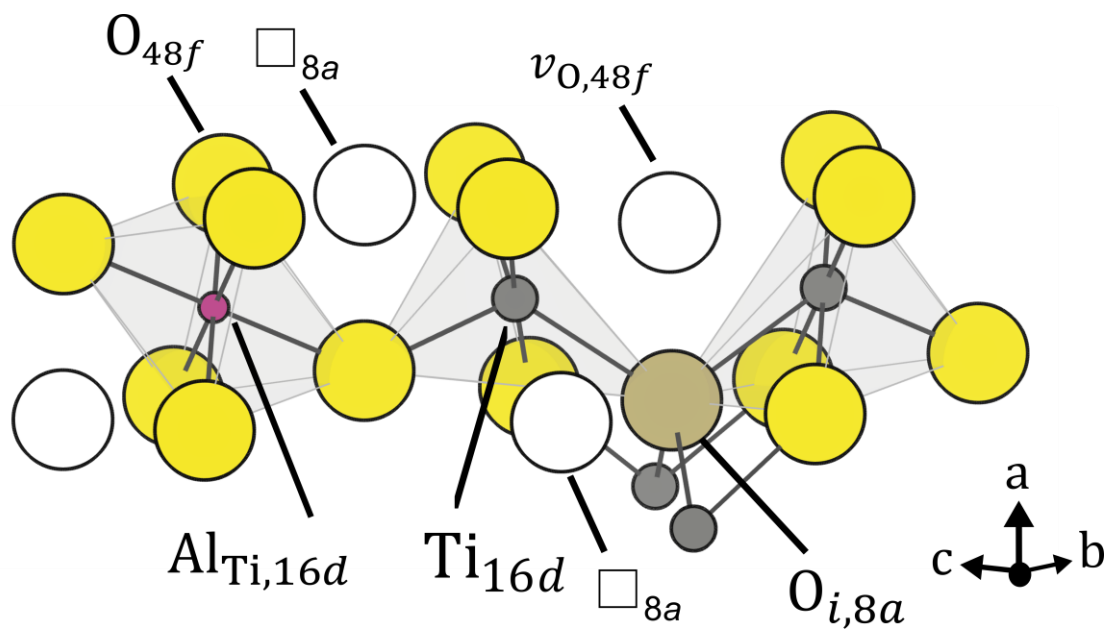


**Figure 2.A2.** Local environment of  $\text{Al}'_{\text{Ti}} + \{v_{\text{O},48f} \cdot \text{O}''_{i,2\text{NN}} \cdot v_{\text{O},48f}\}''$  in  $\text{Y}_2\text{Ti}_2\text{O}_7:\text{Al}$ .

## Bibliography

- [1] Kocevski, V.; Pilania, G.; Uberuaga, B. P. Modeling Disorder in Pyrochlores and Other Anion-Deficient Fluorite Structural Derivative Oxides. *Front. Chem.* **2021**, *9*, 712543.
- [2] Wen, L. C.; Hsieh, H. Y.; Lee, Y. H.; Chang, S. C.; Kao, H. C. I.; Sheu, H. S.; Lin, I. N.; Chang, J. C.; Lee, M. C.; Lee, Y. S. Preparation of Compact Li-Doped  $Y_2Ti_2O_7$  Solid Electrolyte. *Solid State Ionics* **2012**, *206*, 39–44.
- [3] Wuensch, B. J.; Eberman, K. W.; Heremans, C.; Ku, E. M.; Onnerud, P.; Yeo, E. M. E.; Haile, S. M.; Stalick, J. K.; Jorgensen, J. D. Connection between Oxygen-Ion Conductivity of Pyrochlore Fuel-Cell Materials and Structural Change with Composition and Temperature. *Solid State Ionics* **2000**, *129*, 111–133.
- [4] Kramer, S. A.; Tuller, H. L. A Novel Titanate-Based Oxygen Ion Conductor:  $Gd_2Ti_2O_7$ . *Solid State Ionics* **1995**, *82*, 15–23.
- [5] Yamamura, H.; Nishino, H.; Kakinuma, K.; Nomura, K. Electrical Conductivity Anomaly around Fluorite–Pyrochlore Phase Boundary. **2003**, *158*, 359–365.
- [6] Kramer, S.; Spears, M.; Tuller, H. L. Conduction in Titanate Pyrochlores: Role of Dopants. *Solid State Ionics* **1994**, *72* (PART 2), 59–66.
- [7] Shin, S.; Wang, Q.; Luo, J.; Chen, R. Advanced Materials for High-Temperature Thermal Transport. *Adv. Funct. Mater.* **2020**, *30*, 1904815.
- [8] Lehmann, H.; Pitzer, D.; Pracht, G.; Vassen, R.; Stöver, D. Thermal Conductivity and Thermal Expansion Coefficients of the Lanthanum Rare-Earth-Element Zirconate System. *J. Am. Ceram. Soc.* **2003**, *86*, 1338–1344.
- [9] Fornasiero, P.; Di Monte, R.; Rao, G. R.; Kaspar, J.; Meriani, S.; Trovarelli, A.; Graziani, M. Rh-Loaded  $CeO_2$ - $ZrO_2$  Solid-Solutions as Highly Efficient Oxygen Exchangers: Dependence of the Reduction Behavior and the Oxygen Storage Capacity on the Structural-Properties. *Journal of Catalysis*. 1995, 168–177.
- [10] Li, F.; Zhou, L.; Liu, J. X.; Liang, Y.; Zhang, G. J. High-Entropy Pyrochlores with Low Thermal Conductivity for Thermal Barrier Coating Materials. *J. Adv. Ceram.* **2019**, *8*, 576–582.

- [11] Jiang, B.; Bridges, C. A.; Unocic, R. R.; Pitike, K. C.; Cooper, V. R.; Zhang, Y.; Lin, D. Y.; Page, K. Probing the Local Site Disorder and Distortion in Pyrochlore High-Entropy Oxides. *J. Am. Chem. Soc.* **2021**, *143*, 4193–4204.
- [12] Uematsu, K.; Shinozaki, K.; Sakurai, O.; Mizutani, N.; Kato, M. Electrical Conductivity of the System  $Y_2O_3$ - $TiO_2$ . *J. Am. Ceram. Soc.* **1979**, *62*, 219–221.
- [13] Moon, P. K.; Tuller, H. L. Ionic Conduction in the  $Gd_2Ti_2O_7$ - $Gd_2Zr_2O_7$  System. *Solid State Ionics* **1988**, *28–30* (PART 1), 470–474.
- [14] Gill, J. K.; Pandey, O. P.; Singh, K. Role of Sintering Temperature on Thermal, Electrical and Structural Properties of  $Y_2Ti_2O_7$  Pyrochlores. *Int. J. Hydrogen Energy* **2011**, *36*, 14943–14947.
- [15] Shlyakhtina, A. V. Morphotropy, Isomorphism, and Polymorphism of Ln<sub>2</sub>M<sub>2</sub>O<sub>7</sub>-Based (Ln = La-Lu, Y, Sc; M = Ti, Zr, Hf, Sn) Oxides. *Crystallogr. Reports* **2013**, *58*, 548–562.
- [16] Shlyakhtina, A. V.; Shcherbakova, L. G. Polymorphism and High-Temperature Conductivity of Ln<sub>2</sub>M<sub>2</sub>O<sub>7</sub> (Ln = Sm-Lu; M = Ti, Zr, Hf) Pyrochlores. *Solid State Ionics* **2011**, *192*, 200–204.
- [17] Hao, C. K.; Hung, H. E.; Lee, C. S. Characterization and Electrochemical Properties of Chromium-Substituted Pyrochlore  $Y_2Ti_{2-x}Cr_xO_{7-δ}$ . *J. Sol-Gel Sci. Technol.* **2015**, *76*, 428–435.
- [18] Kim, N.; Grey, C. P. Solid-State NMR Study of the Anionic Conductor Ca-Doped  $Y_2Ti_2O_7$ . *Dalt. Trans.* **2004**, *34*, 3048–3052.
- [19] Ohtsuka, M.; Oda, K.; Tanaka, M.; Kitaoka, S.; Muto, S. 2D-HARECXs Analysis of Dopant and Oxygen Vacancy Sites in Al-Doped Yttrium Titanate. *J. Am. Ceram. Soc.* **2021**, *104*, 3760–3769.
- [20] Tanaka, M.; Kitaoka, S.; Yoshida, M.; Sakurada, O.; Hasegawa, M.; Nishioka, K.; Kagawa, Y. Structural Stabilization of EBC with Thermal Energy Reflection at High Temperatures. *J. Eur. Ceram. Soc.* **2017**, *37*, 4155–4161.
- [21] Bonhomme, C.; Gervais, C.; Babonneau, F.; Coelho, C.; Pourpoint, F.; Azaïs, T.; Ashbrook, S. E.; Griffin, J. M.; Yates, J. R.; Mauri, F.; Pickard, C. J. First-Principles Calculation of NMR Parameters Using the Gauge Including Projector Augmented Wave Method: A Chemists Point of View. *Chem. Rev.* **2012**, *112*, 5733–5779.
- [22] Choi, M.; Matsunaga, K.; Oba, F.; Tanaka, I. Al NMR Chemical Shifts in Oxide Crystals: A First-Principles Study. *J. Phys. Chem. C* **2009**, *113*, 3869–3873.

- [23] Smith, M. E. Application of  $^{27}\text{Al}$  NMR Techniques to Structure Determination in Solids. *Appl. Magn. Reson.* **1993**, *4*, 1–64.
- [24] Reif, B.; Ashbrook, S. E.; Emsley, L.; Hong, M. Solid-State NMR Spectroscopy. *Nat. Rev. Methods Prim.* **2021**, *1*, 2.
- [25] Pickard, C. J.; Mauri, F. All-Electron Magnetic Response with Pseudopotentials: NMR Chemical Shifts. *Phys. Rev. B* **2001**, *63*, 2451011–2451013.
- [26] Petrilli, H. M.; Blöchl, P. E. Electric-Field-Gradient Calculations Using the Projector Augmented Wave Method. *Phys. Rev. B* **1998**, *57*, 14690–14697.
- [27] van Meerten, S. G. J.; Franssen, W. M. J.; Kentgens, A. P. M. SsNake: A Cross-Platform Open-Source NMR Data Processing and Fitting Application. *J. Magn. Reson.* **2019**, *301*, 56–66.
- [28] Blöchl, P. E. Projector Augmented-Wave Method. *Phys. Rev. B* **1994**, *50*, 17953–17979.
- [29] Kresse, G.; Furthmüller, J. Efficient Iterative Schemes for Ab Initio Total-Energy Calculations Using a Plane-Wave Basis Set. *Phys. Rev. B* **1996**, *54*, 11169–11186.
- [30] Kresse, G.; Hafner, J. Ab Initio Molecular Dynamics for Liquid Metals. *Phys. Rev. B* **1993**, *47*, 558–561.
- [31] Perdew, J. P.; Burke, K.; Ernzerhof, M. Generalized Gradient Approximation Made Simple. *Phys. Rev. Lett.* **1997**, *77*, 3865–3868.
- [32] Details are described in Chapter 3.
- [33] Dudarev, S.; Botton, G. Electron-Energy-Loss Spectra and the Structural Stability of Nickel Oxide: An LSDA+U Study. *Phys. Rev. B* **1998**, *57*, 1505–1509.
- [34] Pyykkö, P. Year-2008 Nuclear Quadrupole Moments. *Mol. Phys.* **2008**, *106*, 1965–1974.
- [35] Heyd, J.; Scuseria, G. E.; Ernzerhof, M. Hybrid Functionals Based on a Screened Coulomb Potential. *J. Chem. Phys.* **2003**, *118*, 8207–8215.
- [36] Parlinski, K.; Li, Z. Q.; Kawazoe, Y. First-Principles Determination of the Soft Mode in Cubic  $\text{ZrO}_2$ . *Phys. Rev. Lett.* **1997**, *78*, 4063–4066.
- [37] Togo, A.; Oba, F.; Tanaka, I. First-Principles Calculations of the Ferroelastic Transition between Rutile-Type and  $\text{CaCl}_2$ -Type  $\text{SiO}_2$  at High Pressures. *Scr. Mater.* **2008**, *108*, 134106.

- [38] Togo, A.; Tanaka, I. First Principles Phonon Calculations in Materials Science. *Scr. Mater.* **2015**, *108*, 1–5.
- [39] Vlasova, M.; Kakazey, M.; Márquez Aguilar, P. A.; Stetsenko, V.; Bykov, A.; Lakiza, S. Structural and Phase Evolution in Laser Treatment of Al<sub>2</sub>O<sub>3</sub>-TiO<sub>2</sub>-Y<sub>2</sub>O<sub>3</sub> Powder Mixtures. *J. Alloys Compd.* **2014**, *586* (SUPPL. 1), S199–S204.
- [40] Freude, D.; Haase, J. *Quadrupole Effects in Solid-State Nuclear Magnetic Resonance*; 1993; Vol. 29.
- [41] Tanaka, M.; Matsudaira, T.; Kawai, E.; Kawashima, N.; Matsumoto, U.; Ogawa, T.; Takeuchi, M.; Kitaoka, S. Effect of Chemical Composition on Mass Transfer in Y<sub>2</sub>Ti<sub>2</sub>O<sub>7</sub> under Oxygen Potential Gradient at High Temperatures. *J. Ceram. Soc. Japan* **2021**, *129*, 22–31.
- [42] Marlton, F. P.; Zhang, Z.; Zhang, Y.; Proffen, T. E.; Ling, C. D.; Kennedy, B. J. Lattice Disorder and Oxygen Migration Pathways in Pyrochlore and Defect-Fluorite Oxides. *Chem. Mater.* **2021**, *33*, 1407–1415.
- [43] Panero, W. R.; Stixrude, L.; Ewing, R. C. First-Principles Calculation of Defect-Formation Energies in the Y<sub>2</sub>(Ti,Sn,Zr)<sub>2</sub>O<sub>7</sub> Pyrochlore. *Phys. Rev. B* **2004**, *70*, 054110.
- [44] Asai, K.; Tanaka, M.; Ogawa, T.; Matsumoto, U.; Kawashima, N.; Kitaoka, S.; Izumi, F.; Yoshida, M.; Sakurada, O. Crystal Structural, Thermal, and Mechanical Properties of Yb<sub>2+x</sub>Ti<sub>2-x</sub>O<sub>7-x/2</sub> Solid Solutions. *J. Solid State Chem.* **2020**, *287*, 121328.
- [45] Uno, W.; Fujii, K.; Niwa, E.; Torii, S.; Miao, P.; Kamiyama, T.; Yashima, M. Experimental Visualization of Oxide-Ion Diffusion Paths in Pyrochlore-Type Yb<sub>2</sub>Ti<sub>2</sub>O<sub>7</sub>. *J. Ceram. Soc. Japan* **2018**, *126*, 341–345.
- [46] Florian, P.; Gervais, M.; Douy, A.; Massiot, D.; Coutures, J.-P. A Multi-Nuclear Multiple-Field Nuclear Magnetic Resonance Study of the Y<sub>2</sub>O<sub>3</sub>-Al<sub>2</sub>O<sub>3</sub> Phase Diagram. *J. Phys. Chem. B* **2013**, *105*, 379–391.
- [47] Glensk, A.; Grabowski, B.; Hickel, T.; Neugebauer, J. Breakdown of the Arrhenius Law in Describing Vacancy Formation Energies: The Importance of Local Anharmonicity Revealed by Ab Initio Thermodynamics. *Phys. Rev. X* **2014**, *4*, 011018.

- [48] Zhang, X.; Grabowski, B.; Hickel, T.; Neugebauer, J. Calculating Free Energies of Point Defects from Ab Initio. *Comput. Mater. Sci.* **2018**, *148*, 249–259.
- [49] Sutton, C.; Levchenko, S. V. First-Principles Atomistic Thermodynamics and Configurational Entropy. *Front. Chem.* **2020**, *8*, 757.
- [50] Shannon, R. D. Revised Effective Ionic Radii and Systematic Studies of Interatomic Distances in Halides and Chalcogenides. *Acta Crystallogr. Sect. A Found. Adv.* **1976**, *32*, 751–767.
- [51] Taftø, J.; Spence, J. C. H. Crystal Site Location of Iron and Trace Elements in a Magnesium-Iron Olivine by a New Crystallographic Technique. *Science.* **1982**, *218*, 49–51.
- [52] Shitara, K.; Moriasa, T.; Sumitani, A.; Seko, A.; Hayashi, H.; Koyama, Y.; Huang, R.; Han, D.; Moriwake, H.; Tanaka, I. First-Principles Selection of Solute Elements for Er-Stabilized Bi<sub>2</sub>O<sub>3</sub> Oxide-Ion Conductor with Improved Long-Term Stability at Moderate Temperatures. *Chem. Mater.* **2017**, *29*, 3763–3768.
- [53] Bjørheim, T. S.; Kotomin, E. Ab Initio Thermodynamics of Oxygen Vacancies and Zinc Interstitials in ZnO. *J. Phys. Chem. Lett.* **2014**, *5*, 4238–4242.
- [54] Grabowski, B.; Ismer, L.; Hickel, T.; Neugebauer, J. Ab Initio up to the Melting Point: Anharmonicity and Vacancies in Aluminum. *Phys. Rev. B* **2009**, *79*, 134106.

## Chapter 3

### Cooperative Oxide-Ion Transport in Pyrochlore $\text{Y}_2\text{Ti}_2\text{O}_7$ : A

### First-principles Molecular Dynamics Study

#### 3.1 Introduction

Fast ion conductors make possible a range of technologically important devices such as lithium-ion batteries, solid-oxide fuel cells, catalytic convertors, and gas sensors.<sup>1-5</sup> Exploration and optimization of materials for these devices has led to rapid progress in terms of improved efficiency and durability over the past few decades. In many cases, however, ion conductivities remain insufficient for optimal performance, particularly at lower temperatures, and intensive efforts continue to be directed to the search for new materials, e.g., the  $\text{Ba}_7\text{Nb}_4\text{MoO}_{20}$  system recently discovered by Yashima et al.<sup>1</sup> Whether using experimental or computational methods, a fundamental understanding of the atomic-scale diffusion mechanisms is needed because this provides the basis for the rational design and optimization of new ionic conductors.

Models of atomic-scale ionic diffusion are commonly based on one or more of four migration mechanisms, namely, vacancy hopping, ring, interstitial, or interstitialcy. In these models, mobile ions move one by one in a sequential manner. Recently, other mechanisms have been uncovered in a variety of novel fast ion conductors.<sup>3-8</sup> For example, using atomic-scale simulations, He et al.<sup>4</sup> showed that energy barriers for lithium-ion diffusion in  $\text{Li}_7\text{La}_3\text{Zr}_2\text{O}_{12}$  (LLZO),  $\text{Li}_{1.3}\text{Al}_{0.3}\text{Ti}_{1.7}(\text{PO}_4)_3$  (LATP), and  $\text{Li}_{10}\text{GeP}_2\text{S}_{12}$  (LGPS) systems are lowered markedly when mobile ions move cooperatively. Similarly, Masson et al.<sup>9</sup> reported a combined experimental and theoretical study showing that the oxygen ions in apatite  $\text{La}_{9.33+x}(\text{SiO}_4)_6\text{O}_{2+3x/2}$  diffuse by a double hopping mechanism, and Noda et al.<sup>3</sup>

reported that two lithium ions interact with each other during lithium-ion diffusion in NASICON-structured  $\text{LiZr}_2(\text{PO}_4)_3$ . These findings demonstrate that more complex ion-migration mechanisms often operate in complex inorganic materials.

Remarkable increases in computational performance over the past two decades have led to first-principles molecular dynamics (FPMD) simulations becoming a standard tool for investigating ionic diffusion at the atomic level.<sup>3,6,10-13</sup> FPMD allows complex motions of atoms such as anharmonic vibrations and long-scale diffusion to be modeled at the level of density functional theory (DFT). Nevertheless, the identification of a particular diffusion mechanism using FPMD remains difficult because of the need to deconvolute data in which diffusing ions simultaneously follow individual trajectories with varying degrees of interaction with other diffusing ions and the surrounding framework. Although time-series analyses such as wavelet transformation analysis,<sup>14-16</sup> short-time Fourier transformation analysis,<sup>17</sup> and Hilbert-Huang transformation (HHT) analysis<sup>18</sup> have been employed to characterize complex and correlated mechanisms, so far their utilization has been limited to simple systems. For this reason, in many studies, diffusion mechanisms have only been adduced based on a simple density map constructed by integrating atom trajectories, which can ignore or obscure critical details about complex migration mechanisms (see Figure 3.1a), thereby resulting in an erroneous or misleading interpretation. Such difficulties mean that a systematic and universal methodology for analyzing trajectories of ions is needed to determine diffusion mechanisms in complex compounds reliably.

Pyrochlore  $\text{Y}_2\text{Ti}_2\text{O}_7$  is a mixed oxide-ion conductor that exhibits oxide-ion diffusion and *p*-type electronic conductivity and is being considered for a range of applications from high-temperature electrodes to environmental barrier coatings.<sup>19</sup> The stability of point defects and diffusion mechanisms in oxide pyrochlores have been studied over several decades. For example, by performing molecular dynamics (MD) simulations of 54  $A_2B_2O_7$  ( $A = \text{Lu}, \text{Yb}, \text{Er}, \text{Y}, \text{Gd}, \text{Eu}, \text{Sm}, \text{Nd}$ ,

Pr, and La;  $B = \text{Ti, Ru, Mo, Sn, Zr, and Pb}$ ) compounds using an empirical force field, Pirzada et al.<sup>20</sup> found that a single oxide-ion vacancy was energetically more favorable than a split oxide-ion vacancy, and a straightforward stepwise mechanism between single oxide-ion vacancies was favored in the case of the titanates. Li et al.<sup>21</sup> observed a similar trend using first-principles calculations. Experimentally, bond valence sum analyses of neutron and X-ray diffraction spectra has suggested that oxide-ion diffusion occurs along  $[100]$  and  $[110]$  directions of the pyrochlore crystal,<sup>22,23</sup> where the latter was taken as evidence of the presence of split vacancies. Because of this discrepancy between results of theoretical calculations and experimental observations, the actual diffusion mechanism operating in oxide pyrochlores remains uncertain.

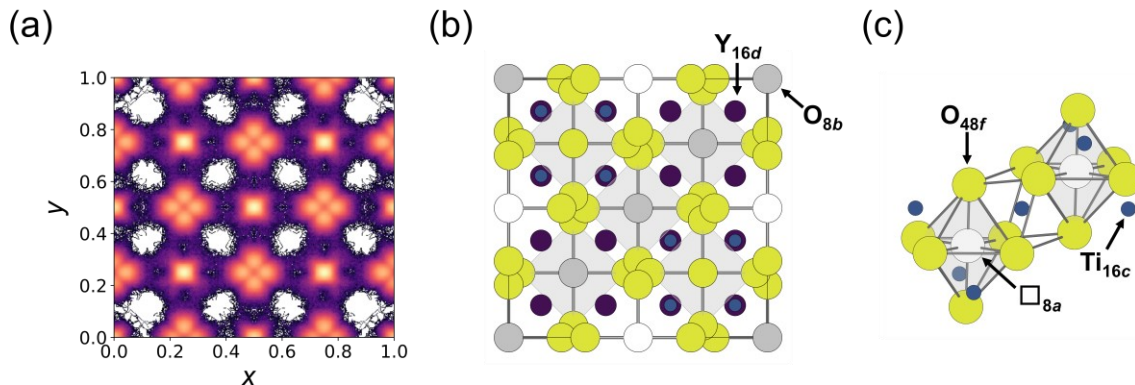


**Figure 3.1.** (a) Density map of oxide ions, (b) crystal structure with an 88-atom conventional cubic cell, and (c) two structural units of pyrochlore  $\text{Y}_2\text{Ti}_2\text{O}_7$ . In (a),  $x$  and  $y$  coordinates are normalized to cell lengths. In (b) and (c), indigo, blue, light yellow green, and gray spheres denote  $\text{Y}_{16d}$ ,  $\text{Ti}_{16c}$ ,  $\text{O}_{48f}$ , and  $\text{O}_{8b}$  atoms, respectively, and white spheres denote vacant  $8a$  sites labeled  $\square_{8a}$ .

In this study, we investigate the diffusion mechanism of oxide ions in pyrochlore  $\text{Y}_2\text{Ti}_2\text{O}_7$  at the atomic level using FPMD simulations. First we extract the cooperative mechanism of the oxide-ion migration using a time-series mapping approach, where the mobile ions are assigned to ideal lattice sites of the ground-state crystal by performing Voronoi–Dirichlet partition<sup>24</sup> (VDP). To estimate the energy barriers of the diffusion pathways identified in this manner, first-principles

calculations at 0 K using the climbing-image nudged elastic band (ci-NEB) method<sup>25,26</sup> are performed. Lastly, we examine the dependence of the stability of defect structures on temperature by combining the FPMD results with results of lattice vibration calculations.

## 3.2 Computational Methods

All first-principles calculations were performed using the projector augmented wave (PAW) method<sup>27</sup> within the framework of DFT as implemented in the Vienna Ab initio Simulation Package<sup>28,29</sup> (VASP). The generalized gradient approximation (GGA) functional with Perdew–Burke–Ernzerhof parameterization adapted for solids<sup>30</sup> (PBEsol) was used to treat exchange–correlation interactions. We used an 88-atom cubic fluorite cell. The dependence of the diffusion mechanism and energetics was carefully examined before choosing the 88-atom cell, which is explained in Table 3.1 in Appendix 3.A. Brillouin zone (BZ) integration was performed using a  $2 \times 2 \times 2$  Monkhorst–Pack  $k$ -point mesh<sup>31</sup> and a Gaussian smearing approach with a smearing width of 0.01 eV. The  $2s$  and  $2p$  orbitals for O atoms,  $3d$  and  $4s$  orbitals for Ti atoms, and  $4s$ ,  $4p$ ,  $4d$  and  $5s$  orbitals for Y atoms were treated as valence states. We used a soft pseudopotential for O atoms. An on-site Coulomb correction with effective Hubbard parameter  $U_{\text{eff}} = 5.4$  eV was applied to Ti 3d electrons. This value is calculated based on the linear response method developed by Cococcioni et al.<sup>32</sup> The calculated band gap was found to be in good agreement with experimental values<sup>33-36</sup> (Table 3.1 and Figure 3.A1 in Appendix 3.A).

For FPMD simulations, the velocity–Verlet algorithm was used to integrate the equations of motion with a time step of 1.5 fs. A total of 27 000 time steps (40.5 ps) were calculated in the  $NPT$  ensemble with a Langevin thermostat<sup>37,38</sup> at temperatures of 800 K, 1000 K, and 1200 K. The cutoff energy for planewave basis sets was increased to 400 eV only for calculations in the  $NPT$  ensemble. Equilibrium cell volumes were taken as the average over at least 10 000 time steps after confirming

that they had reached convergence. The equilibrium lattice parameters were confirmed to increase linearly as a function of temperature. In the subsequent  $NVT$  ensemble simulations, FPMD simulations were carried out with a Nosé–Hoover thermostat<sup>39,40</sup> for a total of 150,000 time steps (225 ps). In these simulations, an oxide-ion vacancy was introduced by removing a single oxygen atom and two electrons from the simulation cell with charge compensation by addition of a homogeneous jellium background charge.  $NVT$  simulations were performed at 300 K, 600 K, 900 K, 1200 K, and 1500 K. The cutoff energy for planewave basis sets was 300 eV.

**Table 3.1.** Calculated and experimental values of the band gap of pyrochlore  $Y_2Ti_2O_7$ .

method	exchange–correlation functional or spectroscopy technique	$\Delta E_{bg}$ (eV)	reference
DFT	GGA-PBEsol+U ( $U_{eff} = 5.4$ eV)	3.66	this work
DFT	GGA-PBEsol	2.86	this work
DFT	hybrid-HSE06	4.35	this work
expt.	UV-vis transmittance spectroscopy	3.7	33
expt.	UV-vis-NIR transmittance spectroscopy	3.44	34
expt.	UV-vis reflectance spectroscopy	3.7	35
DFT	GGA-PBE	2.84	36

To calculate migration energy barriers, the ci-NEB method was used at 0 K. The cutoff energy in this case was 550 eV. Atom positions were fully optimized until residual forces were less than 0.01 eV/Å, with the lattice constant fixed at that of the ideal pyrochlore structure. The spring constant between neighboring images was 5.0 eV/Å<sup>2</sup>.

To determine the vibrational contribution to free energies, phonon calculations were performed in the harmonic approximation with the phonopy code<sup>41,42</sup>. The cutoff energy was 550 eV. The convergence criterion was set to 0.002 eV/Å, and BZ integration was performed using a 3×3×3

gamma centered  $k$ -point mesh in this case. The interatomic force constants were calculated using the Parlinski–Li–Kawazoe method.<sup>43</sup>

### 3.3 Results and Discussion

The ideal pyrochlore structure (space group  $Fd\bar{3}m$ ) is illustrated in Figure 3.1b. In this structure, atoms are located at the following Wyckoff positions: Y at  $16c$ , Ti at  $16d$ , O at  $48f$ , O' at  $8b$ , and intrinsic vacancies at  $8a$ .  $48f$ ,  $8b$ , and  $8a$  sites have different chemical environments because  $48f$ ,  $8b$ , and  $8a$  sites are surrounded by two  $16c$  and two  $16d$ , four  $16c$ , and four  $16d$  sites, respectively. Since the time-series variation in the anion-site occupancies only indicates atom hopping events, identification of the defect states resulting from such an event is necessary to elucidate the microscopic migration mechanism. Defect types were identified by performing  $NVT$ -ensemble FPMD simulations of the cubic pyrochlore unit cell after determining the equilibrium lattice constant and linear thermal expansion coefficient at a given temperature from  $NPT$ -ensemble FPMD simulations. The lattice parameters and linear thermal expansion coefficient are listed in Table 3.2. The defects can be classified into three types: (1) neighboring Frenkel pairs ( $O_i'' + v_{O,48f}''$ ), (2) an oxide-ion vacancy on the  $48f$  site ( $v_{O,48f}''$ ), and (3) a combined Frenkel pair and vacancy ( $v_{O,48f}'' + O_i'' + v_{O,48f}''$ ). The Frenkel-pair defect in the case 1 corresponds to a vacancy on a  $48f$  site and an oxide-ion on a neighboring  $8a$  site. The complex defect in case 3 is called a split vacancy, and consists of oxide-ion

**Table 3.2.** Lattice constant,  $a$ , and linear thermal expansion coefficient,  $\alpha$ , for pyrochlore  $Y_2Ti_2O_7$ .

method	$a$ (Å)	$\alpha$ (1/K)	reference
DFT	10.12	$11 \times 10^{-6}$	this work
expt.	10.06	$8.36 \times 10^{-6}$	46

vacancies on two  $48f$  sites and an oxide ion on a shared neighboring  $8a$  site. These defect types are the same as those previously reported in the literature.<sup>20</sup> The computational algorithms of the mapping approach are described in Appendix 3.C.

To calculate time-series variations of the defect states, we focus on structural units consisting of octahedral clusters of oxide ions centered on an  $8a$  site with its six neighboring  $48f$  sites forming the apices of the octahedron. These units are separated by Ti-centered  $\text{TiO}_6$  octahedra, as illustrated in Figure 3.1c. Using these structural units as reference, defect states observed during the MD simulations could be classified into one of the above three types or as there being no defect. Because long-scale diffusion involves oxide-ion migration between  $8a$ -centered clusters, the diffusion mechanism can be identified by analyzing the time-series variation of defect states of each  $8a$ -centered cluster.

Figure 3.2a shows an example of the time-series of defect states at 1500 K. The complete time-series results are shown in Figure 3.A2 in Appendix 3.B. Switching between split vacancy and single vacancy can be seen to occur frequently. This suggests that the migration energy barrier between these two states is low. However, intra-cluster switching does not contribute to long-scale diffusion directly, whereas switches in defect states from single/split vacancy to no defect/Frenkel pair and *vice versa* contribute to long-scale diffusion, because in these cases at least one oxide ion migrates to a neighboring cluster. This latter type of transition is observed four times over the time span in Figure 3.2a. A magnified views of the time-series diagram around the first inter-cluster migration around 21 ps and around 39 ps are shown in Figure 3.2b and c, respectively. The single vacancy in cluster #3 changes to a no defect while the no defect in cluster #5 simultaneously changes to a split vacancy. For the second jump, at 39 ps, the reverse process occurs; the split vacancy in cluster #5 returns to a no defect while cluster #2 reverts to a single vacancy.

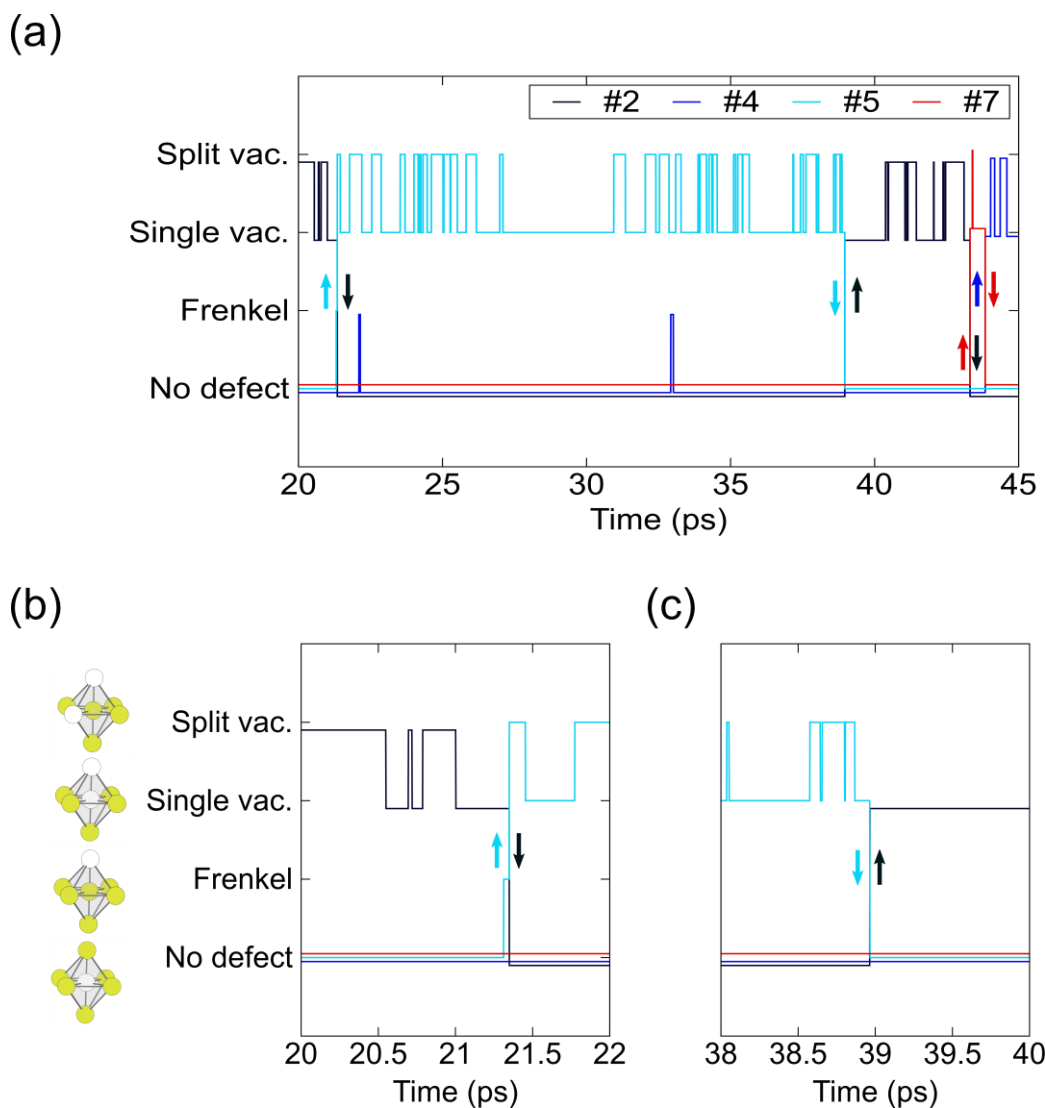


**Figure 3.2.** (a) Time-series diagram of oxide-ion defect states at 1500 K in an *NVT* ensemble between 20 ps and 45 ps; (b) and (c) magnified view of (a) between 20 ps and 22 ps, and between 38 ps and 40 ps, respectively. The different colored lines indicate different  $8a$ -centered octahedral clusters (#2, #4, #5, and #7). Arrows indicate transitions between defect states corresponding to inter-cluster migration.

These instances demonstrate that time-series plots of the oxide-ion clusters, despite being a comparatively simple diagnostic method, reveal cooperative behaviors during oxide-ion diffusion in pyrochlore  $Y_2Ti_2O_7$ . There are time lags of approximately 0.1 ps when the split vacancy reverts to a

no-defect state and *vice versa*. These time lags correspond to frequency of 10 THz that falls within the range of phonon frequencies of oxide ions in pyrochlore  $\text{Yb}_2\text{Ti}_2\text{O}_7$ <sup>44</sup>, which is 5 THz to 25 THz. The time lags can thus be attributed to the difference in relative positions of two oxide ions, before moving to their new positions.

To examine the energy barriers of the migration paths identified in this manner, we performed *ci*-NEB calculations. Figure 3.3 compares the two-step cooperative and three-step stepwise mechanisms in terms of schematic diagrams and energy profiles. The former mechanism corresponds to the pathway identified from analysis of the FPMD time-series data, whereas the latter is the conventional diffusion mechanism assumed in the literature<sup>20,21</sup>. In both cases, the initial and final states correspond to the split-vacancy state as this is lower in energy than the single vacancy by 0.16 eV. The energy plots in Figure 3.3 reveal that the migration barrier of the cooperative mechanism (0.65 eV) is much lower than that of the stepwise mechanism (0.96 eV). This is consistent with the mechanism observed in FPMD simulations being predominantly of the cooperative type. We note that although analysis of mean square displacements (MSDs) of oxide ions during the FPMD runs should produce activation energies of similar magnitude to the *ci*-NEB calculations, the number of hopping events in the present simulations is too low to provide sufficient statistical accuracy; considering the heavy computational cost required to increase the length of the FPMD simulations sufficiently to remedy this, *ci*-NEB calculations is a far more practical alternative.

Figure 3.4 shows a composite image of the oxide ion motion according to the *ci*-NEB calculations of the two-step cooperative mechanism. The oxide ion on the labeled  $8a$  site in Figure 3.4a is initially bonded to three titanium atoms ( $\text{Ti}_A$ ,  $\text{Ti}_B$ , and  $\text{Ti}_D$ ), with an oxygen vacancy on a  $48f$  site in the coordination sphere of the  $\text{Ti}_A$  atom. In the first step, this oxide ion hops to the vacant site, breaking its bond with the  $\text{Ti}_B$  atom and forming two new bonds with yttrium atoms. This results in

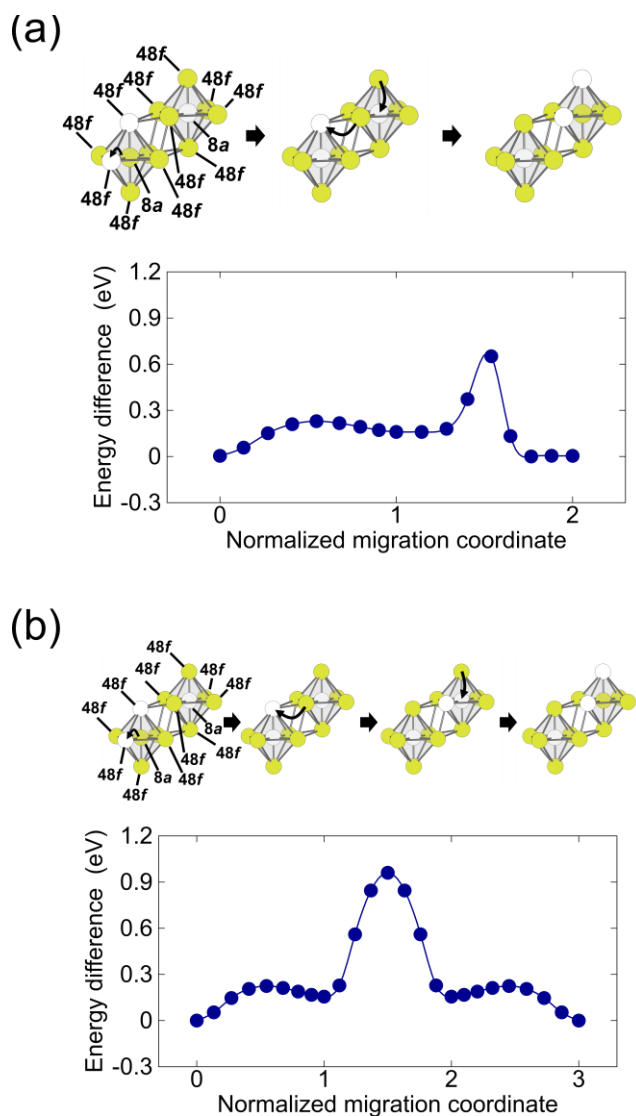


**Figure 3.3.** Schematics of  $8a$ -centered octahedral clusters and potential energy profiles for (a) a two-step cooperative mechanism, and (b) a three-step stepwise mechanism involving sequential vacancy hops. In the upper panel in (a) and (b), light yellow green and white spheres denote O atom, and a vacant site, respectively. Black arrows in a crystal indicate directions of oxide-ion migration.

the coordination number of  $Ti_B$  decreasing from six to five, similar to the  $Ti_A$  atom. In the second step, two oxide ions bonded to  $Ti_B$  and  $Ti_C$  simultaneously move to neighboring sites, the first from its  $48f$  site onto the adjacent  $48f$  site opened up by movement of the oxide ion in the first step and the second to  $8a$  site opened up by motion of this  $48f$  oxygen. At the saddle point,  $Ti_A$ -O and  $Ti_C$ -O bond

lengths become longer, momentarily reducing the coordination numbers of  $Ti_A$  and  $Ti_C$ . As the oxide ion continues its jump to the neighboring  $48f$  site, the coordination numbers of  $Ti_A$  and  $Ti_B$  both return to six and that of  $Ti_C$  is reduced to five, so that the oxide-ion vacancy has in effect migrated from the  $Ti_A$ -O octahedron to the  $Ti_C$ -O octahedron. This cooperative relaxation of two oxide ions to maintain the coordination numbers of the Ti atoms results in a lower energy barrier for oxygen to move through the structure than is the case when the oxide ions jump sequentially.

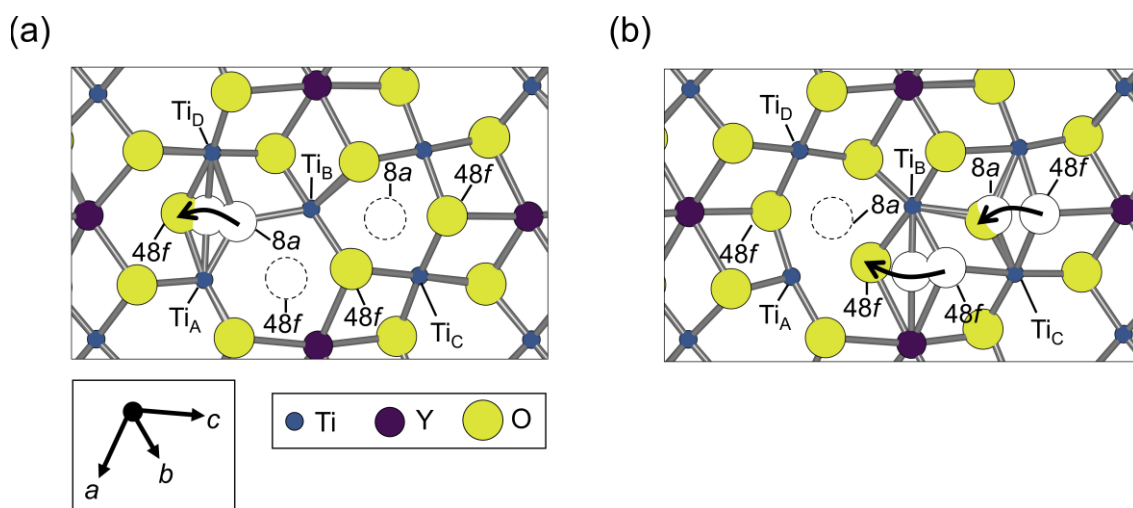


**Figure 3.4.** Composite nudged elastic band images of the two-step cooperative mechanism in pyrochlore  $Y_2Ti_2O_7$ ; (a) first step, and (b) second step. Open circles represent mobile ions in the initial positions and at saddle points along the migration trajectory for each step. Black arrows indicate directions of oxide-ion migration.

Table 3.3 compares activation energies of oxide-ion diffusion in pyrochlore  $Y_2Ti_2O_7$  calculated in this study with those previously reported from experiment and theoretical modeling. It is worth noting that the experimental values are widely scattered, with values ranging from 0.30 eV to 1.15 eV.<sup>45,46</sup> This large scatter may be a result of differences in composition, microstructure, and/or crystalline morphology. Indeed, the high activation energy of 1.15 eV reported by Joseph et al.<sup>45</sup> was for a nanocrystalline sample, in which there is a large number of grain boundaries, which on average are known to be more resistive than the crystal bulk. Gill et al.<sup>46</sup> also noted that their  $Y_2Ti_2O_7$  sample

was significantly reduced when sintered at high temperature, with a composition of  $Y_2Ti_2O_{4.16}$  after sintering at 1550 °C according to XRD analysis, and this large oxygen loss may result in a change of diffusion mechanism. The most reliable experimental activation energy for  $Y_2Ti_2O_7$ , 0.60 eV, thus appears to be that of the bulk crystal, which is comparable to the energy barrier of the cooperative mechanism obtained in the present study.

**Table 3.3.** Experimental and calculated activation energies,  $E_a$ , of oxide ions in  $Y_2Ti_2O_7$ . Calculated energies from previous reports were obtained using either density functional theory (DFT) or force-field (FF) methods.

method	synthesis conditions or mechanism	$E_a$ (eV)	reference
expt.	1550 °C for 12 h	0.30 <sup>a</sup>	46
expt.	1500 °C for 12 h	0.60	46
expt.	1000 °C for 4 h (nanocrystalline)	1.15	45
FF	stepwise	1.27	20
DFT	stepwise	0.92	21
DFT	stepwise	0.96	this work
DFT	cooperative	0.65	this work

<sup>a</sup>The authors of reference 46 wrote that the sample was significantly reduced to  $Y_2Ti_2O_{4.16}$  after sintering at 1550 °C.

During the FPMD simulations, we observed frequent switches between split and single vacancies within the  $8a$ -centered cluster (see Figure 3.A2 in Appendix 3.B), with the switching rates depending strongly on temperature. As the low-energy defect state at any given temperature serves as the reference point for the initial and final positions of a migrating oxide ion, it is important to examine any changes in defect stability as a function of temperature and the effect this has on the migration mechanism. To do this, we defined a new term, the split-vacancy duration factor,  $f$ , to be the duration of a split vacancy as a fraction of the total simulation time. The duration factor varies in the range of 0 and 1. As seen in Figure 3.5a, the calculated duration factor is approximately 1 at low temperatures, which is consistent with the high energetic stability of the split vacancy at 0 K as

mentioned above. As the temperature increases, the duration factor gradually decreases to less than 0.5, which means that the single vacancy becomes more stable than the split vacancy at higher temperatures. The rate at which the duration factor decreases slows at temperatures higher than ca. 1000 K, so that it converges to approximately 0.3 at 1500 K. This indicates that, although the split vacancy does not disappear entirely, the single vacancy becomes the majority defect from 1000 to 1500 K. The coexistence of the split vacancy and single vacancy in roughly equal proportions suggests that both the cooperative and simple stepwise mechanisms may both be active at elevated temperatures, but the cooperative mechanism should occur more frequently given its considerably lower barrier height.

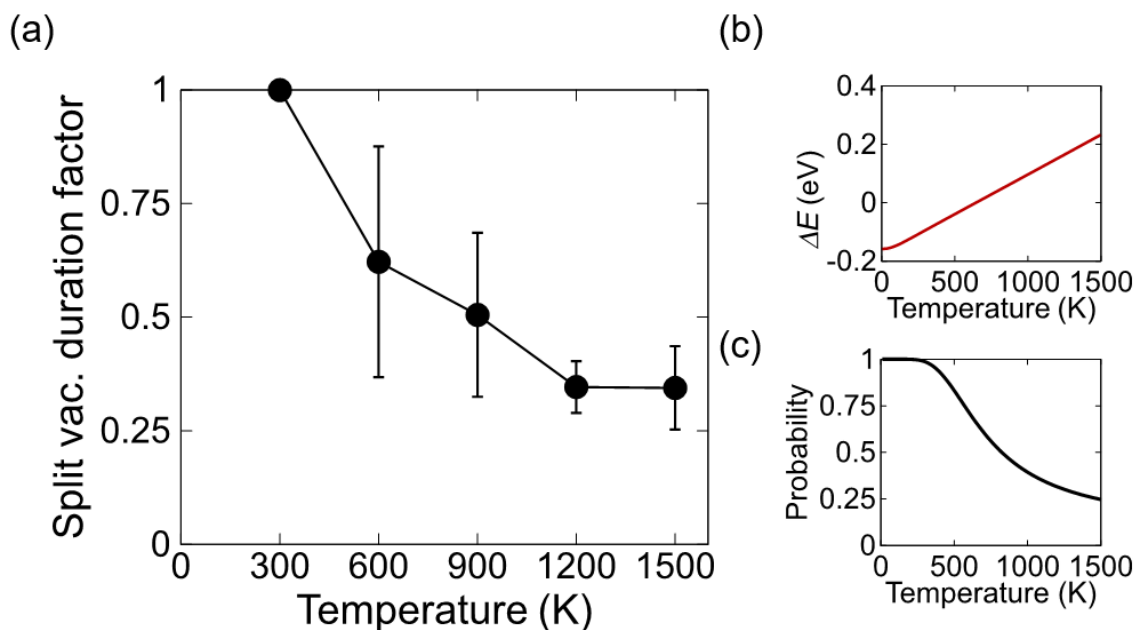


**Figure 3.5.** (a) Duration factor of split vacancies, (b) free energy of a single vacancy relative to that of a split vacancy,  $\Delta E$ , and (c) probability of formation of a split vacancy, all as functions of temperature. In (a), the black filled circles and error bars are average values and two standard deviations, respectively, calculated using five data sets each from FPMD simulations of duration 40 ps.

The error bars in Figure 3.5a are determined both by the frequency of the intra-cluster diffusion of vacancies and the probability to form split vacancy. Since we fixed the sample time to be 40 ps independent of the temperature, the number of atomic jumps is much larger at higher temperatures. This is the reason why the error is smaller at higher temperatures. At the same time, the duration factor of the split vacancy at 300 K is unity. As shown in Figure 3.A1 in Appendix 3.A, the split vacancy remains throughout almost the entire simulation. The error at 300 K is essentially zero in Figure 3.5a.

The statistical nature of the switches between split and single vacancies can be further investigated by calculating vibrational contributions to the free energy. Figure 3.5b shows the free energy of the split vacancy relative to that of the single vacancy. Although the split vacancy is lower in free energy than the single vacancy at low temperatures, the trend is reversed at temperatures higher than ca. 700 K. This behavior is consistent with the observed decrease in split-vacancy duration factor with temperature. If the two defect states are assumed to be in a canonical ensemble, the probability,  $P$ , of a split vacancy being formed is given by the following equation:

$$P(\text{Split vacancy}) = \frac{\zeta \cdot \exp\left(-\frac{\Delta E}{k_B T}\right)}{1 + \zeta \cdot \exp\left(-\frac{\Delta E}{k_B T}\right)} \quad (1)$$

where  $\zeta$  and  $\Delta E$  indicate the ratio of multiplicities and the free energy of the split vacancy relative to that of the single vacancy, respectively. The ratio of multiplicities is 2 because the split vacancy involves two lattice sites, but the single vacancy only one. As seen in Figure 3.5c, the probability gradually decreases from 1.0 to 0.3 with an increase in temperature from 0 K to 1000 K. This behavior is in good agreement with that of the duration factor estimated from FPMD trajectories (see Figure 3.5a) and confirms the validity of the two-state model used.

Nakamura et al.<sup>47</sup> calculated the energy differences for these defects for a wide range of Gd pyrochlores. According to their study, the energy difference between single vacancy and split vacancy in  $\text{Gd}_2\text{B}_2\text{O}_7$  ( $B = \text{Ti}, \text{Sn}, \text{Hf}, \text{and Zr}$ ) varies from 0.0 eV ( $B = \text{Ti}$ ), to 0.5 eV ( $B = \text{Sn}$ ), to 1.5 eV ( $B = \text{Hf}$ ), and 3.5 eV ( $B = \text{Zr}$ ). Since the energy differences of Gd titanates and stannates are small, similar to  $\text{Y}_2\text{Ti}_2\text{O}_7$  in the present study, the appearance of the cooperative mechanism may be a general feature of these pyrochlores. On the other hand, the large energy differences in zirconate and hafnate pyrochlores suggest that they behave differently from titanate and stannate pyrochlores.

The analytical methods developed in this study are applicable not only to oxide pyrochlores but also to other fast ion conductors. However, some limitations and further challenges remain. The mapping approach and way of identifying defect states needs to be modified in cases where mobile ions cannot be assigned unambiguously to well-defined lattice sites, e.g., as is the case for interstitialcy mechanisms. Analysis of ionic diffusion in amorphous materials is also not possible using these methods, so alternative techniques will need to be brought to bear in such cases.

### 3.4 Conclusions

We have developed a mapping approach based on VDP method to analyze results of FPMD simulations in crystalline inorganic compounds and applied it to investigate oxide-ion diffusion in the pyrochlore  $\text{Y}_2\text{Ti}_2\text{O}_7$ . The migration mechanism was found to consist of a two-step cooperative motion *via* a split vacancy. At low temperatures, the split vacancy is favored energetically over the single vacancy, whereas split and single vacancies coexist at higher temperatures. Our ci-NEB calculations showed that the energy barrier for the cooperative mechanism of 0.65 eV is substantially lower than that of the conventional stepwise mechanism, at 0.96 eV. The obtained energy barrier of the cooperative mechanism is comparable to the experimentally measured activation energy for oxide-

ion diffusion in the crystal bulk reported in the literature. We plan to apply our new methodology to the study of ion transport in other inorganic compounds.

### **3.5 Acknowledgement**

Reprinted with permission from Matsumoto, U; Ogawa, T; A. J. Fisher, C; Kitaoka, S; and Tanaka. I, *J. Phys. Chem. C* **2021**, 125, 20460–20467. <https://doi.org/10.1021/acs.jpcc.1c03610>. Copyright 2021 American Chemical Society.

### Appendix 3.A Band Gap of the Structure $Y_2Ti_2O_7$

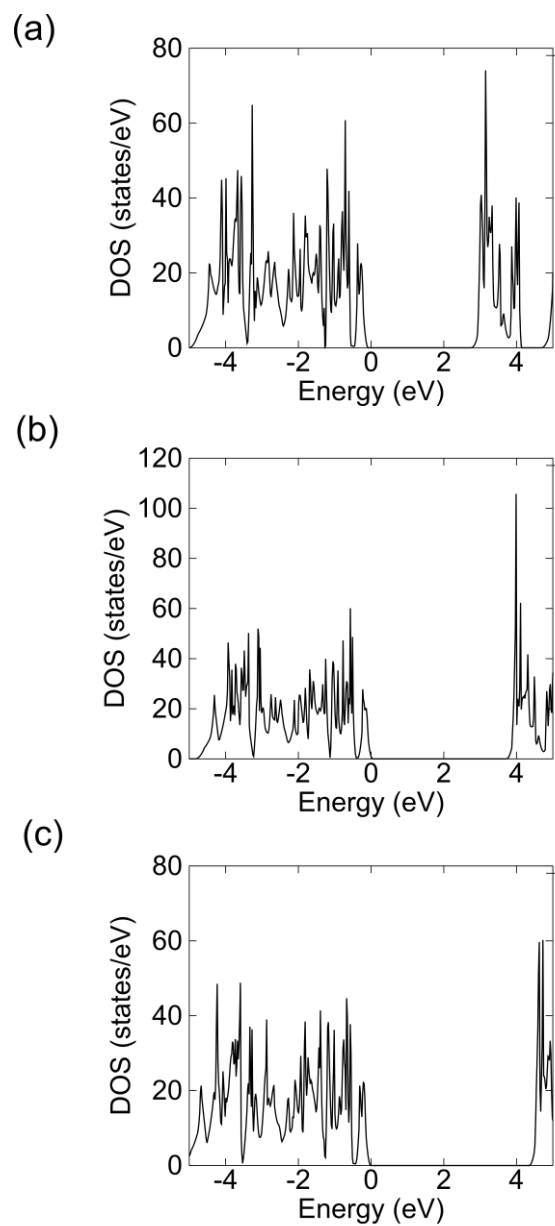


**Figure 3.A1.** Densities of states (DOS) of pyrochlore  $Y_2Ti_2O_7$  using different functional: (a) PBEsol, (b) PBEsol+U, and (c) HSE06.

## Appendix 3.B Defect State Diagrams

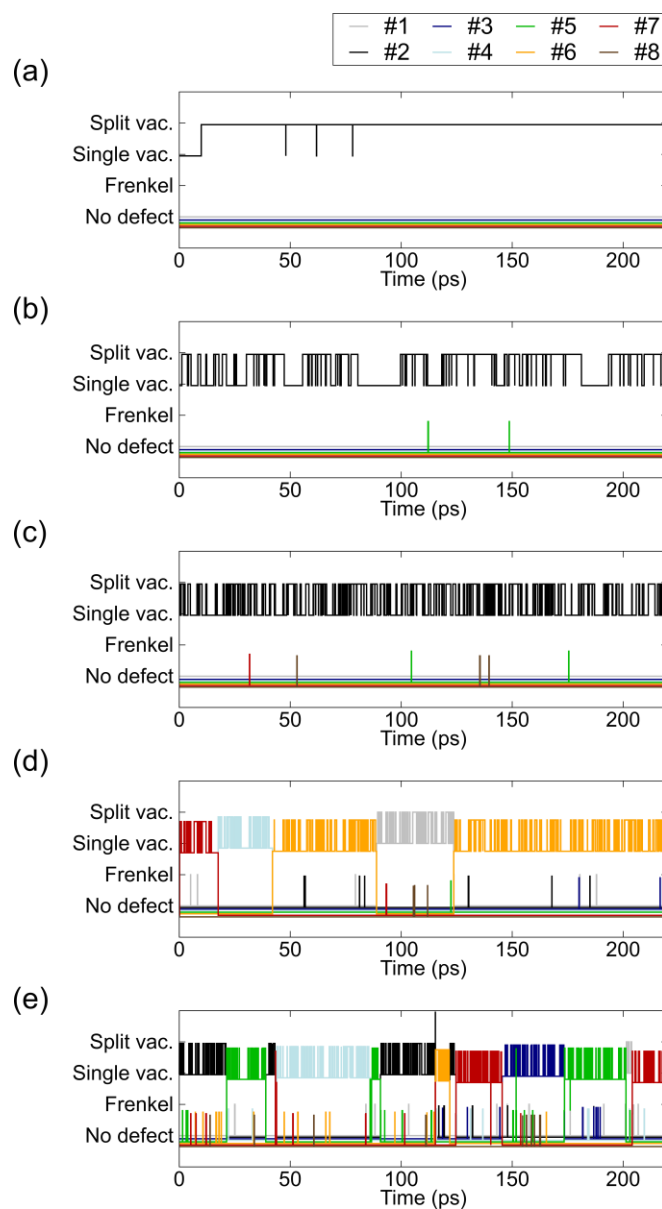


**Figure 3.A2.** Defect state diagrams of eight structural units of  $Y_2Ti_2O_7$  calculated at (a) 300 K, (b) 600 K, (c) 900 K, (d) 1200 K, and (e) 1500 K. Gray, black, navy blue, light blue, green, orange, red, and brown lines correspond to structural unit number #1, #2, #3, #4, #5, #6, #7, and #8, respectively.

## Appendix 3.C Pseudo-code of the Mapping Approach

---

Algorithm 1: Generation of time series of atom numbers on each site from atom trajectories and ideal lattice sites

---

Input: atom positions in the ground-state structure

Input: atom trajectories from NVT simulations

Output: atom number at site  $j$  at time  $t$

```
for t = 0 to maximum time step
  for i = 1 to number of anion sites
    distance_min = 1000000.0 # initialize
    for j = 1 to number of atoms
      for k = 1, 2, 3
        dr[k] = k component of the distance between ideal lattice site j and atom i
        distance = (dr[0]**2+ dr[1]**2+ dr[2]**2)**0.5
        if (distance < distance_min)
          site[t][i] = j
```

---

---

Algorithm 2: Conversion of atom numbers on each site each at each time step into data set of defect states of the structural units

---

Input: atom numbers on site  $j$  at time  $t$

Output: defect states of the structural units

for  $t = 0$  to maximum time step

    Initialize site numbers of each structural unit, `unit[]`

    # Specifically

    # `unit[0] = [0,1,2,3,4,5,6]`

    # `unit[1] = [7,8,9,10,11,12,13]`

    # ...

    # `unit[7] = [49, 50, 51, 52, 53, 54, 55]`

    # site numbers 0, 7, ..., 49 and the others correspond to 8a and 48f sites, respectively.

    for  $k = 1$  to number of structural units

        for  $i = 1$  to number of anion sites

            if `unit[k].include(site[t][i])`

`unit[k].delete(site[t][i])`

        if `unit[k].include(8a site)`

            if `unit[k].include(five oxygen atoms)`

`state[t][k] = 3` # Split vacancy

            if `unit[k].include(six oxygen atoms)`

`state[t][k] = 1` # Frenkel pair

        else

            if `unit[k].include(five oxygen atoms)`

`state[t][k] = 2` # Single vacancy

            if `unit[k].include(six oxygen atoms)`

`state[t][k] = 0` # No defect

---

## Bibliography

- [1] Yashima, M.; Tsujiguchi, T.; Sakuda, Y.; Yasui, Y.; Zhou, Y.; Fujii, K.; Torii, S.; Kamiyama, T.; Skinner, S. J. High Oxide-Ion Conductivity through the Interstitial Oxygen Site in Ba<sub>7</sub>Nb<sub>4</sub>MoO<sub>20</sub>-Based Hexagonal Perovskite Related Oxides. *Nat. Commun.* **2021**, *12*, 556.
- [2] Sakai, G.; Matsunaga, N.; Shimano, K.; Yamazoe, N. Theory of Gas-Diffusion Controlled Sensitivity for Thin Film Semiconductor Gas Sensor. *Sens. Actuators, B: Chem.* **2001**, *80*, 125–131.
- [3] Noda, Y.; Nakano, K.; Takeda, H.; Kotobuki, M.; Lu, L.; Nakayama, M. Computational and Experimental Investigation of the Electrochemical Stability and Li-Ion Conduction Mechanism of LiZr<sub>2</sub>(PO<sub>4</sub>)<sub>3</sub>. *Chem. Mater.* **2017**, *29*, 8983–8991.
- [4] He, X.; Zhu, Y.; Mo, Y. Origin of Fast Ion Diffusion in Super-Ionic Conductors. *Nat. Commun.* **2017**, *8*, 15893.
- [5] Li, H.; Okamoto, N. L.; Hatakeyama, T.; Kumagai, Y.; Oba, F.; Ichitsubo, T. Fast Diffusion of Multivalent Ions Facilitated by Concerted Interactions in Dual-Ion Battery Systems. *Adv. Energy Mater.* **2018**, *8*, 1801475.
- [6] Yang, X.; Fernández-Carrión, A. J.; Wang, J.; Porcher, F.; Fayon, F.; Allix, M.; Kuang, X. Cooperative Mechanisms of Oxygen Vacancy Stabilization and Migration in the Isolated Tetrahedral Anion Scheelite Structure. *Nat. Commun.* **2018**, *9*, 4484.
- [7] Moreno, K. J.; Mendoza-Suárez, G.; Fuentes, A. F.; García-Barriocanal, J.; León, C.; Santamaria, J. Cooperative Oxygen Ion Dynamics in Gd<sub>2</sub>Ti<sub>2-y</sub>Zr<sub>y</sub>O<sub>7</sub>. *Phys. Rev. B* **2005**, *71*, 7–10.
- [8] Kendrick, E.; Kendrick, J.; Knight, K. S.; Islam, M. S.; Slater, P. R. Cooperative Mechanisms of Fast-Ion Conduction in Gallium-Based Oxides with Tetrahedral Moieties. *Nat. Mater.* **2007**, *6*, 871–875.
- [9] Masson, O.; Berghout, A.; Béchade, E.; Jouin, J.; Thomas, P.; Asaka, T.; Fukuda, K. Local Structure and Oxide-Ion Conduction Mechanism in Apatite-Type Lanthanum Silicates. *Sci. Technol. Adv. Mater.* **2017**, *18*, 644–653.
- [10] Blöchl, P. E.; Smargiassi, E.; Car, R.; Laks, D. B.; Andreoni, W.; Pantelides, S. T. First-Principles Calculations of Self-Diffusion Constants in Silicon. *Phys. Rev. Lett.* **1993**, *70*, 2435–2438.

- [11] Zhang, Y.; Zhao, Y.; Chen, C. Ab Initio Study of the Stabilities of and Mechanism of Superionic Transport in Lithium-Rich Antiperovskites. *Phys. Rev. B* **2013**, *87*, 134303.
- [12] Mo, Y.; Ong, S. P.; Ceder, G. First Principles Study of the  $\text{Li}_{10}\text{GeP}_2\text{S}_{12}$  Lithium Super Ionic Conductor Material. *Chem. Mater.* **2012**, *24*, 15–17.
- [13] Kuo, P. H.; Du, J. Lithium Ion Diffusion Mechanism and Associated Defect Behaviors in Crystalline  $\text{Li}_{1+x}\text{Al}_x\text{Ge}_{2-x}(\text{PO}_4)_3$  Solid-State Electrolytes. *J. Phys. Chem. C* **2019**, *123*, 27385–27398.
- [14] Askar, A.; Cetin, A. E.; Rabitz, H. Wavelet Transform for Analysis of Molecular Dynamics. *J. Phys. Chem.* **1996**, *100*, 19165–19173.
- [15] Biswas, S.; Mallik, B. S. Vibration Spectral Dynamics of Weakly Coordinating Water Molecules near an Anion: FPMD Simulations of an Aqueous Solution of Tetrafluoroborate. *J. Phys. Chem. B* **2019**, *123*, 2135–2146.
- [16] Argoul, F.; Arneodo, A.; Elezgaray, J.; Grasseau, G.; Murenzi, R. Wavelet Analysis of the Self-Similarity of Diffusion-Limited Aggregates and Electrodeposition Clusters. *Phys. Rev. A* **1990**, *41*, 5537–5560.
- [17] Wang, R.; Jiang, W.; Qu, Z.; Zhu, Y.; Yang, Y.; Wang, Z. Intermolecular Vibrational Energy Transfers in Nitro-Energetic Molecules: A First-Principles Molecular Dynamics Study. *Chem. Phys. Lett.* **2019**, *733*, 136675.
- [18] Phillips, S. C.; Gledhill, R. J.; Essex, J. W.; Edge, C. M. Application of the Hilbert-Huang Transform to the Analysis of Molecular Dynamics Simulations. *J. Phys. Chem. A* **2003**, *107*, 4869–4876.
- [19] Uematsu, K.; Shinozaki, K.; Sakurai, O.; Mizutani, N.; Kato, M. Electrical Conductivity of the System  $\text{Y}_2\text{O}_3\text{-TiO}_2$ . *J. Am. Ceram. Soc.* **1979**, *62*, 219–221.
- [20] Pirzada, M.; Grimes, R. W.; Minervini, L.; Maguire, J. F.; Sickafus, K. E. Oxygen Migration in  $\text{A}_2\text{B}_2\text{O}_7$  Pyrochlores. *Solid State Ion.* **2001**, *140*, 201–208.
- [21] Li, Y.; Kowalski, P. M. Energetics of Defects Formation and Oxygen Migration in Pyrochlore Compounds from First Principles Calculations. *J. Nucl. Mater.* **2018**, *505*, 255–261.

- [22] Uno, W.; Fujii, K.; Niwa, E.; Torii, S.; Miao, P.; Kamiyama, T.; Yashima, M. Experimental Visualization of Oxide-Ion Diffusion Paths in Pyrochlore-Type  $\text{Yb}_2\text{Ti}_2\text{O}_7$ . *J. Ceram. Soc. Jpn.* **2018**, 126, 341–345.
- [23] Tanaka, M.; Matsudaira, T.; Kawai, E.; Kawashima, N.; Matsumoto, U.; Ogawa, T.; Takeuchi, M.; Kitaoka, S. Effect of Chemical Composition on Mass Transfer in  $\text{Y}_2\text{Ti}_2\text{O}_7$  under Oxygen Potential Gradient at High Temperatures. *J. Ceram. Soc. Jpn.* **2021**, 129, 22–31.
- [24] Blatov, V. A. Voronoi-Dirichlet Polyhedra in Crystal Chemistry: Theory and Applications. *Crystallogr. Rev.* **2004**, 10, 249–318.
- [25] Henkelman, G.; Jónsson, H. Improved Tangent Estimate in the Nudged Elastic Band Method for Finding Minimum Energy Paths and Saddle Points. *J. Chem. Phys.* **2000**, 113, 9978–9985.
- [26] Henkelman, G.; Uberuaga, B. P.; Jónsson, H. Climbing Image Nudged Elastic Band Method for Finding Saddle Points and Minimum Energy Paths. *J. Chem. Phys.* **2000**, 113, 9901–9904.
- [27] Blöchl, P. E. Projector Augmented-Wave Method. *Phys. Rev. B* **1994**, 50, 17953–17979.
- [28] Kresse, G.; Furthmüller, J. Efficient Iterative Schemes for Ab Initio Total-Energy Calculations Using a Plane-Wave Basis Set. *Phys. Rev. B* **1996**, 54, 11169–11186.
- [29] Kresse, G.; Hafner, J. Ab Initio Molecular Dynamics for Liquid Metals. *Phys. Rev. B* **1993**, 47, 558–561.
- [30] Perdew, J. P.; Burke, K.; Ernzerhof, M. Generalized Gradient Approximation Made Simple. *Phys. Rev. Lett.* **1997**, 78, 1396–1396.
- [31] Monkhorst, H. J.; Pack, J. Special Points for Brillouin-Zone Integrations. *Phys. Rev. B* **1976**, 13, 5188–5192.
- [32] Cococcioni, M.; de Gironcoli, S. Linear Response Approach to the Calculation of the Effective Interaction Parameters in the LDA+U Method. *Phys. Rev. B* **2005**, 71, 035105.
- [33] Wang, X.; Xie, J.; Wang, Z.; Zhou, G.; Shi, Y.; Wang, S.; Mao, X. Fabrication and Properties of  $\text{Y}_2\text{Ti}_2\text{O}_7$  Transparent Ceramics with Excess Y Content. *Ceram. Int.* **2018**, 44, 9514–9518.

- [34] Suganya, M.; Ganesan, K.; Vijayakumar, P.; Gill, A. S.; Ramaseshan, R.; Ganesamoorthy, S. Structural, Optical and Mechanical Properties of  $Y_2Ti_2O_7$  Single Crystal. *Scr. Mater.* **2020**, 187, 227–231.
- [35] Merka, O.; Bahnemann, D. W.; Wark, M. Improved Photocatalytic Hydrogen Production by Structure Optimized Nonstoichiometric  $Y_2Ti_2O_7$ . *ChemCatChem* **2012**, 4, 1819–1827.
- [36] Jiang, Y.; Smith, J. R.; Robert Odette, G. Prediction of Structural, Electronic and Elastic Properties of  $Y_2Ti_2O_7$  and  $Y_2TiO_5$ . *Acta Mater.* **2010**, 58, 1536–1543.
- [37] Parrinello, M.; Rahman, A. Polymorphic Transitions in Single Crystals: A New Molecular Dynamics Method. *J. Appl. Phys.* **1981**, 52, 7182–7190.
- [38] Parrinello, M.; Rahman, A. Crystal Structure and Pair Potentials: A Molecular-Dynamics Study. *Phys. Rev. Lett.* **1980**, 45, 1196–1199.
- [39] Hoover, W. G. Canonical Dynamics: Equilibrium Phase-Space Distributions. *Phys. Rev. A* **1985**, 31, 1695–1697.
- [40] Nosé, S. A Unified Formulation of the Constant Temperature Molecular Dynamics Methods. *J. Chem. Phys.* **1984**, 81, 511–519.
- [41] Togo, A.; Tanaka, I.; Oba, F.; Tanaka, I. First-Principles Calculations of the Ferroelastic Transition between Rutile-Type and  $CaCl_2$ -Type  $SiO_2$  at High Pressures. *Scr. Mater.* **2008**, 108, 134106.
- [42] Togo, A.; Tanaka, I. First Principles Phonon Calculations in Materials Science. *Scr. Mater.* **2015**, 108, 1–5.
- [43] Parlinski, K.; Li, Z. Q.; Kawazoe, Y. First-Principles Determination of the Soft Mode in Cubic  $ZrO_2$ . *Phys. Rev. Lett.* **1997**, 78, 4063–4066.
- [44] Details are described in Chapter 4.
- [45] Joseph, D.; Kaliyaperumal, C.; Mummoorthy, S.; Paramasivam, T. Dependence on Temperature of the Electrical Properties of Nanocrystalline  $Y_2Ti_2O_7$  Ceramics. *Ceram. Int.* **2018**, 44, 5426–5432.
- [46] Gill, J. K.; Pandey, O. P.; Singh, K. Role of Sintering Temperature on Thermal, Electrical and Structural Properties of  $Y_2Ti_2O_7$  Pyrochlores. *Int. J. Hydrog. Energy* **2011**, 36, 14943–14947.

[47] Nakamura, K.; Mori, M.; Itoh, T.; Ohnuma, T. Theoretical and Experimental Investigation of Defect Formation / Migration in  $Gd_2Ti_2O_7$ : General Rule of Oxide-Ion Migration in  $A_2B_2O_7$  Pyrochlore. *AIP Adv.* **2016**, *6*, 115003.

## Chapter 4

### First-Principles Study on the Stability of Weberite-type,

### Pyrochlore, and Defect-Fluorite Structures of $A_2B_2O_7$ ( $A = \text{Lu}^{3+} - \text{La}^{3+}$ , $B = \text{Zr}^{4+}$ , $\text{Hf}^{4+}$ , $\text{Sn}^{4+}$ and $\text{Ti}^{4+}$ )

#### 4.1 Introduction

$A_2^{3+}B_2^{3+}O_7$  ( $A =$  trivalent cations,  $B =$  tetravalent cations) oxides with defect-fluorite (DF) based structures are being considered for application in solid oxide fuel cells,<sup>1,2</sup> thermal barrier coatings,<sup>3-5</sup> and materials<sup>6,7</sup> for actinide immobilization in nuclear waste because they have high ionic conductivity, low thermal conductivity and high tolerance against radiation damage, as well as suitable mechanical properties. These physical and chemical properties are closely related to the degree of short- and/or long-range order of component atoms.<sup>8-10</sup> Thus, elucidating the key factors controlling ordered or disordered atomic arrangements is essential when tailoring atomic structures to provide enhanced performance.

A well-known ordered structure for  $A_2B_2O_7$  compounds is the cubic pyrochlore structure, being composed of two types of cation sites and three types of sites for anions (Figure 4.1a). Transitions between the pyrochlore structure and the defect-fluorite structure, with disordering on both cation and anion sites (Figure 4.1b), are triggered by changes in temperature, pressure, and composition, and have been abundantly studied. Systematic studies on the energetic stability of  $A_2B_2O_7$  compounds by Subramanian et al.<sup>11</sup> suggested that compounds with a larger ionic radius ratio ( $r_A/r_B > 1.46$ ) preferentially form in the pyrochlore structure rather than the defect-fluorite structure. This tendency was examined via the defect formation energies of Frenkel pairs on each cation and anion sublattice

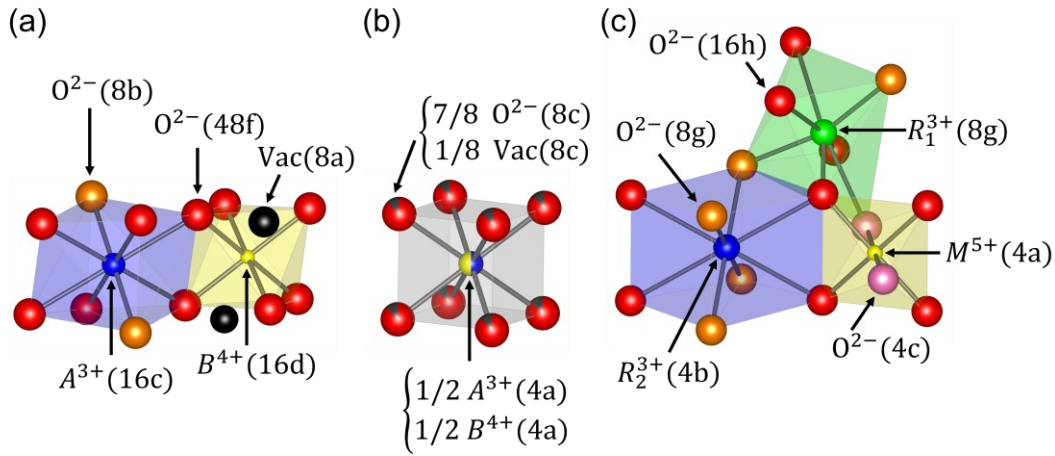


**Figure 4.1.** Local structures of (a) pyrochlore, (b) defect-fluorite, and (c) *2OIII*-type weberite structures.

determined from atomic-scale simulations.<sup>12-15</sup> More recently, trends of transition temperatures in  $A_2B_2O_7$  were partially reproduced by computing the disordering energies from pyrochlore to defect-fluorite using first-principles calculations.<sup>16</sup>

Another type of ordered structure related to the weberite structure was postulated by Shamblin et al.<sup>17</sup> using pair distribution function (PDF) analysis based on neutron diffraction total scattering for  $\text{Ho}_2\text{Zr}_2\text{O}_7$ , which had been identified as a defect-fluorite structure with disordered atomic arrangements. The weberite structures are also derivatives of the defect-fluorite structure and are formed in  $A_2^3+B_2^3+O_7$  compounds such as  $\text{Ca}_2^2+\text{Sb}_2^5+O_7$  (*2O*-type) and in  $R_3^3+M^5+O_7$  ( $R$  = rare-earth element,  $M = \text{Ta}$  and  $\text{Nb}$ ) compounds such as  $\text{La}_3^3+\text{Ta}^5+O_7$  (*2OIII*-type).<sup>18,19</sup> The proposed orthorhombic  $\text{Ho}_2\text{Zr}_2\text{O}_7$  structure was constructed by substituting cation atoms in *2OIII*-type  $R_3MO_7$  weberite with the space group *Ccmm* (Figure 4.1c), in which 8g sites were shared by Ho and Zr cations, and 4a and 4b sites were fully occupied by Ho and Zr cations, respectively. Although the weberite-type structure is possibly formed in a wide range of  $A_2B_2O_7$  compounds, identification of the structure has yet to be elaborated on, probably due to the following two reasons: (1) Such weberite-type structures are prone to aperiodic modulation on a nanometer-scale, forming numerous

tiny subdomains in crystals and causing any anisotropy to disappear,<sup>17</sup> and (2) the ordering process to form the weberite-type arrangements strongly depends on the heat treatment, especially at relatively low temperatures compared to the usual sintering temperatures. Indeed, the effects of thermal history on the structures are largely unknown, which hinders the preparation of homogeneous samples. It has therefore been difficult to reveal the details of weberite-type structures from an experimental perspective.

Since the weberite-type structures are represented by a two-sublattice model in the defect-fluorite structure, we can expect that first-principles calculations for exhaustively generated structures can enable us to search for the ground-state structure in an  $A_2B_2O_7$  system within the given unit cell. In this work, we adopted this methodology for the  $Yb_2Ti_2O_7$  system.  $Yb_2Ti_2O_7$  is one of the materials with relatively high oxide-ion conductivity among  $A_2B_2O_7$  compounds<sup>20</sup> and its conductivity is strongly influenced by the sintering temperature. While  $Yb_2Ti_2O_7$  is known to form the pyrochlore structure by the usual solid-state reaction synthesis at a high temperature, it has been reported that the 100 reflection peak of the X-ray diffraction (XRD) patterns becomes weak by annealing at lower temperatures, which suggests the formation of, or transformation to, a different ordered state.<sup>21,22</sup> In the present study, we show that a weberite-type structure with layered arrangements of cations can be formed as the lowest-energy state, whereas the pyrochlore-related structure is the second-most stable. After structural characters of the weberite-type structure are described, the finite-temperature stability of the structure in comparison to pyrochlore is also shown. Finally, we compare the energetic stabilities of the weberite-type, pyrochlore, and defect-fluorite structures for a wide range of  $A_2^{3+}B_2^{3+}O_7$  ( $A = Lu^{3+}$ – $La^{3+}$ ,  $B = Zr^{4+}$ ,  $Hf^{4+}$ ,  $Sn^{4+}$ , and  $Ti^{4+}$ ). Here, defect-fluorite structures are represented by special quasi-random structures (SQS).

## 4.2 Calculation Methods

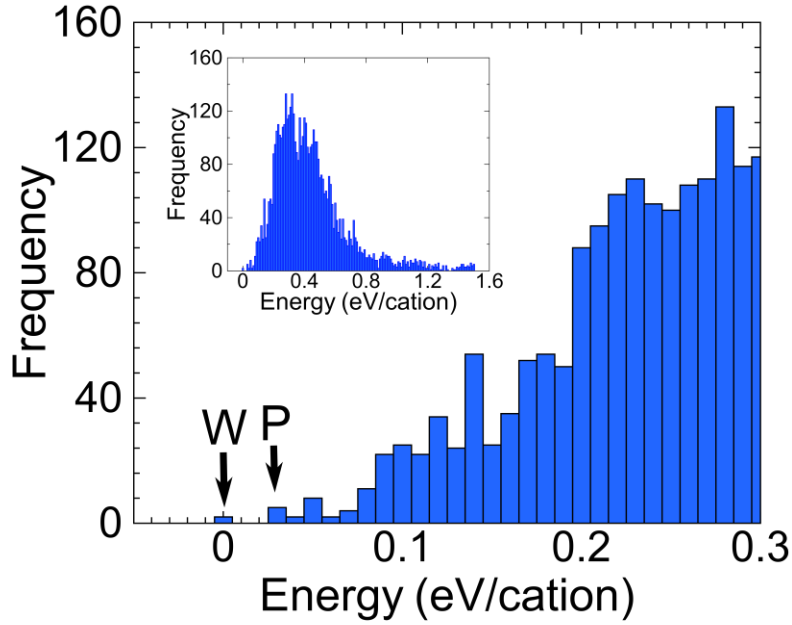
The low-energy structures of  $\text{Yb}_2\text{Ti}_2\text{O}_7$  compounds were searched among derivative structures constructed from a fluorite cell, which consists of a face-centered cubic (fcc) lattice for cations and a simple cubic lattice for anions. We generated all unique atomic configurations for  $\text{Yb}_2\text{Ti}_2\text{O}_7$  within 8 cation sites and 16 anion sites, fixing cation and anion sublattices, by the Alloy Theoretic Automated Toolkit (ATAT).<sup>23</sup> The number of configurations was 6386.

All first-principles calculations were performed using the projector augmented wave (PAW) method<sup>24</sup> within the framework of density functional theory (DFT) as implemented in the Vienna Ab initio Simulation Package (VASP).<sup>25,26</sup> Generalized gradient approximation (GGA) functional with the Perdew–Burke–Ernzerhof parametrization adapted for solids (PBEsol)<sup>27,28</sup> was used to treat the exchange–correlation interactions. Brillouin zone integration was performed using the Monkhorst–Pack  $k$ -point mesh<sup>29</sup> and a Gaussian smearing approach with a smearing width of 0.01 eV. For the exhaustive search in  $\text{Yb}_2\text{Ti}_2\text{O}_7$ , we set undemanding conditions to reduce the total calculation time. The cutoff energy for plane-wave basis sets was set as 370 eV. Brillouin zones (BZs) of all structures are integrated with  $k$ -point spacings of no more than  $0.5 \text{ \AA}^{-1}$ . The 2s and 2p orbitals for O atoms, 3d and 4s orbitals for Ti atoms, and 4s, 4p, 4d and 5s orbitals for Yb atoms were treated as valence states. Atomic positions were fully optimized until the residual forces became less than  $0.05 \text{ eV/\AA}$ , with the lattice constant fixed to that of the ideal pyrochlore structure. For examining the absence of soft modes and calculating the vibrational contribution to free energies for  $\text{Yb}_2\text{Ti}_2\text{O}_7$ , phonon calculations were performed in the harmonic approximation after optimization of structures and lattice constants. Here, we employed a more stringent convergence criterion than that in the exhaustive-search case: The tolerance for structural optimizations was set to  $0.002 \text{ eV/\AA}$ . The largest  $k$ -point spacing along any reciprocal cell vector is below  $0.3 \text{ \AA}^{-1}$ . The interatomic force constants were calculated by the Parlinski–Li–Kawazoe method<sup>30</sup> as implemented in the phonopy code.<sup>31,32</sup>

Regarding systematic calculations of weberite, pyrochlore, and defect-fluorite structures for  $A_2B_2O_7$ , the structures were fully optimized until the residual forces became less than  $0.02 \text{ eV/\AA}$ . The largest  $k$ -point spacing along any reciprocal cell vector is below  $0.3 \text{ \AA}^{-1}$ . PAW potentials without explicit  $f$ -orbitals were selected for the  $A$  cations. While the pseudopotentials of Ti and O atoms were the same as in the previous case,  $5p$ ,  $6s$ , and  $5d$  orbitals for Hf atoms,  $4s$ ,  $4p$ ,  $4d$ , and  $5s$  orbitals for Zr atoms, and  $2s$  and  $2p$  orbitals for Sn atoms were treated as valence states. We prepared five 88-atom SQS models<sup>33</sup> with the conventional pyrochlore cell as models of fully defect-fluorite structures. Monte Carlo (MC) simulations were performed five times using a different random seed until the objective functions reached a sufficiently low level ( $< 0.01$ ) using ATAT mcsqs code.<sup>34</sup> The objective functions contained up to four-body correlations.

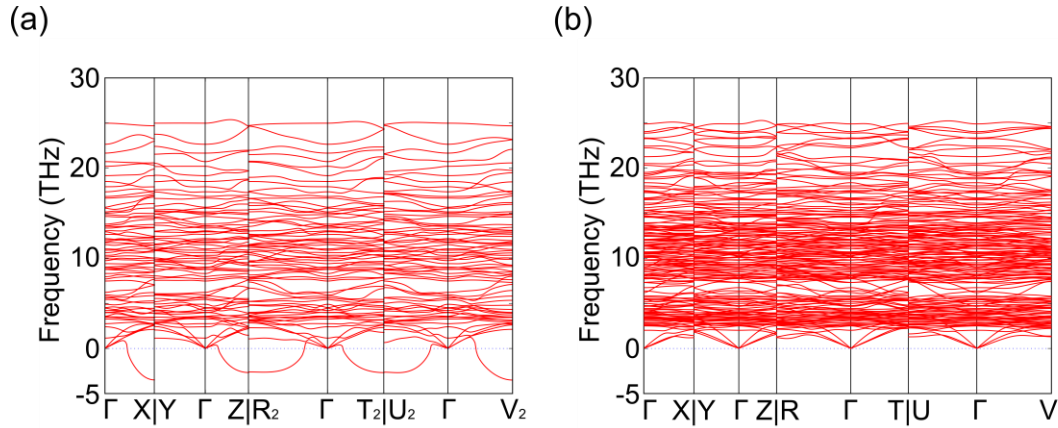
### 4.3 Results and Discussion

Figure 4.2 shows a histogram of calculated  $\text{Yb}_2\text{Ti}_2\text{O}_7$  energies relative to the lowest energy, obtained for 2-fold structures with almost the same energy and structure. Although the two lowest-energy structures originate from different initial configurations, we regard the resulting structures as identical. The characteristic feature of the structures is a layer-type arrangement of cations, as will be described in detail below. The pyrochlore structure appears as the second-lowest-energy state, with higher energy by  $0.035 \text{ eV/cation}$ . After full optimization with lattice constants, their energy difference was slightly changed to  $0.043 \text{ eV/cation}$ . Other structures in the energy region less than  $0.067 \text{ eV/cation}$  are similar to the structure in terms of cation arrangements, but they adopt different anion configurations.



**Figure 4.2.** Histogram of Yb<sub>2</sub>Ti<sub>2</sub>O<sub>7</sub> energies exhaustively calculated, measured from the lowest energy. The inset exhibits the whole range of energies. Symbols W and P represent weberite-type and pyrochlore, respectively.

The calculated phonon dispersion of the structure with triclinic symmetry (space group:  $P\bar{1}$ ) has an imaginary mode, as shown in Figure 4.3a. As shown in the figure, the imaginary mode appears at X, Z, R<sub>2</sub>, T<sub>2</sub>, U<sub>2</sub>, and V<sub>2</sub>  $q$ -points. We relax the structures with a shift of atomic positions in a supercell toward the directions of the eigenvectors of the imaginary mode. Among the six cases, the structure with shifts along the direction of the T<sub>2</sub>  $q$ -point has the lowest energy, with a difference in energy of 0.011 eV/cation compared to that before the optimization. While the energeti and structural changes during the optimization are small, the calculated phonon dispersion of the new structure exhibits no imaginary modes, as shown in Figure 4.3b, indicating that the finally obtained structure can be a candidate for the ground state in the Yb<sub>2</sub>Ti<sub>2</sub>O<sub>7</sub> system. As will be explained in the following part, the structure can be specified as an instance of weberite structure so that we label the structure as a “weberite-type” structure.



**Figure 4.3.** Phonon band structure of the weberite-type structures of  $\text{Yb}_2\text{Ti}_2\text{O}_7$ , (a) obtained from the exhaustive search and (b) after vanishing the soft mode appearing in (a).

The symmetry of the weberite-type structure is lowered to triclinic, as summarized in Table 4.A1 in Appendix 4A while the pyrochlore and defect-fluorite structures hold cubic symmetry. Table 4.A2 in Appendix 4B listed the resulting positional parameters, and the weberite-type structure is depicted in Figures 4.4a–c. The most notable characteristic of the structure is the presence of the alternately ordered Yb and Ti layers, as seen in Figure 4.4b. The cation layer planes correspond to the  $(111)_{\text{DF}}$  planes of the defect-fluorite (DF) crystal. The arrangement pattern can be confirmed more clearly in the preoptimized configuration, as shown in Figure 4.A1b in Appendix 4.C, by comparison to the pyrochlore case shown in Figure 4.A1a in Appendix 4.C. As seen in the figures, both structures are commonly composed of the same type of chain arrangements of Yb and Ti atoms on the  $(110)_{\text{DF}}$  planes, but there is a difference in the stacking sequence in the  $[100]_{\text{DF}}$  direction: While the planes stack in a straightforward manner in the weberite-type structure, the neighboring planes are rotated by  $90^\circ$  to each other in the pyrochlore structure.

The coordination environments of cations in the weberite-type structure are different from those of pyrochlore. The cation coordination in the weberite-type  $\text{Yb}_2\text{Ti}_2\text{O}_7$  is categorized into 7- or

8-fold coordination for Yb cations and 6- or 7-fold coordination for Ti cations in contrast to the pyrochlore case, where Yb and Ti cations have 8- and 6-fold coordinations, respectively. Figure 4.4d,e shows the extracted Yb and Ti layers, respectively, where the atomic spheres are colored differently for each coordination of each cation. As shown in Figure 4.4d, Yb polyhedra with 7- and 8-fold coordinations are, respectively, linked into chains, and Yb atoms form a triangular lattice with a certain amount of distortion. Arrangements of Ti atoms on the Ti layers are dispersive, as shown in Figure 4.4e, which is attributed to the presence of oxygen defects on neighboring sites on the O-sublattice in the pristine defect-fluorite cell.

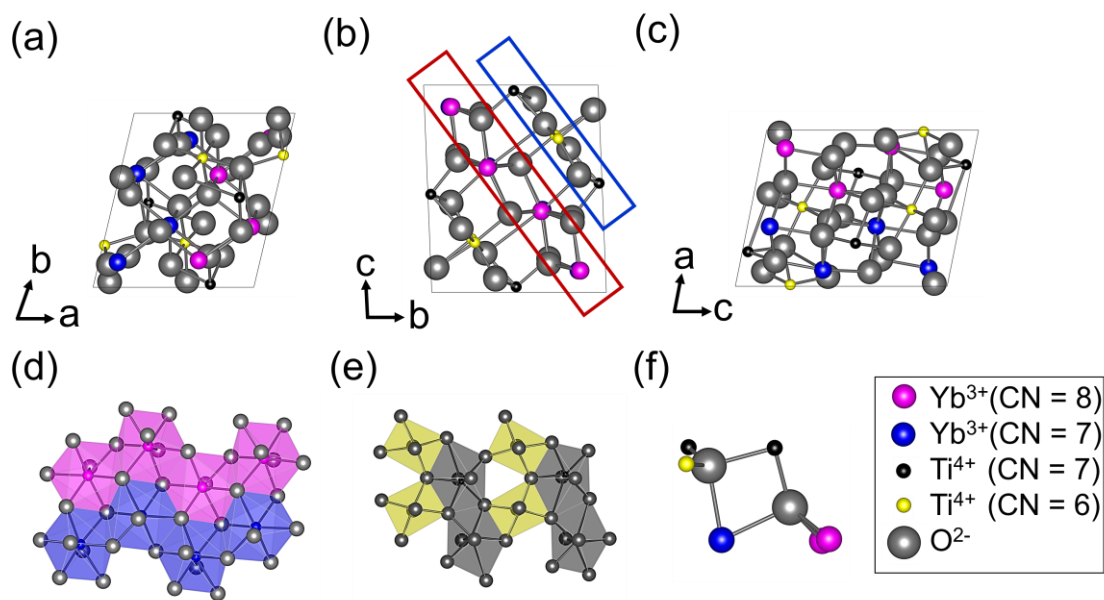


**Figure 4.4.** Crystal structure of weberite-type  $\text{Yb}_2\text{Ti}_2\text{O}_7$ , viewed along the (a)  $c$  axis, (b)  $a$  axis and (c)  $b$  axis, extracted (d) Yb and (e) Ti layers and (f) coordination environments of O atoms. The blue and pink spheres indicate  $\text{Yb}^{3+}$  (CN = 7) and  $\text{Yb}^{3+}$  (CN = 8), respectively, and the yellow and black spheres indicate  $\text{Ti}^{4+}$  (CN = 6) and  $\text{Ti}^{4+}$  (CN = 7), respectively. The small gray spheres are  $\text{O}^{2-}$ . CN means coordination numbers (CNs). The Yb and Ti layers in (d) and (e) are indicated by the red and blue rectangles in (b), respectively. There are two types of oxygen coordination as shown in (f): surrounded by  $3\text{Yb} + \text{Ti}$  and  $\text{Yb} + 3\text{Ti}$  atoms.

The coordination numbers (CNs) of anions are commonly 4 for both the weberite-type and pyrochlore structures, but there are differences in the combinations of coordinating cations, as

**Table 4.1.** Coordination environments of oxygen sites in weberite-type and ideal pyrochlore structures.<sup>a</sup>

crystal structure	oxygen site occupancy	neighboring cations				
		4Yb	3Yb + Ti	2Yb + 2Ti	Yb + 3Ti	4Ti
pyrochlore	occupied	1		6		0
	unoccupied	0		0		1
weberite-type	occupied		4		3	
	unoccupied		0		1	

<sup>a</sup> Total number of oxygen atoms (occupied sites) and vacancies (unoccupied sites) is normalized to 8.

summarized in Table 4.1. The coordination environments of anion sites in the weberite-type structure consist of two types of cation combinations: 3Yb + Ti and Yb + 3Ti, as shown in Figure 4.4f. Oxygen sites surrounded by 3Yb + Ti atoms are fully occupied, and those surrounded by Yb + 3Ti atoms are partially occupied with an occupancy ratio of 0.75. 4Yb, 2Yb + 2Ti, and 4Ti coordination environments are not possible due to the layered arrangement of cations in the weberite-type structure. In contrast, in the pyrochlore structure, there are 4Yb, 2Yb + 2Ti, and 4Ti coordination environments for oxygen sites, and the former two sites are fully occupied (Table 4.1). These results suggest that oxygen atoms tend to avoid coordinating to Ti atoms and prefer to increase their coordination to Yb atoms.

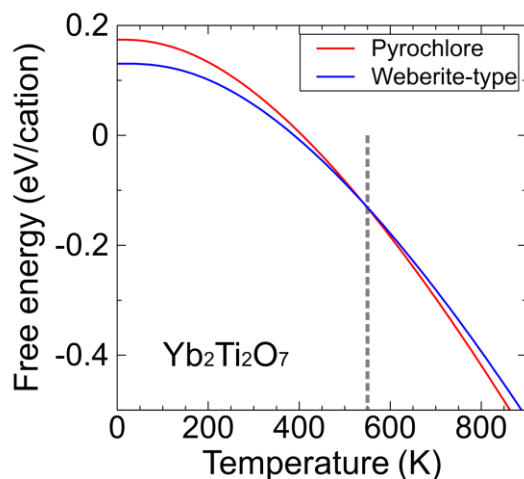
The weberite-type structure exhibits a configuration of superstructure derived from  $\text{Ho}_2\text{Zr}_2\text{O}_7$  2OIII-type structure by Shamblin et al.<sup>17</sup> with space group *Ccmm*.<sup>19</sup> As shown in Figure 4.1c, there are three types of cation sites in 2OIII-type weberite  $\text{Yb}_3\text{TaO}_7$ ; 4*b* for Yb, 8*g* for Yb, and 4*a* for Ta, with 8-, 7-, and 6-fold coordinations, respectively. Shamblin et al. constructed the weberite-type  $\text{Ho}_2\text{Zr}_2\text{O}_7$  structure as follows: While 8*g* sites of 2OIII-type weberite are shared by *A* and *B* atoms of  $\text{A}_2\text{B}_2\text{O}_7$  in a mixed way, 4*b* and 4*a* sites are occupied by *A* and *B* atoms, respectively. By partitioning the shared sites into two types of sites occupied with *A* and *B* atoms as shown in Figure 4.A2 in

Appendix 4.D, we can reproduce the configuration obtained from our exhaustive search. Therefore, the weberite-type structure we found can be regarded as an ordered structure of  $\text{Yb}_3\text{TaO}_7$ -based weberite  $A_2B_2O_7$  containing fractional cation sites.

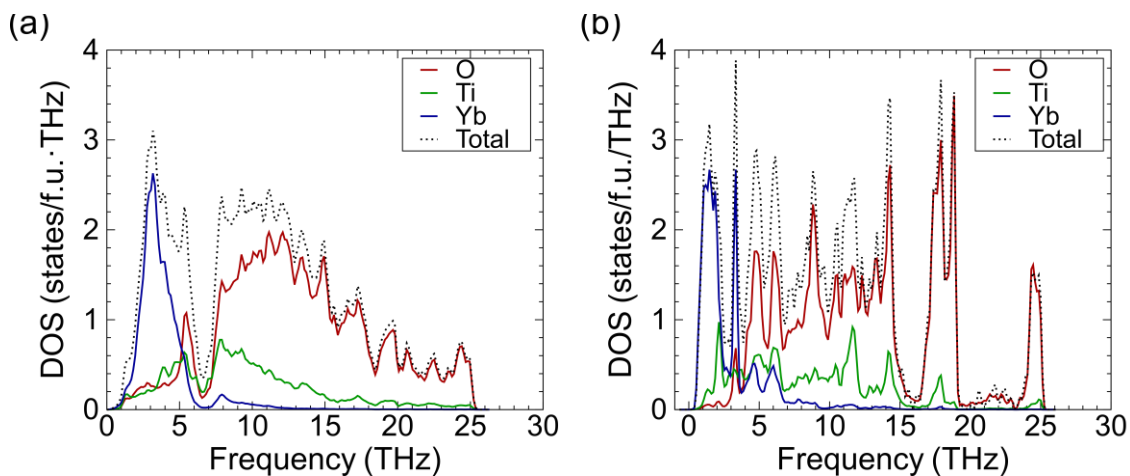
The calculated free energies of the weberite-type and pyrochlore structures, including vibrational contributions obtained by first-principles phonon calculations, are shown in Figure 4.5. Although the weberite-type structure is energetically favored than the pyrochlore structure by 0.044 eV/cation at 0 K, the free energy curves have a crossing point at 550 K. Hence, the pyrochlore structure is favored than the weberite-type structure at above 550 K. This implies the difficulty in producing homogeneous samples where the weberite-type structure prevails, through usual solid-state reactions due to the kinetic controlled regime. Actually, in the experiment of  $\text{Yb}_2\text{Ti}_2\text{O}_7$ , intensity of the 100 reflection peak in the XRD pattern of pyrochlore structure was weakened by sintering at relatively low temperatures, but the change was too subtle to provide a clear conclusion.<sup>21</sup> On the other hand, short-range weberite-type-ordering structures were identified for  $\text{Er}_2\text{Ti}_2\text{O}_7$  when synthesized by ball milling, but pyrochlore in  $\text{Er}_2\text{Ti}_2\text{O}_7$  was recovered by annealing at a relatively high temperature near 800 K.<sup>35</sup> This result suggests the possibility that weberite-type structure is stable at low temperatures. Since the ionic radii of  $\text{Er}^{3+}$  (0.890 Å) and  $\text{Yb}^{3+}$  (0.868 Å) are close to each other, such behaviors are expected to be common. Finally, our calculations show similar stability tendencies for  $\text{Er}_2\text{Ti}_2\text{O}_7$  and  $\text{Yb}_2\text{Ti}_2\text{O}_7$  at 0 K, as described later.

Figure 4.6a,b shows the partial and total phonon density of states (DOS) of the weberite-type and pyrochlore structures, respectively. In both cases, while the vibrational contributions of Yb atoms lie in the relatively low-frequency range lower than 5 THz, the contributions of Ti and O atoms are distributed over a wide frequency range. This trend is mainly ascribed to the different mass and stronger covalent bonding of Ti–O: average values of bond lengths of Yb–O and Ti–O are 2.29 Å and 2.00 Å, respectively. The partial DOS of Yb atoms of weberite-type is more broadened than those

of pyrochlore, which would originate from the lower CN and distorted coordination environments of the Yb cations in the weberite-type structure. These changes in the low-frequency modes are considered to induce the changes in the temperature dependences of the free energies between the two structures.



**Figure 4.5.** Free energy as a function of temperature for weberite-type and pyrochlore structures. The vertical dashed line represents the transition temperature.



**Figure 4.6.** Phonon density of states (DOS) of (a) weberite-type and (b) pyrochlore structures for  $\text{Yb}_2\text{Ti}_2\text{O}_7$ . Partial DOS of each atom and total DOS are depicted by solid and dotted curves, respectively. Red, green, and blue lines represent O, Ti, and Yb atoms, respectively.

Figure 4.7 shows the relative energies of the weberite-type structure against the pyrochlore structure for  $A_2B_2O_7$  as a function of the Shannon's ionic radius of  $A^{3+}$  cations.<sup>36</sup> The relative energies, for each  $B^{4+}$  cation, increase as the ionic radius of  $A^{3+}$  cation decreases. This trend indicates that the relative stability continuously changes as a function of the ionic radius of  $A^{3+}$  cation. For  $A_2Zr_2O_7$  ( $A = \text{Lu-Nd}$ ),  $A_2\text{Hf}_2O_7$  ( $A = \text{Lu-Sm}$ ), and  $A_2\text{Ti}_2O_7$  ( $A = \text{Lu-Dy}$ ), since the relative energies are negative, we can conclude that the weberite-type structure is stable relative to pyrochlore in such a wide range of compositions at 0 K.

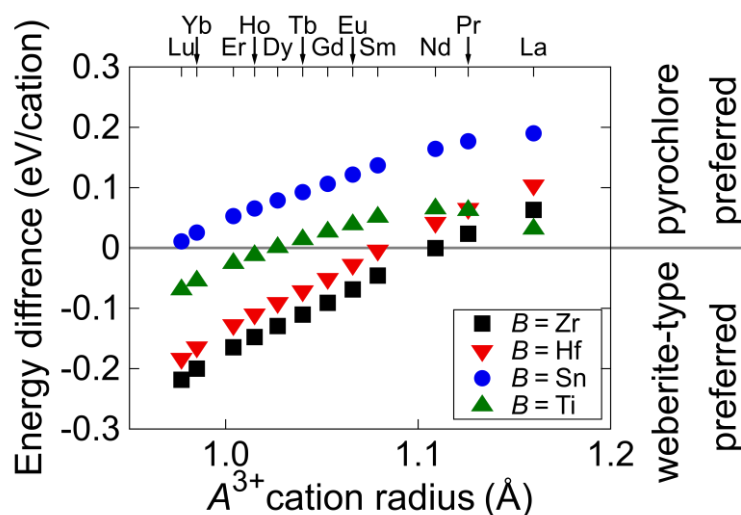


**Figure 4.7.** Difference in energy between weberite-type and pyrochlore for lanthanoid zirconates (black squares), hafnates (red downward triangles), stannates, (blue circles), and titanates (green upward triangles).

We also examined relative energies of the ordered (weberite-type and pyrochlore) structures for  $A_2B_2O_7$  with respect to the disordered structures, as modeled by SQS at 0 K. As shown in Figure 4.8, the relative energies are scattered by 0.2 eV/cation at most because the energies of the disordered structures are scattered depending on the choice of SQS models. The trends in relative energies between pyrochlore and SQS models agree with the results in the early report by Jiang et al.<sup>16</sup> Although there are small differences in energy, they are smaller than the scatter of the total energy

with the choice of SQS models. Limitations in the present approach to treat the disordered structures will be described later in this paper. We will make some qualitative discussion based on the results shown in Figure 4.8.

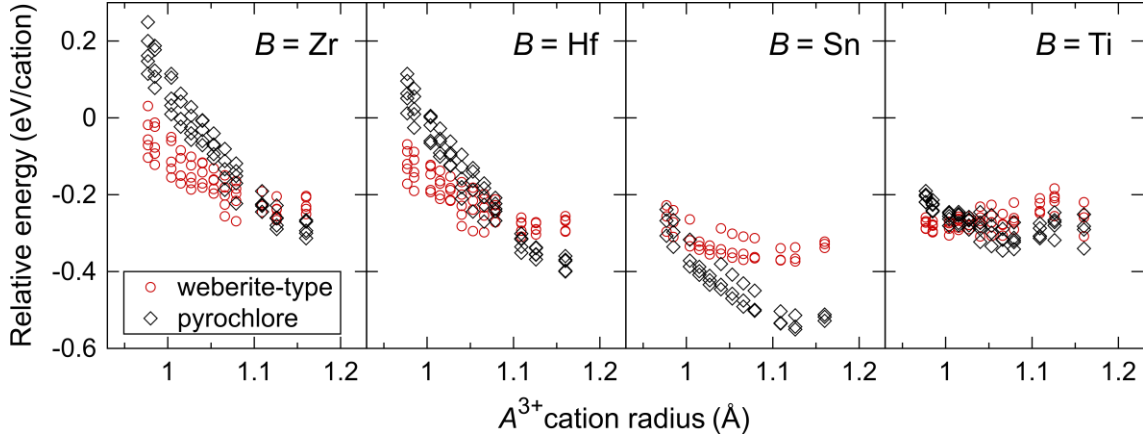


**Figure 4.8.** Energies of ordered (weberite-type and pyrochlore) structures of  $A_2B_2O_7$  zirconates, hafnates, stannates and titanates relative to energies of five different special quasi-random structures (SQS) models of the defect-fluorite structure.

The relative stability of defect-fluorite increases with the increase of temperature due to the contribution of mixing entropy. This corresponds to the addition of the entropy term  $-T\Delta S_{\text{mix}}$  to the relative energy, where mixing entropy,  $\Delta S_{\text{mix}}$ , is given by  $\Delta S_{\text{mix}} = -k_B[x_C \ln x_C + (1 - x_C) \ln(1 - x_C) + 2x_A \ln x_A + 2(1 - x_A) \ln(1 - x_A)]$ . Here,  $x_C = 1/2$ , and  $x_A = 1/8$  represent the fractional occupation at cation and anion sites, respectively. The value  $T\Delta S_{\text{mix}} = -0.1$  eV/cation corresponds to  $T = 800$  K.

For  $B = \text{Sn}$  and  $\text{Ti}$ , the relative energies are lower than  $-0.2$  eV/cation. It implies that the stannates and the titanates have a strong tendency to prefer the ordered structures over the defect-fluorite up to high temperatures of ca. 2000 K. For  $B = \text{Zr}$  and  $\text{Hf}$ , the relative energies are in the range of  $-0.2$  to  $0.0$  eV/cation. It implies that the disordered defect-fluorite structure may be formed

in the zirconates and the hafnates at high temperatures, especially when the ionic radius of  $A^{3+}$  cation is small.

In the PDF analyses based on neutron total scattering for few  $A_2B_2O_7$  compounds,<sup>17,37</sup> a weberite-type structure model was successfully used to fit the data, indicating the formation of weberite-type structures as a short-range ordered state. However, the structure models include fractionally occupied cation and anion sites. On another front, several experimental studies have reported that an unknown “fluorite-like” phase was observed at low temperatures for the  $A_2B_2O_7$  compositions by XRD measurement.<sup>21,22,38</sup> Shlyakhtina et al.<sup>21,22</sup> reported that  $A_2Zr_2O_7$  ( $A = \text{Lu–Sm}$ ),  $A_2Hf_2O_7$  ( $A = \text{Lu–Eu}$ ), and  $A_2Ti_2O_7$  ( $A = \text{Lu–Tm}$ ) compounds synthesized by the freeze-dried method have the fluorite-like phase instead of the pyrochlore phase. The fluorite-like phases were suggested based on weak signals emerging in XRD. Interestingly, those composition ranges overlap the composition ranges where weberite is stable compared to pyrochlore and SQS in our calculations. Sevastyanov et al.<sup>38</sup> also reported that the powder with  $\text{Gd}_2\text{Hf}_2\text{O}_7$  composition calcined at 1273 K has a fluorite-like phase characterized by a broad peak at around  $2\theta = 20^\circ$  in XRD. We performed the XRD simulation for weberite and pyrochlore structures of the  $\text{Gd}_2\text{Hf}_2\text{O}_7$ : Simulated XRD patterns indicate that there are several peaks at around  $2\theta = 20^\circ$  in weberite, but there are no peaks in pyrochlore (see Figure 4.9). This suggests a possibility that the experimental broad peak in  $\text{Gd}_2\text{Hf}_2\text{O}_7$  was derived from the weberite-type structure.

It should be interesting to revisit  $A_2B_2O_7$  ( $A = \text{Lu}^{3+}\text{–La}^{3+}$ ,  $B = \text{Zr}^{4+}$ ,  $\text{Hf}^{4+}$ ,  $\text{Sn}^{4+}$ , and  $\text{Ti}^{4+}$ ) compounds taking the present computed results into consideration. Experimentally, they were reported to form either pyrochlore or defect-fluorite structures. According to the present study, the weberite-type ordering of the defect-fluorite structure is expected to take place in many of them especially by low-temperature synthesis or annealing. Together with detailed neutron diffraction and

XRD analyses, transmission electron microscopy (TEM) should be useful for direct observation of the ordered state of cations and anions in  $A_2B_2O_7$ .

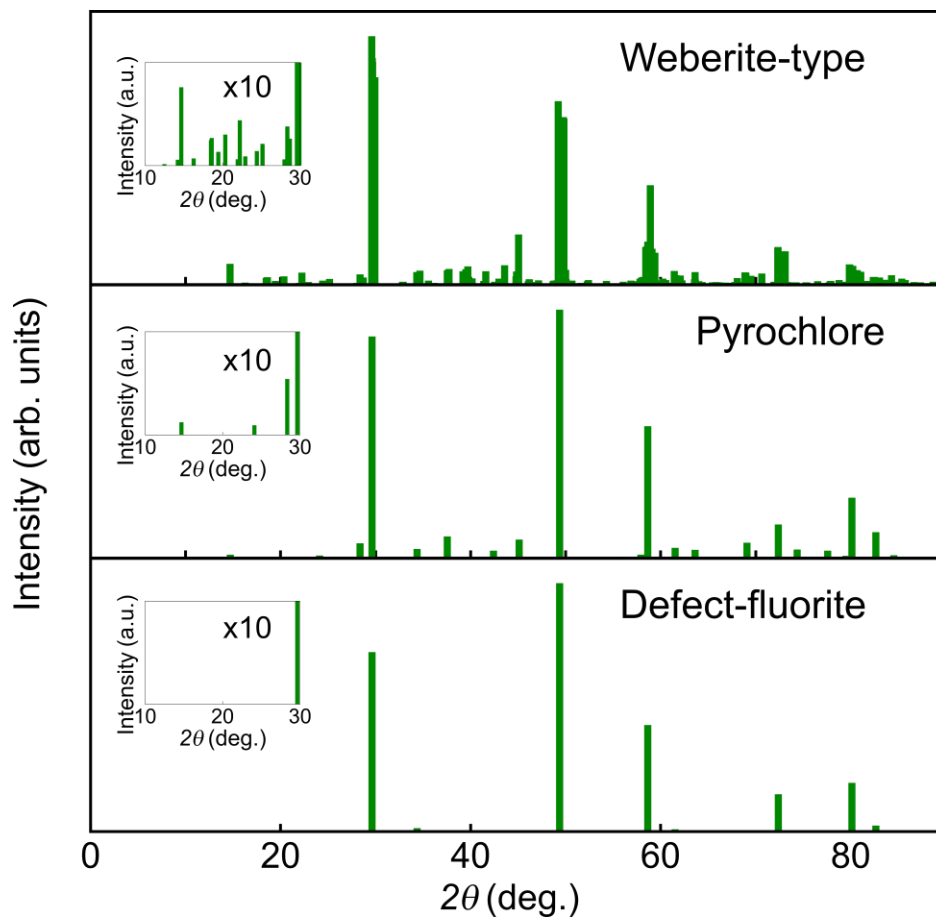


**Figure 4.9.** Simulated XRD patterns ( $=1.54 \text{ \AA}$ ) of (top) weberite-type, (middle) pyrochlore, and (bottom) ideal defect-fluorite structures of  $Gd_2Hf_2O_7$ . The intensity is calculated by multiplying the structural factor, the Lorentz factor of polycrystals, and the polarization factor. The low-scattering-angle part of the intensity data is expanded in the inset for each structure.

Finally, it is important to note a few limitations of the calculations in our study. First, the cell sizes for the exhaustive search were limited to up to 24 sublattice sites. Structural searches with larger cells may provide ordered structures with longer periodicity. Even when the cell size is smaller than ours, total energy may be affected by the calculation conditions such as exchange–correlation

functional. The previous structure search of  $\text{Ho}_2\text{Zr}_2\text{O}_7$  with cell size containing less than 12 sublattice cells provided different anion configuration.<sup>39</sup> We confirmed that energies of the structure model they proposed for such a small cell are higher than ones of the weberite-type model found here and pyrochlore structures for  $\text{Yb}_2\text{Zr}_2\text{O}_7$  and  $\text{Ho}_2\text{Zr}_2\text{O}_7$ . Second, SQS models on both the cation and anion sublattices were used to model the defect-fluorite structure. As shown in Figure 4.9, energies of five SQS models scatter by 0.2 eV/cation at most. Seko and Tanaka<sup>40</sup> reported that the convergence of SQS energies with respect to the cell size is quite slow in ionic multicomponent systems due to long-range interactions. To estimate the ordering temperature of the defect-fluorite structure, such correlations should be treated much more carefully. However, it is beyond the scope of the present study.

## 4.4 Conclusions

In the present work, we have performed first-principles calculations to search the ground-state structures of  $A_2B_2O_7$  ( $A = \text{Lu}^{3+}\text{--La}^{3+}$ ,  $B = \text{Zr}^{4+}$ ,  $\text{Hf}^{4+}$ ,  $\text{Sn}^{4+}$ , and  $\text{Ti}^{4+}$ ) by an exhaustive structure search for the specific composition  $\text{Yb}_2\text{Ti}_2\text{O}_7$ . The obtained results are summarized in the following four points:

- (1) In  $\text{Yb}_2\text{Ti}_2\text{O}_7$ , the lowest-energy structure is found to be the layered structure derived from *2OIII*-type weberite, and the second-lowest-energy structure is the pyrochlore structure.
- (2) Calculation of free energies including vibrational entropy contributions by first-principles phonon calculations indicates that the weberite-type structure becomes less stable than the pyrochlore at temperatures higher than 550 K.
- (3) In  $A_2\text{Zr}_2\text{O}_7$  and  $A_2\text{Hf}_2\text{O}_7$ , the weberite-type structure is preferred to the pyrochlore structure in a large range of  $A^{3+}$  ionic radii less than about 1.1 Å. In contrast, all  $A_2\text{Sn}_2\text{O}_7$  prefer pyrochlore, as is

consistent with numerous previous studies. For  $A_2Ti_2O_7$ , the weberite-type structure is stabilized against pyrochlore only for the cases with small  $A^{3+}$  ionic radii ( $A = Lu^{3+}-Er^{3+}$ ).

(4)  $A_2Zr_2O_7$  and  $A_2Hf_2O_7$  are preferred to form defect-fluorite at high temperatures when the ionic radius of  $A^{3+}$  cation is small,<sup>11,16,41-45</sup> whereas  $A_2Sn_2O_7$  and  $A_2Ti_2O_7$  have a strong tendency to prefer ordered structures over defect-fluorite.<sup>11,16,46,47</sup>

## 4.5 Acknowledgement

Reprinted with permission from Matsumoto, U; Ogawa, T; Kitaoka, S; Moriwake, H; and Tanaka. I, *J. Phys. Chem. C* **2020**, 124, 20555–20562. Copyright 2020 American Chemical Society.

## Appendix 4.A Lattice Parameters of Yb<sub>2</sub>Ti<sub>2</sub>O<sub>7</sub>

**Table 4.A1.** Lattice parameters of Yb<sub>2</sub>Ti<sub>2</sub>O<sub>7</sub>.

crystal structure		lattice constants (Å)			volume (Å <sup>3</sup> )	space group
		<i>a</i>	<i>b</i>	<i>c</i>		
pyrochlore	expt. <sup>a</sup>	10.0905			256.8	<i>Fd</i> $\bar{3}$ <i>m</i>
	calc.	9.965			247.4	<i>Fd</i> $\bar{3}$ <i>m</i>
weberite (22-atom)	calc.	6.016	6.100	7.103	245.6	<i>P</i> $\bar{1}$
		$\alpha = 89.66^\circ$	$\beta = 78.85^\circ$	$\gamma = 76.90^\circ$		
weberite (44-atom)	calc.	7.158	7.830	9.257	495.5	<i>P</i> 1
		$\alpha = 89.59^\circ$	$\beta = 78.85^\circ$	$\gamma = 76.93^\circ$		

<sup>a</sup> Shlyakhtina, A. V.; Sokolov, A. E.; Ul'yanov, V. A.; Trunov, V. A.; Boguslavskii, M. V.; Levchnk, A. V.; Shcherbakova, L. G. Neutron diffraction investigation of the evolution of the crystal structure of oxygen-conducting solid solutions (Yb<sub>1-x</sub>Ca<sub>x</sub>)<sub>2</sub>Ti<sub>2</sub>O<sub>7</sub> (*x* = 0, 0.05, 0.10). *Crystallogr. rep.* **2009**, *54*, 25–30.

## Appendix 4.B Positional Parameters of Yb<sub>2</sub>Ti<sub>2</sub>O<sub>7</sub>

**Table 4.A2.** Positional parameters in unit cell of weberite-type structure Yb<sub>2</sub>Ti<sub>2</sub>O<sub>7</sub> (space group *P1*,  $a = 7.158 \text{ \AA}$ ,  $b = 7.830 \text{ \AA}$ ,  $c = 9.257 \text{ \AA}$ ,  $\alpha = 89.592^\circ$ ,  $\beta = 78.849^\circ$ ,  $\gamma = 76.933^\circ$ ).

atom	fractional atomic coordinates		
	<i>x</i>	<i>y</i>	<i>z</i>
Yb1	0.116800	0.142812	0.894539
Yb2	0.104691	0.652730	0.397902
Yb3	0.617797	0.154091	0.893936
Yb4	0.615593	0.645000	0.391602
Yb5	0.384407	0.355001	0.608398
Yb6	0.382203	0.845909	0.106064
Yb7	0.895309	0.347271	0.602098
Yb8	0.883200	0.857188	0.105461
Ti1	0.491789	0.741912	0.759011
Ti2	0.508211	0.258088	0.240989
Ti3	0.989593	0.759442	0.742225
Ti4	0.010407	0.240558	0.257775
Ti5	0.275100	0.984040	0.525705
Ti6	0.221457	0.485953	0.025911
Ti7	0.778543	0.514047	0.974089
Ti8	0.724900	0.015960	0.474295
O1	0.747137	0.685674	0.810947
O2	0.757902	0.182883	0.307321
O3	0.333697	0.323173	0.862852
O4	0.326417	0.821837	0.363130
O5	0.172811	0.177708	0.662479
O6	0.163122	0.676096	0.164468
O7	0.836878	0.323904	0.835532
O8	0.827189	0.822292	0.337521
O9	0.673583	0.178163	0.636870
O10	0.666303	0.676827	0.137148
O11	0.242098	0.817117	0.692679
O12	0.252863	0.314326	0.189053
O13	0.904481	0.969165	0.881548
O14	0.906876	0.465040	0.379968
O15	0.449871	0.130308	0.435954
O16	0.408198	0.632571	0.929207
O17	0.981930	0.368186	0.063204
O18	0.938081	0.867901	0.571690
O19	0.580556	0.536011	0.619224
O20	0.575846	0.036011	0.120436
O21	0.424154	0.963989	0.879564
O22	0.419444	0.463989	0.380776
O23	0.061919	0.132099	0.428310
O24	0.018070	0.631814	0.936796
O25	0.591802	0.367429	0.070793
O26	0.550129	0.869692	0.564046
O27	0.093124	0.534960	0.620032
O28	0.095520	0.030835	0.118452

## Appendix 4.C Atomic Configurations of Pyrochlore and Weberite-type Structures

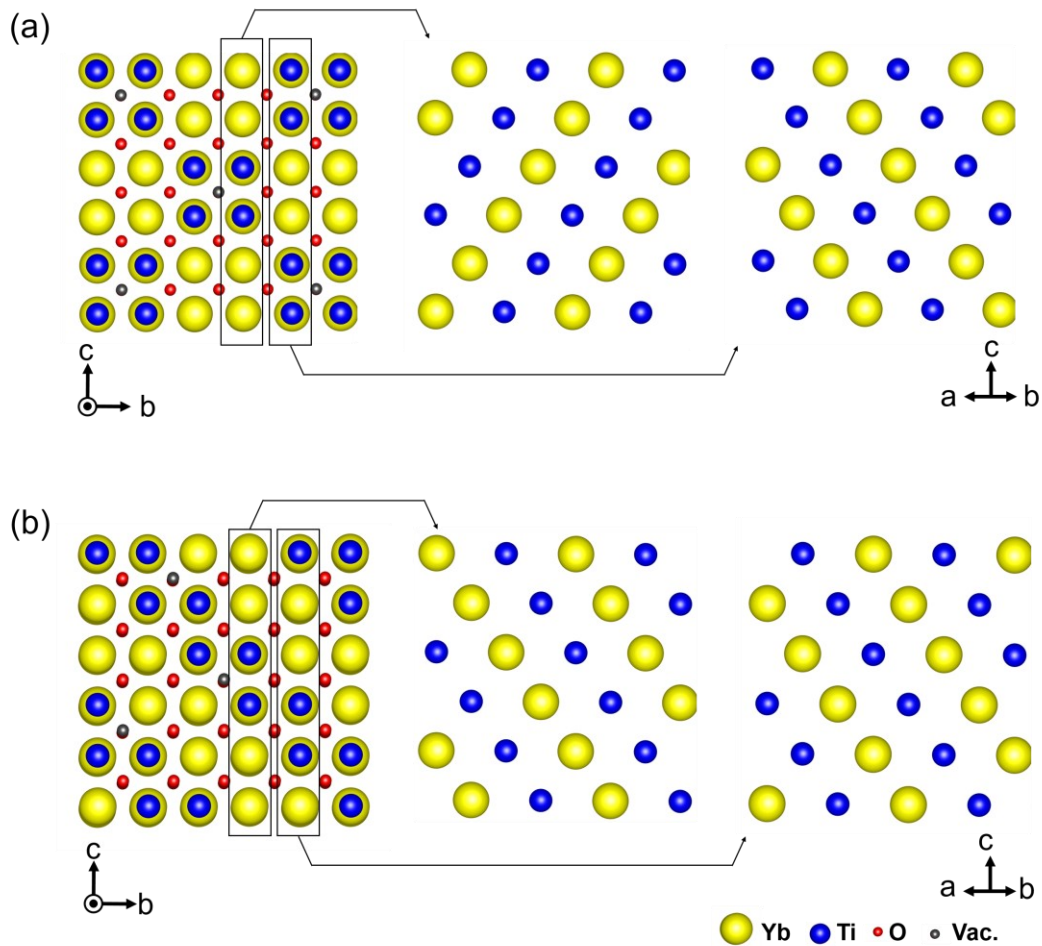


**Figure 4.A1.** Atomic configurations on the defect-fluorite lattices of (a) pyrochlore and (b) weberite-type structures as represented in axes of the defect-fluorite cell, where the left structures are viewed from  $[100]_{DF}$  and others are cation layers on the two neighboring  $(110)_{DF}$  planes extracted from the region indicated by the black rectangles. While, in both structures, the cation atoms aligns in the direction toward  $[1\bar{1}1]_{DF}$  on the  $(110)_{DF}$  planes, the stacking sequences in the  $[100]_{DF}$  directions are different to each other, resulting in the different type of long-range orders.

## Appendix 4.D Configurations of Cations in $\text{Yb}_3\text{TaO}_7$ and $\text{Yb}_2\text{Ti}_2\text{O}_7$

### Weberite-type Structures

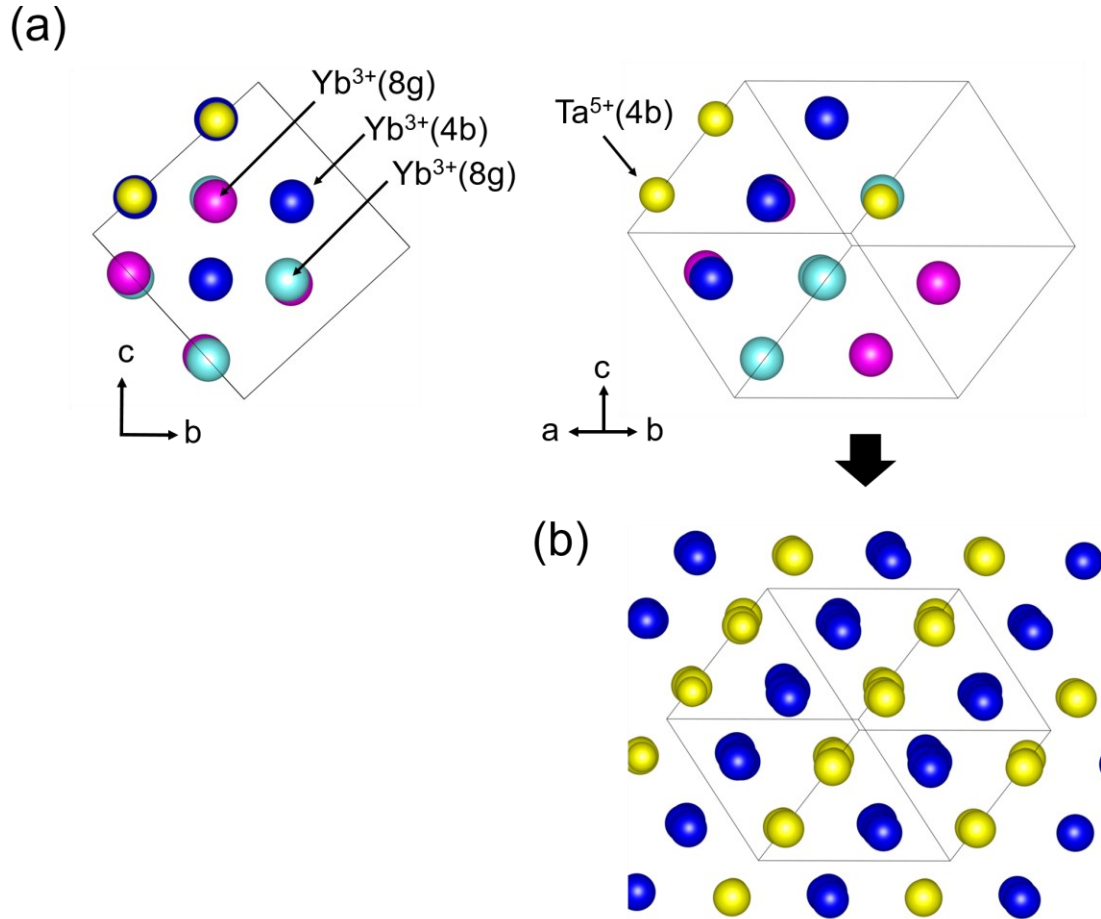


**Figure 4.A2.** (a) Configurations of cations in  $\text{Yb}_3\text{TaO}_7$  ( $2OIII$ -type weberite) as viewed from  $[100]_{\text{DF}}$  and  $[110]_{\text{DF}}$  directions in the axes of the defect-fluorite cells on the left and right panels, respectively, and (b) configurations of cations in the  $\text{Yb}_2\text{Ti}_2\text{O}_7$  weberite-type structure as viewed from the  $[110]_{\text{DF}}$  direction. Blue-, mint-, pink- and yellow- colored spheres represent  $\text{Yb}^{3+}(4b)$ ,  $\text{Yb}^{3+}(8g)$ ,  $\text{Yb}^{3+}(8g)$  and  $\text{Ta}^{5+}(4b)$ , respectively in the panel (a). In panel (b), blue- and yellow-colored spheres represent  $\text{Yb}^{3+}$  and  $\text{Ti}^{4+}$  atoms. The structure in panel (b) is produced by substituting pink- and mint-colored spheres on the  $8c$  sites by Yb and Ti atoms of  $\text{Yb}_2\text{Ti}_2\text{O}_7$ , respectively.

## Bibliography

- [1] Wuensch, B. J.; Eberman, K. W.; Heremans, C.; Ku, E. M.; Onnerud, P.; Yeo, E. M. E.; Haile, S. M.; Stalick, J. K.; Jorgensen, J. D. Connection Between Oxygen-Ion Conductivity of Pyrochlore Fuel-Cell Materials and Structural Change with Composition and Temperature. *Solid State Ionics* **2000**, *129*, 111–133.
- [2] Mandal, B. P.; Roy, M.; Grover, V.; Tyagi, A. K. X-ray Diffraction,  $\mu$ -Raman Spectroscopic Studies on  $\text{CeO}_2\text{-RE}_2\text{O}_3$  (RE = Ho, Er) Systems: Observation of Parasitic Phases. *J. Appl. Phys.* **2008**, *103*, 033506.
- [3] Pan, W.; Phillpot, S. R.; Wan, C.; Chernatynskiy, A.; Qu, Z. Low Thermal Conductivity Oxides. *MRS Bull.* **2012**, *37*, 917–922.
- [4] Tanaka, M.; Kitaoka, S.; Yoshida, M.; Sakurada, O.; Hasegawa, M.; Nishioka, K.; Kanagawa, Y. Structural Stabilization of EBC with Thermal Energy Reflection at High Temperatures. *J. Eur. Ceram. Soc.* **2017**, *37*, 4155–4161.
- [5] Asai, K.; Tanaka, M.; Ogawa, T.; Matsumoto, U.; Kawashima, N.; Kitaoka, S.; Izumi, F.; Yoshida, M.; Sakurada, O. Crystal Structural, Thermal, and Mechanical Properties of  $\text{Yb}_{2+x}\text{Ti}_{2-x}\text{O}_{7-x/2}$  Solid Solutions. *J. Solid State Chem.* **2020**, *287*, 121328.
- [6] Sickafus, K. E.; Minervini, L.; Grimes, R. W.; Valdez, J. A.; Ishimaru, M.; Li, F.; McClellan, J.; Hartmann, T. Radiation Tolerance of Complex Oxides. *Science* **2000**, *289*, 748–751.
- [7] Pilania, G.; Whittle, K. R.; Jiang, C.; Grimes, R. W.; Stanek, C. R.; Sickafus, K. E.; Pedro Uberuaga, B. Using Machine Learning to Identify Factors That Govern Amorphization of Irradiated Pyrochlores. *Chem. Mater.* **2017**, *29*, 2574–2583.
- [8] Abe, R.; Higashi, M.; Zou, Z.; Sayama, K.; Abe, Y.; Arakawa, H. Photocatalytic Water Splitting into  $\text{H}_2$  and  $\text{O}_2$  over  $\text{R}_3\text{TaO}_7$  and  $\text{R}_3\text{NbO}_7$  (R = Y, Yb, Gd, La): Effect of Crystal Structure on Photocatalytic Activity. *J. Phys. Chem. B* **2004**, *108*, 811–814.
- [9] Abe, R.; Higashi, M.; Zou, Z.; Sayama, K.; Abe, Y.; Arakawa, H. Photocatalytic Activity of  $\text{R}_3\text{MO}_7$  and  $\text{R}_2\text{Ti}_2\text{O}_7$  (R = Y, Gd, La; M = Nb, Ta) for Water Splitting into  $\text{H}_2$  and  $\text{O}_2$ . *J. Phys. Chem. B* **2006**, *110*, 2219–2226.

- [10] Mamontov, E; Egami, T.; Brezny, R.; Koranne, M.; Tyagi, S. Lattice Defects and Oxygen Storage Capacity of Nanocrystalline Ceria and Ceria-Zirconia. *J. Phys. Chem. B* **2000**, *104*, 11110–11116.
- [11] Subramanian, M. A.; Aravamudan, G.; Subba Rao, G. V. Oxide Pyrochlores — A Review. *Prog. Solid State Chem.* **1983**, *15*, 55–143.
- [12] Minervini, L.; Grimes, R. W. Disorder in Pyrochlore Oxides, *J. Am. Ceram. Soc.* **2000**, *83*, 1873–1878.
- [13] Stanek, C. R.; Grimes, R. W. Prediction of Rare-Earth  $A_2Hf_2O_7$  Pyrochlore Phases. *J. Am. Ceram. Soc.* **2002**, *85*, 2139–2141.
- [14] Li, Y.; Kowalski, P. M.; Beridze, G.; Birnie, A. R.; Finkeldei, S.; Bosbach, D. Defect Formation Energies in  $A_2B_2O_7$  Pyrochlores. *Scr. Mater.* **2015**, *107*, 18–21.
- [15] Zu, X. T.; Li, N.; Gao, F. First-Principles Study of Structural and Energetic Properties of  $A_2Hf_2O_7$  ( $A = Dy, Ho, Er$ ) Compounds. *J. Appl. Phys.* **2008**, *104*, 043517.
- [16] Jiang, C.; Stanek, C. R.; Sickafus, K. E.; Uberuaga, B. P. First-Principles Prediction of Disorder Tendencies in Pyrochlore Oxides, *Phys. Rev. B* **2009**, *79*, 104203.
- [17] Shamblin, J.; Feygenson, M.; Neufeind, J.; Tracy, C. L.; Zhang, F.; Finkeldei, S.; Bosbach, D.; Zhou, H.; Ewing, R. C.; Lang, M. Probing Disorder in Isometric Pyrochlore and Related Complex Oxides. *Nat. Mater.* **2016**, *15*, 507–511.
- [18] Cai L.; Nino, J. C. Complex Ceramic Structures. I. Weberites. *Acta. Crystallogr., Select. B* **2009**, *65*, 269–290.
- [19] King, G.; Thompson, C. M.; Greedan, J. E.; Llobet, A. Local Structure of the Vacancy Disordered Fluorite  $Yb_3TaO_7$  from Neutron Total Scattering. *J. Mater. Chem. A* **2013**, *1*, 10487–10494.
- [20] Shlyakhtina, A. V.; Shcherbakova, L. G. Polymorphism and High-Temperature Conductivity of  $Ln_2M_2O_7$  ( $Ln = Sm-Lu$ ;  $M = Ti, Zr, Hf$ ) Pyrochlore. *Solid State Ionics*, **2011**, *192*, 200–204.
- [21] Shlyakhtina, A. V.; Shcherbakova, L. G.; Knotko, A. V.; Steblevskii, A. V. Study of the Fluorite–Pyrochlore–Fluorite Phase Transitions in  $Ln_2Ti_2O_7$  ( $Ln = Lu, Yb, Tm$ ). *J. Solid State Electrochem.* **2004**, *8*, 661–667.

- [22] Shlyakhtina, A. V.; Shcherbakova, L. G. New Solid Electrolytes of the Pyrochlore Family. *Russ. J. Electrochem.* **2012**, *48*, 1–25.
- [23] van de Walle, A.; Ceder, G. Automating First-Principles Phase Diagram Calculations. *J. Phase Equilib.* **2002**, *23*, 348–358.
- [24] Blöchl, P. E. Projector Augmented-Wave Method. *Phys. Rev. B* **1994**, *50*, 17953–17979.
- [25] Kresse, G.; Hafner, J. *Ab initio* Molecular Dynamics for Liquid Metals. *Phys. Rev. B* **1993**, *47*, 558–561.
- [26] Kresse, G.; Furthmüller, J. Efficient Iterative Schemes for *Ab initio* Total-Energy Calculations Using a Plane-Wave Basis Set. *Phys. Rev. B* **1996**, *54*, 11169–11186.
- [27] Perdew, J. P.; Burke, K.; Ernzerhof, M. Generalized Gradient Approximation Made Simple. *Phys. Rev. Lett.* **1996**, *77*, 3865–3868.
- [28] Perdew, J. P.; Burke, K.; Ernzerhof, M. Generalized Gradient Approximation Made Simple. *Phys. Rev. Lett.* **1997**, *78*, 1396–1396.
- [29] Monkhorst, H. J.; Pack, J. D. Special Points for Brillouin-Zone Integrations. *Phys. Rev. B* **1976**, *13*, 5188–5192.
- [30] Parlinski, K.; Li, Z. Q.; Kawazoe, Y. First-Principles Determination of the Soft Mode in Cubic  $\text{ZrO}_2$ . *Phys. Rev. Lett.* **1997**, *78*, 4063–4066.
- [31] Togo, A.; Oba, F.; Tanaka, I. First-Principles Calculations of the Ferroelastic Transition Between Rutile-Type and  $\text{CaCl}_2$ -Type  $\text{SiO}_2$  at High Pressures. *Phys. Rev. B* **2008**, *78*, 134106.
- [32] Togo, A.; Tanaka, I. First Principles Phonon Calculations in Materials Science. *Scr. Mater.* **2015**, *108*, 1–5.
- [33] Zunger, A.; Wei, S. H.; Ferreira, L. G.; Bernard, J. E. Special Quasirandom Structures. *Phys. Rev. Lett.* **1990**, *65*, 353–356.
- [34] van de Walle, A.; Tiwary, P.; de Jong, M. M.; Olmsted, D. L.; Asta, M. D.; Dick, A.; Shin, D.; Wang, Y.; Chen, L.-Q.; Liu, Z.-K. Efficient Stochastic Generation of Special Quasirandom Structures. *CALPHAD*. **2013**, *42*, 13–18.

- [35] O'Quinn, E. C.; Bishop, J. L.; Sherrod, R.; Neufeind, J.; Montemayor, S. M.; Fuentes, A. F.; Lang, M. Advanced Characterization Technique for Mechanochemically Synthesized Materials: Neutron Total Scattering Analysis. *J. Mater. Sci.* **2018**, *43*, 13400–13410.
- [36] Shannon, R. D. Revised Effective Ionic Radii and Systematic Studies of Interatomic Distances in Halides and Chalcogenides. *Acta Crystallogr., Sect. A* **1976**, *32*, 751–767.
- [37] Shamblin, J.; Tracy, C. L.; Palomares, R. I.; O'Quinn, E. C.; Ewing, R. C.; Neufeind, J.; Feygenson, M.; Behrens, J.; Trautmann, C.; Lang, M. Similar Local Order in Disordered Fluorite and Aperiodic Pyrochlore Structures. *Acta Mater.* **2018**, *144*, 60–67.
- [38] Sevastyanov, V. G.; Simonenko, E. P.; Simonenko, N. P.; Stolyarova, V. L.; Lopatin, S. I.; Kuznetsov, N. T. Synthesis, Vaporization and Thermodynamic Properties of Superfine  $\text{Nd}_2\text{Hf}_2\text{O}_7$  and  $\text{Gd}_2\text{Hf}_2\text{O}_7$ . *Eur. J. Inorg. Chem.* **2013**, *26*, 4636–4644.
- [39] Solomon, J. M.; Shamblin, J.; Maik, L.; Narvrotsky, A.; Asta, M. Chemical Ordering in Substituted Fluorite Oxides: A Computational Investigation of  $\text{Ho}_2\text{Zr}_2\text{O}_7$  and  $\text{RE}_2\text{Th}_2\text{O}_7$  (RE = Ho, Y, Gd, Nd, La). *Sci. Rep.* **2016**, *6*, 38772.
- [40] Seko, A.; Tanaka, I. Special Quasirandom Structure in Heterovalent Ionic Systems. *Phys. Rev. B* **2015**, *91*, 024106.
- [41] Popov, V. V.; Menushenkov, A. P.; Yaroslavtsev, A. A.; Zubavichus, Y. V.; Gaynanov, B. R.; Yastrebtshev, A. A.; Leshchev, D. S.; Chernikov, R. V. Fluorite-Pyrochlore Phase Transition in Nanostructured  $\text{Ln}_2\text{Hf}_2\text{O}_7$  (Ln = La-Lu). *J. Alloys Compd.* **2016**, *689*, 669–679.
- [42] Mandal, B. P.; Garg, N.; Sharma, S. M.; Tyagi, A. K. Preparation, XRD and Raman Spectroscopic Studies on New Compounds  $\text{RE}_2\text{Hf}_2\text{O}_7$ . (RE = Dy, Ho, Er, Tm, Lu, Y): Pyrochlores or Defect-Fluorite? *J. Solid State Chem.* **2006**, *179*, 1990–1994.
- [43] Andrievskaya, E. R. Phase Equilibria in the Refractory Oxide Systems of Zirconia, Hafnia and Yttria with Rare-Earth Oxides. *J. Eur. Ceram. Soc.* **2008**, *28*, 2363–2388.
- [44] Karthik, C.; Anderson, T. J.; Gout, D.; Ubic, R. Transmission Electron Microscopic Study of Pyrochlore to Defect-Fluorite Transition in Rare-Earth Pyrohafnates. *J. Solid State Chem.* **2012**, *194*, 168–172.

- [45] Klee, W. K.; Weitz, G. Infrared Spectra of Ordered and Disordered Pyrochlore-Type Compounds in the Series  $\text{RE}_2\text{Ti}_2\text{O}_7$ ,  $\text{RE}_2\text{Zr}_2\text{O}_7$  and  $\text{RE}_2\text{Hf}_2\text{O}_7$ . *J. Inorg. Nucl. Chem.* **1969**, *31*, 2369–2372.
- [46] Kennedy, B. J.; Hunter, B. A.; Howard, C. J. Structural and Bonding Trends in Tin Pyrochlore Oxides. *J. Solid State Chem.* **1997**, *130*, 58–65.
- [47] Brisse, F.; Knop, O. Pyrochlores. III. X-Ray, Neutron, Infrared, and Dielectric Studies of  $\text{A}_2\text{Sn}_2\text{O}_7$  Stannates. *Can. J. Chem.* **1968**, *46*, 859–873.

## Chapter 5

### Oxide-Ion Diffusion in Weberite-type and Pyrochlore Structures

#### $\text{Yb}_2\text{Ti}_2\text{O}_7$ : A First-principles Molecular Dynamics Simulations

##### 5.1 Introduction

Yttrium stabilized zirconia (YSZ), have been commercially used as electrolytes in SOFC over the past decades, but there remains a problem that the operating temperature is high. Thus, the other suitable materials for electrolytes in SOFC, which exhibits high ionic conductivity at low temperatures, is highly demanded, which strongly motivates us to explore new oxide-ion conductors. To date, an abundant of studies on pyrochlore-related oxides, apart from YSZ, have been reported in the literature. For example, Shlyakhtina et al. reported systematical studies on pyrochlore and defect-fluorite oxides with  $A_2B_2O_7$  composition and found the pyrochlore with  $\text{Yb}_2\text{Ti}_2\text{O}_7$  composition exhibit higher oxide conductivity compared to other compositions.<sup>1</sup> Tuller et al. reported that doping with aliovalent or aliovalent cations lower the activation energy of ion transport and enhances the ionic conductivity by an order magnitude.<sup>2,3</sup> These studies demonstrate that oxide-ion conductivity of pyrochlore-related oxides can be tuned by controlling ionic radius ratio of  $A$  and  $B$  cations or incorporating a variety of cations with variable oxidation states.

Recently, experimental studies based on neutron pair distribution function (PDF) analysis have revealed that the weberite-type structures are locally formed in the  $\text{Ho}_2\text{Zr}_2\text{O}_7$  oxide, which has been identified as a long-range disordered phase by X-ray diffraction (XRD) analysis.<sup>4</sup> Similarly, O'Quinn et al. reported that crystalline phase fraction of  $\text{Er}_2\text{Ti}_2\text{O}_7$  synthesized by mechanical milling technique changes from weberite to pyrochlore structures with increasing temperature.<sup>5,6</sup> In the previous study

based on theoretical calculations, we have reported a weberite-type structure found by performing a configurational search with up to 22-atom cell and the weberite-type structure can be stabilized in low temperature.<sup>7</sup> A series of studies demonstrates a possibility of pyrochlore-related oxides is used as an oxide-ion conductor. However, a majority of studies on pyrochlore-related oxides were focused on to improve the performance has focused on ordered pyrochlore and disordered defect-fluorite phases. The diffusion property of weberite-type structure remains unknown.

Herein, we report oxide-ion diffusion in pyrochlore and weberite-type structures with the composition  $\text{Yb}_2\text{Ti}_2\text{O}_7$  using first-principles molecular dynamics (FPMD) simulations. The pyrochlore structure has an isotropic oxide-ion diffusion pathway, whereas the weberite-type structure has two-dimensional on the Ti-O layer. Moreover, results show the self-diffusion coefficient of weberite-type structure is higher than that of pyrochlore structure by one order of magnitude.

## 5.2 Computational Methods

Weberite-type atomic configurations for  $\text{Yb}_2\text{Ti}_2\text{O}_7$  within 12 cation and 24 anion sites were generated by the Alloy Theoretic Automated Toolkit (ATAT).<sup>8</sup> The number of configurations was 3850. Here, the weberite-type derivative structures consist of a face-centered cubic (fcc) array of cations and a simple cubic lattice array of anions.

All first-principles calculations within the framework of density functional theory (DFT) were carried out using the projector augmented wave (PAW) method,<sup>9</sup> as incorporated in the Vienna Ab initio Simulation Package (VASP).<sup>10,11</sup> The 2s and 2p orbitals for O atoms, 3d and 4s orbitals for Ti atoms, 4s, 4p, 4d, and 5s orbitals for Yb atoms, 3s and 3p orbitals for Al atoms were explicitly treated as valence states. Generalized gradient approximation (GGA) functional with Perdew–Burke–Ernzerhof parametrization adapted for solids<sup>12</sup> (PBEsol) was used to treat exchange–correlation effect.

Brillouin zones (BZs) were integrated with  $k$ -point spacings of less than  $0.5 \text{ \AA}^{-1}$  and a Gaussian smearing approach with a smearing width of 0.01 eV.

For the configuration search in the  $\text{Yb}_2\text{Ti}_2\text{O}_7$  weberite-type structures, the cut-off energy for the planewave basis sets was set as 370 eV. Atomic positions were fully optimized until the residual forces became less than  $0.02 \text{ eV/\AA}$ , with the lattice constant fixed to that of the ideal pyrochlore structure.

For FPMD simulations, the velocity–Verlet algorithm was used to integrate the equations of motion with a time step of 3 fs. A total of 18,000 time steps (540 ps) were calculated in the  $NVT$  ensemble with a Nosé–Hoover thermostat<sup>13,14</sup> at temperatures 2000, 2200, 2400, and 2600 K. In these simulations, an oxide-ion vacancy was introduced by removing a single oxygen atom and two electrons from the simulation cell with charge compensation by addition of a homogeneous jellium background charge. The cut-off energy was 300 eV. Since GGA functional is known to misalign the metal’s 3d states, an on-site Coulomb correction,  $U_{\text{eff}}$ , was applied to Ti 3d electrons, where the value of  $U_{\text{eff}}$  was set at 5.5 eV within the rotationally invariant formalism.<sup>15</sup> This value of  $U_{\text{eff}}$  was calculated based on the liner response method developed by Cococcioni et al.<sup>16</sup> Here, we used more stringent energy convergence criterion than that used for FPMD simulations; the cut-off energy for the planewave basis sets was 550 eV and BZs were integrated with  $k$ -point spacings of less than  $0.16 \text{ \AA}^{-1}$ .

To investigate oxide-ion conduction in the pyrochlore and weberite-type structures, the mean square displacements (MSDs) of the ionic positions were calculated via the following equation:

$$\text{MSD}(\tau) = \frac{1}{N_\alpha N_\omega} \sum_{i=0}^{N_\alpha-1} \sum_{j=0}^{N_\omega-1} |r_{\alpha_i}(\tau + t_0; \omega_j) - r_{\alpha_i}(t_0; \omega_j)|^2 \quad (1)$$

$$\approx \frac{1}{N_\alpha N_\omega} \sum_{i=0}^{N_\alpha-1} \sum_{j=0}^{N_\omega-1} |r_{\alpha_i}(\tau + t_j; \omega_0) - r_{\alpha_i}(t_j; \omega_0)|^2,$$

where,  $N_\alpha$ ,  $N_\omega$ ,  $r_{\alpha_i}(t)$ ,  $\omega_j$  represent the total number of species  $\alpha$ , the number of sampling, the  $i$ th ion position of species  $\alpha$  at time  $t$ , and the initial parameter of the process noise. In our approximate, the number of the process noise can be regarded as the number of trajectories. The self-diffusion coefficient,  $D_\alpha$ , of each species,  $\alpha$ , have been calculated from the Einstein relation via the slopes of MSDs:

$$D_\alpha = \frac{1}{2d} \lim_{t \rightarrow \infty} \frac{d\text{MSD}(t)}{dt}, \quad (2)$$

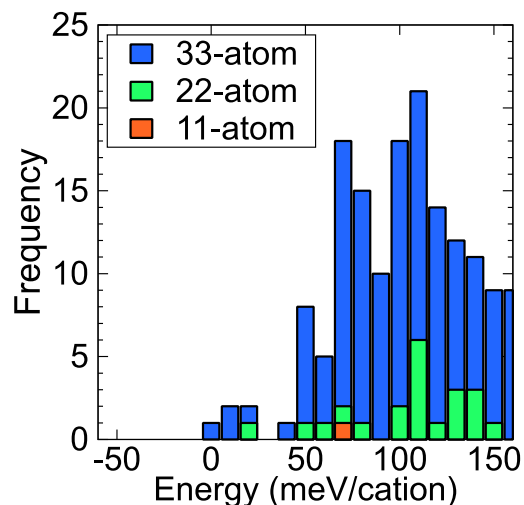
where,  $d$  is the dimension of the lattice on with ion hopping takes places.

### 5.3 Results and Discussion

To investigate candidate weberite-type structures, we performed configurational searching with maximum 33-atom cell based on weberite-type cation ordering configurations. The distribution of calculated energies of weberite-type structures with respect to the lowest energy structure are shown in Figure 5.1. Four structures with 33-atom cell are found to have lower energy than that of the weberite-type structure with 22-atom cell. These structures have the coordination number of Ti are from five to seven, whereas the coordination number of Yb are from seven to eight. The energy difference between the lowest energy structure and pyrochlore structure is 67 meV/cation. Anion configurations of four structures are similar, suggesting that the anion defects are inclined to be formed in weberite-type structure rather than pyrochlore structure.

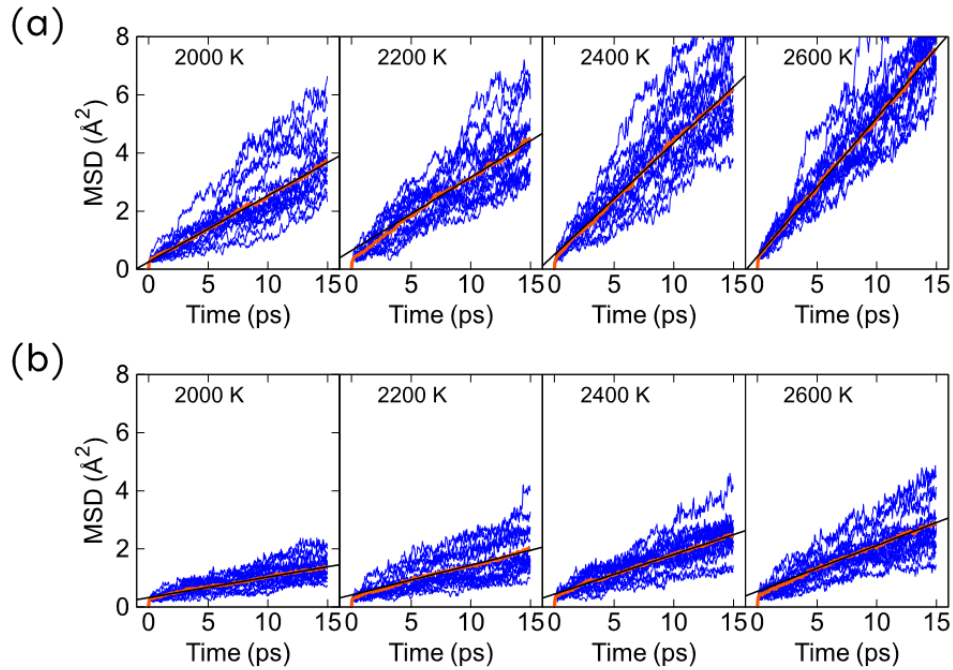
To examine the oxide-ion diffusion, we performed FPMD simulation of weberite-type and pyrochlore structures at the temperature of 2000, 2200, 2400, and 2600 K. For simulation box, we used the conventional cubic 88-atom and 132-atom cells of the pyrochlore and weberite-type

structures, respectively. Here, the 132-atom cell is expanded by the third-lowest energy structure obtained from the configuration searching because the computational cost can be lowered owing to its cubic structure.



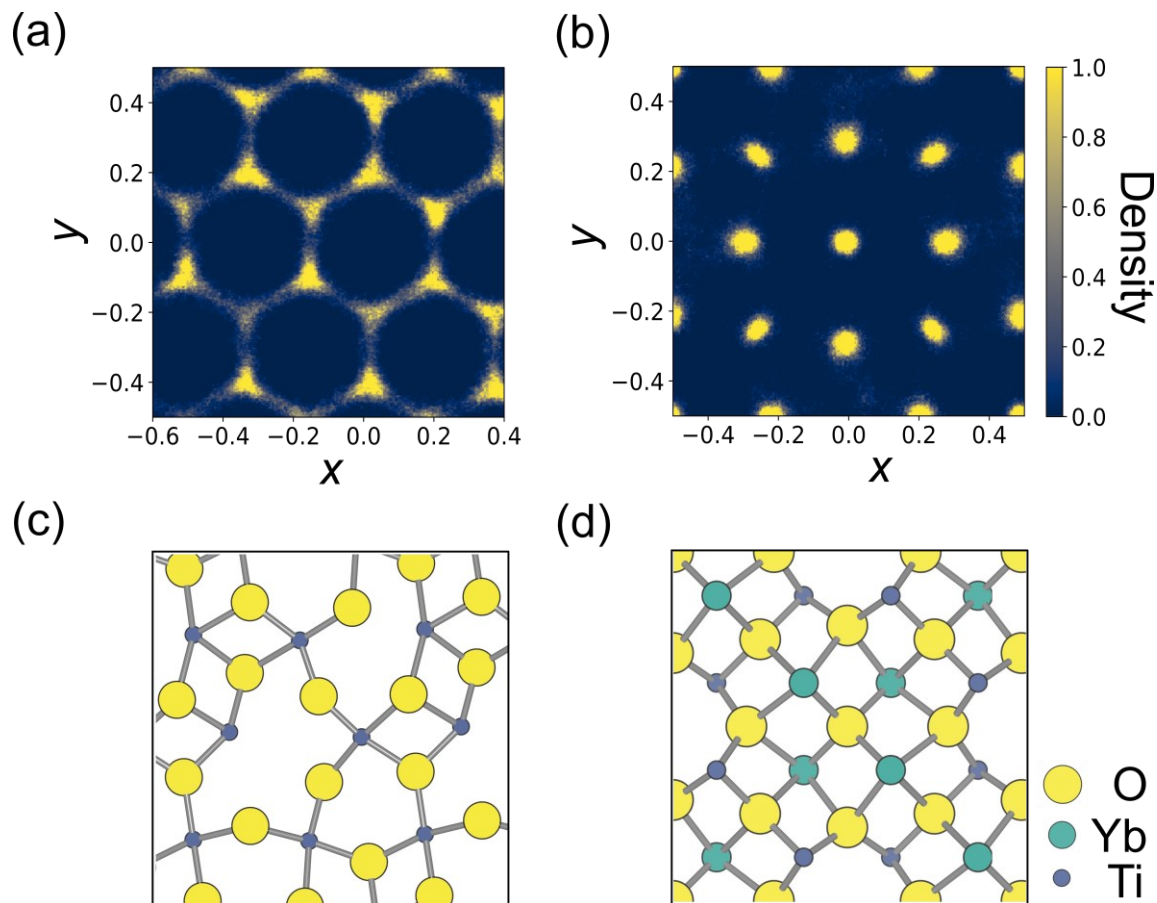
**Figure 5.1.** Histogram of Yb<sub>2</sub>Ti<sub>2</sub>O<sub>7</sub> energies exhaustively calculated, measured from the lowest energy.

Figure 5.2a,b shows MSDs of weberite-type and pyrochlore structures, respectively. With increasing the temperature from 2000 K to 2600K, MSD values are greater at each structure. Also, the distribution of MSDs is more scatter at higher temperature. Comparing with MSDs of both structures, MSDs of weberite-type structure are greater than that of pyrochlore at each temperature. The averaged MSDs (the orange lines) exhibit parabolic increase in the range of 0 to 1 ps and then increases as a fashion of linear range of 1 ps to 15 ps. Therefore, we are confident that MSDs are adequate to sample to calculate diffusion coefficient from MSDs. The gradients of MSD are greater at higher temperature.



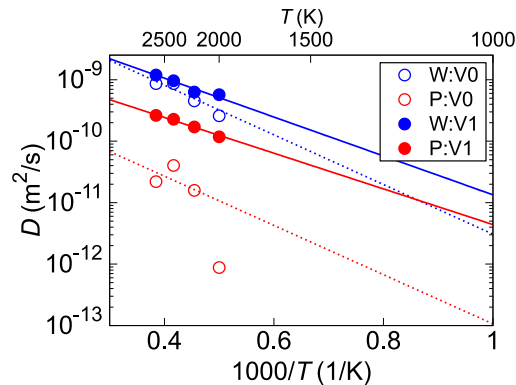
**Figure 5.2.** Mean square displacement of (a) weberite-type and (b) pyrochlore structures.

Figure 5.3a,b shows that oxide-ion density map on Ti–O planes in weberite-type structure and  $\langle 100 \rangle_{DF}$  planes of pyrochlore structure, respectively. At 2000 K, the oxide ions in the pyrochlore structure are confined to local vibrations around their lattice positions. The oxide-ion densities on the moiety of  $48f-8a$  sites are slightly high parallel to  $\{100\}$  direction, resulting in the oxide ions occasionally jump between  $48f$  sites and vacant  $8a$  sites. In contrast, the trajectories of oxide ions in the weberite-type structure are overlapped on Ti–O planes, which means the oxide ions significantly jump onto the unoccupied neighbor sites, resulting that the high oxide-ion diffusion occurs. Furthermore, in the weberite-type structure an analysis of our simulation results indicates that the oxide-ion densities are high on Ti-centered honeycomb shape.



**Figure 5.3.** Oxide-ion densities of (a) weberite-type and (b) pyrochlore structures and corresponding optimized structures of weberite-type and pyrochlore structures (d).

To quantify the oxide-ion diffusion, we calculated oxide-ion diffusion coefficients from MSDs of weberite-type and pyrochlore structures. The resulting oxide-ion diffusion coefficients are plotted in Figure 5.4. The oxide-ion diffusion coefficients increased linearly as the temperature increased in each structure. In comparison with oxide-ion diffusion coefficients of both structures, the oxide-ion diffusion coefficient of the weberite-type structure is higher than that of the pyrochlore structure in any temperature. This means that the weberite-type structure can be an oxide-ion conductor rather than the pyrochlore structure.



**Figure 5.4.** Temperature dependence of oxide-ion diffusion coefficients of weberite-type (blue) and pyrochlore structures (red). V0 and V1 mean no and one oxygen vacancies introduced in the simulation cells.

## 5.4 Conclusions

First-principles molecular dynamics simulations were carried out to investigate oxide-ion diffusion in the waberite and pyrochlore structures of the  $\text{Yb}_2\text{Ti}_2\text{O}_7$  composition. The mean square displacements were calculated from the calculation results for each structure and the diffusion coefficients were compared. The diffusion coefficient of the weberite-type structure was found to be about one order of magnitude larger than that of the Pyrochlore structure. The density of oxide ions was also plotted to investigate the details of the diffusion path. In the pyrochlore structure, the oxide ion density was found to be on the line connecting adjacent anion sites in the simple lattice. This suggests that the oxide ions diffuse in a three-dimensional manner. On the other hand, in the waberite structure, the oxide ion density was found only in the Ti–O layer. In the waberite structure, the density of oxide ions was observed only in the Ti–O layer, and the density formed a honeycomb shape with

the Ti cation at the center. Therefore, in the waberite structure, the oxide ions diffuse over the honeycomb shape in a two-dimensional manner.

## Bibliography

- [1] Shlyakhtina, A. V.; Shcherbakova, L. G. Polymorphism and High-Temperature Conductivity of  $Ln_2M_2O_7$  ( $Ln = \text{Sm-Lu}$ ;  $M = \text{Ti, Zr, Hf}$ ) Pyrochlores. *Solid State Ionics* **2011**, *192* (1), 200–204.
- [2] Kramer, S. A.; Tuller, H. L. A Novel Titanate-Based Oxygen Ion Conductor:  $\text{Gd}_2\text{Ti}_2\text{O}_7$ . *Solid State Ionics* **1995**, *82* (1–2), 15–23.
- [3] Tuller, H. L.; Moon, P. K. Fast Ion Conductors: Future Trends. *Mater. Sci. Eng. B* **1988**, *1* (2), 171–191.
- [4] Shamblin, J.; Feygenson, M.; Neuefeind, J.; Tracy, C. L.; Zhang, F.; Finkeldei, S.; Bosbach, D.; Zhou, H.; Ewing, R. C.; Lang, M. Probing Disorder in Isometric Pyrochlore and Related Complex Oxides. *Nat. Mater.* **2016**, *15* (5), 507–511.
- [5] O'Quinn, E. C.; Sickafus, K. E.; Ewing, R. C.; Baldinozzi, G.; Neuefeind, J. C.; Tucker, M. G.; Fuentes, A. F.; Drey, D.; Lang, M. K. Predicting Short-Range Order and Correlated Phenomena in Disordered Crystalline Materials. *Sci. Adv.* **2020**, *6* (35), eabc2758.
- [6] Drey, D. L.; O'Quinn, E. C.; Subramani, T.; Lilova, K.; Baldinozzi, G.; Gussev, I. M.; Fuentes, A. F.; Neuefeind, J. C.; Everett, M.; Sprouster, D.; Navrotsky, A.; Ewing, R. C.; Lang, M. Disorder in  $\text{Ho}_2\text{Ti}_{2-x}\text{Zr}_x\text{O}_7$ : Pyrochlore to Defect Fluorite Solid Solution Series. *RSC Adv.* **2020**, *10* (57), 34632–34650.
- [7] Details are described in Chapter 4.
- [8] van de Walle, A.; Ceder, G. Automating First-Principles Phase Diagram Calculations. *J. Phase Equilibria* **2002**, *23* (4), 348–359.
- [9] Blöchl, P. E. Projector Augmented-Wave Method. *Phys. Rev. B* **1994**, *50* (24), 17953–17979.
- [10] Kresse, G.; Furthmüller, J. Efficient Iterative Schemes for Ab Initio Total-Energy Calculations Using a Plane-Wave Basis Set. *Phys. Rev. B* **1996**, *54* (16), 11169–11186.
- [11] Kresse, G.; Hafner, J. Ab Initio Molecular Dynamics for Liquid Metals. *Phys. Rev. B* **1993**, *47* (1), 558–561.
- [12] Perdew, J. P.; Burke, K.; Ernzerhof, M. Generalized Gradient Approximation Made Simple. *Phys. Rev. Lett.* **1997**, *77* (18), 3865–3868.
- [13] Nosé, S. A Unified Formulation of the Constant Temperature Molecular Dynamics Methods. *J. Chem. Phys.* **1984**, *81* (1), 511–519.
- [14] William, G. H. Canonical Dynamics: Equilibrium Phase-Space Distributions. *Phys. Rev. A* **1985**, *31* (4), 1695–1697.

- [15] Dudarev, S.; Botton, G. Electron-Energy-Loss Spectra and the Structural Stability of Nickel Oxide: An LSDA+U Study. *Phys. Rev. B* **1998**, *57* (3), 1505–1509.
- [16] Cococcioni, M.; De Gironcoli, S. Linear Response Approach to the Calculation of the Effective Interaction Parameters in the LDA+U Method. *Phys. Rev. B* **2005**, *71* (3), 035105.

## Chapter 6

### General Conclusion

In this doctoral thesis, the author studied the defects, oxide-ion diffusion, and phase stability of pyrochlore-related oxides using first-principles calculations and magic-angle spinning nuclear magnetic resonance (MAS-NMR) experiments. The main results of this thesis are summarized as follows.

In Chapter 2, the chemical environments in Al-doped  $Y_2Ti_2O_7$ ,  $\alpha-Al_2O_3$ , and  $Y_3Al_5O_{12}$  compounds were investigated using  $^{27}Al$  magic-angle MAS-NMR experiments and first-principles calculations. The MAS-NMR spectra of the  $Y_2Ti_2O_7:Al$  sample showed three signals in the  $Y_2Ti_2O_7:Al$  sample. The good agreement between the major signal in the MAS-NMR spectra and the simulated signal of  $Al'_{Ti}$  based on NMR parameters derived from first-principles calculations corroborated that the dopant Al predominantly substituted onto Ti sites. This finding demonstrated the utility of combining NMR experiments and first-principles calculations to determine the chemical environments of defects in oxides. Comparison with the spectra of the  $Y_2Ti_2O_7:Al$  sample and its end members showed that the  $Y_2Ti_2O_7:Al$  sample contains a small amount of  $\alpha-Al_2O_3$ . Moreover, the thermodynamic stability of defects in pyrochlore  $Y_2Ti_2O_7:Al$  were examined using first-principles calculations. Those calculations showed that the  $Al'_{Ti}$  defect preferentially associated with the oxygen vacancy at temperatures lower than 500 K, whereas at higher temperatures the  $Al'_{Ti}$  defect and oxygen vacancy were preferentially isolated. This result is consistent with the fact that no five-coordinated aluminum was detected in the  $Y_2Ti_2O_7:Al$  sample in MAS-NMR spectra, because the  $Y_2Ti_2O_7:Al$  sample was sintered at temperatures higher than 500 K.

In Chapter 3, oxide-ion diffusion in pyrochlore  $\text{Y}_2\text{Ti}_2\text{O}_7$  was investigated using first-principles molecular dynamics (FPMD) simulation. A mapping approach for analyzing time-series data from trajectories of ions during FPMD simulations based on Voronoi–Dirichlet partition was developed. The mapping approach was applied to ion trajectories from FPMD simulations, suggesting that defect states in pyrochlore  $\text{Y}_2\text{Ti}_2\text{O}_7$  are classified into three types: a Frenkel pair, a single vacancy, and a split vacancy. In the subsequent analysis, the oxide-ion migration was found to occur by a two-step cooperative mechanism via a split vacancy during FPMD simulations. Climbing-image nudged elastic band calculation was also used to evaluate energy barriers of cooperative and stepwise diffusion mechanisms. These results showed the energy barrier for the cooperative diffusion mechanism to be substantially less than that of a simple stepwise mechanism. This lower energy barrier was comparable to experimental activation energies of oxide-ion diffusion in  $\text{Y}_2\text{Ti}_2\text{O}_7$  reported in the literature, making this previously unrecognized cooperative mechanism the most likely candidate for enabling oxide-ion transport in the titanate pyrochlore.

In Chapter 4, crystal structures and energetics of a series of  $A_2B_2O_7$  ( $A = \text{Lu}^{3+}$ – $\text{La}^{3+}$ ,  $B = \text{Zr}^{4+}$ ,  $\text{Hf}^{4+}$ ,  $\text{Sn}^{4+}$ , and  $\text{Ti}^{4+}$ ) compounds have been systematically investigated using first-principles calculations. Initially, an exhaustive configurational search based on two sub-lattice models revealed that the lowest energy structure in the  $\text{Yb}_2\text{Ti}_2\text{O}_7$  composition is a triclinic weberite-type structure characterized by alternating layers Yb and Ti. The stability of the weberite-type and pyrochlore structures at finite temperature was investigated by calculating lattice vibrational contribution to the free energies. The resulting free energies showed that the transition temperature between the weberite-type and pyrochlore structures of  $\text{Yb}_2\text{Ti}_2\text{O}_7$  is 550 K. Moreover, the energies of the weberite-type and pyrochlore structures were also compared for a wide range of  $A_2B_2O_7$  compositions. It was found that the stability of the weberite-type structure increases relative to the pyrochlore structure as the  $A^{3+}$  cation radius decreases. The stability field of the weberite-type structure found to cover the

composition range where the formation of the weberite-type structure has been experimentally observed. In  $A_2Zr_2O_7$  and  $A_2Hf_2O_7$ , the formation of such defect-fluorite structures found to be more energetically favorable at higher temperatures for smaller  $A^{3+}$  cation radii. These results were consistent with previously reported experimental results.

In Chapter 5, oxide-ion diffusion in both weberite-type and pyrochlore structures with the  $Yb_2Ti_2O_7$  composition are investigated using FPMD simulations. Mean square displacements calculations showed that oxide-ion diffusion coefficient of the weberite-type is larger than that of pyrochlore by one order of magnitude. Oxide-ion density distribution in the structures was simulated by FPMD simulations. The distribution maps showed that in the pyrochlore structure, three-dimensional oxide-ion diffusion occurs between  $48f-48f$  sites, whereas in the weberite-type structure, two-dimensional diffusion occurs on the Ti–O layers. These findings have suggested the unique applicability of the weberite-type structure to the development of oxide-ion conductors.

This thesis investigated the defects, oxide-ion diffusion, and phase stability of pyrochlore-related oxides using first-principles calculations and MAS-NMR experiments. The author believes that the findings and approaches to illuminate the essential properties of pyrochlore-related oxides, and to contribute the development of oxide-ion and mixed conductors that will be utilized in the next generation.